PHYSICS BASED PREDICTION OF AEROMECHANICAL LOADS FOR UH-60A ROTOR

A Dissertation
Presented to
The Academic Faculty

by

Ritu Priyanka Marpu

In Partial Fulfillment
of the Requirements for the Degree
Doctor of Philosophy in
Aerospace Engineering

Georgia Institute of Technology
May 2013

PHYSICS BASED PREDICTION OF AEROMECHANICAL LOADS FOR UH-60A ROTOR

Approved by:

Dr. Lakshmi N. Sankar, Advisor School of Aerospace Engineering *Georgia Institute of Technology*	Dr. Stephen M. Ruffin School of Aerospace Engineering *Georgia Institute of Technology*
Dr. Dewey Hodges School of Aerospace Engineering *Georgia Institute of Technology*	Dr. James Baeder Department of Aerospace Engineering *University of Maryland*
Dr. J.V.R. Prasad School of Aerospace Engineering *Georgia Institute of Technology*	

Date Approved: 3rd April, 2013

Dedicated to my parents,

Raja and Silviya

and my sister

Rhea

for their unconditional love and support

ACKNOWLEDGEMENTS

I thank my Lord and Savior Jesus Christ for the gift of Salvation, for this life and for enabling me to pursue the career of my choice. My awe and adoration towards God and nature are best summed up in the words of the Psalmist:

"When I consider the heavens, the work of your fingers, the sun, moon and the stars, which You have set in place, what is mankind that You are mindful of them!"- Psalm 8:3-4.

My sincere and heartfelt thanks to my advisor and mentor Dr. Sankar, for his support, vision and guidance. Dr. Sankar's encouragement and his never ending patience has encouraged and challenged me all these years as a graduate student and research assistant at Georgia Tech. He is a wonderful boss to work, ever-ready to discuss a research problem and I could not have asked for a better advisor to guide me in my doctoral research. Dr. Sankar's exemplary personality and professional life have taught me life lessons.

I would like to thank Dr. Stephen Ruffin, Dr. Dewey Hodges, Dr. James Baeder and Dr. J.V.R. Prasad for agreeing to be on my thesis committee and for providing suggestions for improvement of the thesis document. I am grateful to Mr. Alan Egolf who has always advocated for efficient and accurate methods and his vast experience with vortex methods has been instrumental in making GT-Hybrid an efficient tool applicable to rotorcraft industry. I am thankful to Dr. Nischint Rajmohan, whose work on GT-Hybrid forms the basis of my thesis work.

I would like to thank giants in the rotorcraft field, Dr. Robert Ormiston and Mr. Bill Bousman whose dynamic vision and guidance have shaped the face of rotorcraft research in recent years. I am thankful to them for encouraging and challenging several young minds to pursue the same kind of vision for next-generation technology. I look up to Dr. Anubhav Datta and Dr. Hyeonsoo Yeo for taking interest in my work and providing valuable feedback on my work.

My sincere thanks to our collaborators and industry partners, Drs. Ram Janakiram, Stephen Makinen, Mark Wasikowski, Ted Meadowcraft, Hormoz Tadghighi, Hossein Saberi and Loren Ahuas.

I would like to thank the Airloads Workshop community for collaborating on all our research activities. I would like to express my gratitude to Mike Rutkowski and the Center for Rotorcraft Innovation (VLC) for their continued support and funding of my research work. I am extremely grateful to Robert Kufeld and Thomas Norman for making the UH-60A flight test and wind tunnel test data readily available for our perusal.

The time spent at Georgia Tech was enriching both academically and personally. I would like to thank my labmates and friends JeeWoong Kim, Eliya Wing, Alpha Bah, Kyle Collins, Andrea La and Robert Lee for their friendship and discussions. My thanks to colleagues Drs. Nandita Yeshala, Hancao Li, Byung-Young Min, Afifa Zaki, Liwei Zhang.

I am greatly indebted to my parents and sister who have been the pillars of support throughout my life; and their unconditional love and affection has been a great source of strength and confidence. I dedicate this thesis work to them.

TABLE OF CONTENTS

LIST OF TABLES

LIST OF FIGURES

NOMENCLATURE

a	Speed of sound
b	Wing semi-span
c	Chord
$C_n M^2$	Normal force coefficient $(N/\left(\frac{1}{2}\rho a^2 c_{ref}\right))$
$C_m M^2$	Pitching Moment coefficient $(PM/\left(\frac{1}{2}\rho a^2 c_{ref}^2\right))$
C_p	Pressure coefficient $((p - p_\infty)/q_{ref})$
C_T	Thrust coefficient $(T/\left(\rho_\infty A V_{tip}^2\right))$
d	Distance from the wall
D	Drag force
D'	Sectional drag force
e	Flapping hinge offset.
EN	Energy per unit volume
E, F, G	Inviscid flux matrices
E_v, F_v, G_v	Viscous flux matrices
F/M	Force and moment
F_c	Chord-wise force
F_z	Force along z-direction
g	Acceleration of gravity
h_0	Specific total enthalpy
I	Identity matrix
J	Jacobian of grid transformation
k	Thermal conductivity, Reduced frequency

k_β	Hinge spring constant
l	Length
L	Lift force, Reference length, Load, Rotational matrix
L'	Sectional lift force
L, D, U	Lower, diagonal and upper block triangular matrix
L, M N	Moments about helicopter center of mass
m	Mass
M	Mach number
M_z	Yaw moment
N	Normal force
N_b	Number of blade
n_t	Grid velocity in the surface normal direction
n_x, n_y, n_z	Surface normal vector
p	Pressure
P	Per-revolution
Pr	Prandtl number
Psi	Azimuth angle
q	State vector
q_{ref}	Dynamic pressure ($\frac{1}{2}\rho_\infty V_{tip}^2$ for rotor analysis)
Q	State variable vector, Vorticity and strain rate balance, Torque
r	Radial location
Re	Reynolds number
RHS	Shorthand notation for the terms on the right hand side for any equation
s	Sectional span length

S	Vorticity
S_{ij}	Strain rate
t	Time, Thickness
T	Temperature, Thrust
u, v, w	Cartesian components of velocity
U, V, W	Contravariant velocity
$\boldsymbol{V}$	Velocity
w	Weight function
x, y, z	Cartesian coordinates
y^+	Viscous sub-layer length scale ($y\sqrt{\rho\tau_w}/\mu$)

Greek Symbols

α	Angle of attack
α_s	Shaft tilt angle
β	Flapping angle
δ	Central difference operator
Δ	Difference, Grid spacing
ε	Turbulent dissipation
ϕ	Limiter function, Phase angle
$\Delta\phi, \Delta\theta, \Delta\psi$	Euler angles
γ	Specific heat ratio
Γ	Vortex strength
κ	Turbulent kinetic energy
λ	Eigen value
μ	Viscosity, Advance ratio

μ_l	Molecular viscosity
μ_t	Turbulent viscosity
θ	Pitch angle
ρ	Density
σ	Solidity
τ_{ij}	Shear stress tensor component
ω	Turbulent specific dissipation
ξ, η, ζ	Curvilinear coordinates
ψ, Ψ	Azimuth angle
Ω	Main rotor RPM

Subscripts

0	Amplitude of zero-th harmonic
$1c, 1s$	Amplitude of first harmonic
i, j, k	Indices in three coordinate directions
LL	Lifting line
L, R	Left and right sides of the cell faces
max	Maximum
n	Normal direction
p	Pressure
t	Derivative with respect to time
$wall$	Variable on the wall surface
x, y, z	Derivatives with respect to Cartesian coordinates
ξ, η, ζ	Derivatives with respect to curvilinear coordinates
∞, inf, ref	Reference value

Superscripts

-1	Inverse matrix
l, r	Left and right sides of the cell faces
$m, m+1$	Sub-iteration level
$n, n+1$	Time level
sgs	Sub-grid scale
*	Non-dimensional variable
^	Generalized coordinate
–	Matrix in the computational domain
~	Roe-averaged quantity
+	Positive Eigen value
-	Negative Eigen value

Acronyms and Abbreviations

2-D	Two Dimensional
3-D	Three Dimensional
BC	Boundary Condition
BVI	Blade Vortex Interaction
CFD	Computational Fluid Dynamics
CSD	Computational Structural Dynamics
DES	Detached Eddy Simulation
FSI	Fluid Structure Interface
GCL	Geometric Conservation Law

HRKES	Hybrid RANS-KES
KES	Kinetic Eddy Simulation
LES	Large Eddy Simulation
LC	Loose Coupling
LU-SGS	Lower-Upper Symmetric Gauss Seidel
MUSCL	Monotone Upstream-centered Scheme for Conservation Laws
PDE	Partial Differential Equation
RANS	Reynolds Averaged Navier-Stokes
RHS	Right Hand Side
rpm	Rotation-per-minute
SA	Spalart-Allmaras
SST	Shear Stress Transform
T.E	Trailing Edge

SUMMARY

Helicopters in maneuvering flight are characterized by aperiodic airloads and structural loads as well as dependence of rotor response on vehicle dynamics. The rotor blades operate in severe operating environments and are affected by complex transonic and dynamic stall phenomena to varying degrees. Maneuvers are critical points in rotor and hub design and experience high load factors. The strength and durability of rotor and hub components is dependent on the accurate prediction of mean and peak-to-peak structural loads. The study of aeromechanical loads during extreme maneuvers using efficient and high fidelity computational tools is therefore very important for the design and development of next generation rotorcraft.

The objective of this research is to investigate and capture all the key physical phenomena for steady level flight and extreme maneuvers for the UH-60A with the goal of improving the prediction quality of rotating system aeromechanical loads. The current work employs GT-Hybrid, a Navier-Stokes/free-wake Computational Fluid Dynamics software coupled to DYMORE, a flexible multi-body structural analysis software in loosely coupled manner applicable to steady level flight and for quasi-steady maneuvers.

Selected speed and thrust sweep runs from the recently obtained (May 2010) UH-60A wind tunnel tests at the NFAC are studied to assess the prediction quality of key aerodynamic phenomena such as vortex bundling at low speeds, compressibility effects at high speed and dynamic stall cycles on highly loaded rotors. In this effort, wake modeling effects on time histories and frequency content of aeromechanical loads have been studied. It was found that a multiple trailer representation of the trailing wake

improved the correlation of loads in the inboard stations, which was significant for low-speed flight conditions with significant vortex bundling. Inclusion of the shed wake improved dynamic stall prediction in high thrust conditions. Rotor performance and trim settings were obtained and were found to be in good agreement with test data.

The aeromechanical loads developed during selected revolutions of severe diving turn maneuvers 11680 and 11679 are studied. The diving turn maneuver (11680), ranked the most severe out of all the flight conditions recorded in the UH-60A flight database, experiences a peak load factor of nearly 1.9 during the maneuver and is characterized by the most severe torsional and pitch-link loads. To analyze the rotor loads developed during this maneuver, the structural model is validated by imposing measured airloads from flight test data on the rotor structure to obtain blade deformations. These blade deformations are then imposed on the CFD grid to perform grid sensitivity studies. Next, time histories of aerodynamic sectional normal loads and pitching moments, blade structural loads, and pitch-link loads are presented. The rotor experiences extensive occurrence of stall including an advancing blade stall phenomenon for this maneuver. The fundamental mechanism behind this stall occurrence is explored. An examination of the harmonic content of structural loads indicates that the current methodology gives an accurate prediction of harmonics 1P-3P, but under-predicts harmonics 4P-6P.

CHAPTER 1

INTRODUCTION

The prediction and analysis of loads developed on a helicopter rotor remains a challenging task because of the complex environment under which the rotor blades operate. The state-of-the-art in rotor aeromechanical load prediction covers a wide range of research areas such as dynamics, aeroelastic response and stability, vibration prediction, unsteady aerodynamics, high-speed flow, wake modeling, computational fluid dynamics and flight mechanics among others. In order to develop tools that accurately predict aeromechanical loads under a variety of flight conditions it is of utmost importance to understand the underlying mechanisms.

Over the last two decades, computational tools have been extensively developed for modeling rotorcraft aeromechanics. Low fidelity lifting-line based tools have been unable to capture some of the defining characteristics of the flow field. High fidelity computational fluid dynamics (CFD) based tools model the flow physics more accurately, but they need to be coupled with computational structural dynamics (CSD) codes to perform a complete, trimmed aeroelastic analysis of the rotor. Maneuvering flight introduces additional challenges that need to be addressed by computational tools. Maneuvers are flight conditions with non-zero accelerations and angular accelerations, giving rise to unsteady rotor airloads and structural response. Additionally, the rotor response is dependent upon vehicle dynamics, pilot control input, and interactional aerodynamics. The rotor blade airfoils operate close to, and beyond, the stall region. Large blade elastic deflections intensify aeroelastic phenomena, and the operating environment is highly unsteady. The slender and flexible blades of rotor combined with severe load conditions provide challenges to the prediction of vibratory loads. The unsteady loads encountered in maneuvering flight impose severe demands on the rotor structure and dictate the overall sizing and structural properties of the helicopter rotor. Thus, the capability to accurately predict the airloads and structural loads encountered during maneuvers is critical from a rotorcraft designer's perspective.

The focus of the present research is on the modeling, analysis and fundamental understanding of the loads experienced by the UH-60A rotor in a variety of steady level flight and severe maneuvering flight conditions. The current work utilizes extensive wind tunnel and flight test datasets conducted for the UH-60A with the goal of gaining physical insights into the mechanisms that cause severe loading as well as complex aerodynamic and aeroelastic phenomena.

1.1 Motivation

Helicopters in forward flight experience complex aerodynamic phenomena to various degrees. In low speed level flight, the vortex wake remains close to the rotor tip path plane and interacts with the rotor blades to give rise to blade vortex interaction phenomena which are a major source of noise and vibration. In high-speed flight, compressibility effects dominate, leading to the formation of shocks. In high thrust flight, the retreating blade experiences a rapid variation in the effective pitch angle, giving rise to three-dimensional dynamic stall phenomena.

Maneuvers are critical aspects of rotor and hub design. The strength and durability of rotor hub components is dependent on the accurate prediction of peak-to-peak structural loads at the blade root. Accurate knowledge of control loads is important for sizing the expensive swash-plate components, for fatigue. The component size is generally dictated by large loads that occur during extreme flight conditions. Rotor components need to be redesigned if the loads occurring during extreme maneuvers are outside of the design load spectrum, or else a shorter lifespan must be accepted for those components.

Incorrect estimation of the fatigue load spectrum for rotor components can be detrimental to an aircraft design program. The rotor oscillatory loads define the fatigue loading on the rotating system components. Oscillatory loads are defined as 1P and higher in the rotating system. They are also the major source of airframe vibratory loads. The vibratory loads that are passed on from the rotating system to the fixed system cause fatigue damage for fixed-system components. Aerodynamically generated noise caused by BVI phenomena is usually dominated by harmonics above 10 or 15P and is therefore beyond the regime of vibratory loads.

The controls loads are primarily dependent on the accuracy of torsional response which is the most difficult to be captured by existing, state-of-the-art predictive tools. The peak-to-peak loads in the fixed system are dependent on the harmonic content of the rotating system loads. For example, for a 4-bladed rotor, the 4P swash-plate servo loads in the fixed system are dependent upon the 3-5P pushrod loads in the rotating system. Although accurate prediction of the peak-to-peak pushrod loads is adequate for sizing the pushrod, the harmonic content of pushrod loads must be accurately predicted to capture the 4P servo loads.

The rotor aeromechanics prediction tools must therefore be equipped to accurately predict mean, peak-to-peak and higher harmonic content of rotating system loads. This forms the motivation for the current work. The thrust of this research is therefore to investigate important physical phenomena that cause severe loads on the rotor in steady and maneuvering flight conditions. The secondary goal is to improve the prediction quality of the harmonic content of the rotating system loads by accurately predicting key aerodynamic phenomena.

1.2 Model and full scale Rotor tests

The ability to accurately predict the performance and loads of a rotor across various operating conditions is essential for the design and development of next-generation rotorcraft. Therefore, it is of primary importance to assess the prediction quality and reliability of performance prediction tools. Validation of these performance predictive tools requires high quality experimental data. A number of model and full scale rotor tests were conducted in the past with the aim of investigating complex aerodynamic phenomena for a rotor in forward flight such as regions of blade stall, compressibility effects as well as to study performance characteristics. The objective of conducting extensive tests is to make rich datasets available for the development and validation of numerical codes.

One of the earliest experimental efforts in obtaining rigorous full scale and model rotor tests include those for the following rotor configurations - H34 [1], AH-1G [2], [3] and BERP/Lynx [4]. In order to aid in the development of rotor hover performance codes, hover tests for a model helicopter rotor were conducted [5] and detailed blade pressure measurements and tip vortex trajectories were captured. Wind tunnel tests for a 1/5th scale model of the Boeing Vertol model 360 [6], [7] were conducted and rotor performance, blade and control loads and blade pressure data were recorded. More recently, three significant and extensive databases for the UH-60A rotor have been instrumental in advancing the state-of-the-art in rotor airload and structural load prediction, which are discussed next.

1.2.1 UH-60A Model DNW Wind Tunnel Test

The first and extensive airload measurements for a pressure-instrumented and aeroelastically scaled model of the UH-60A black-hawk under steady flight conditions were conducted at the DNW [8]. The DNW test included steady, level flight, descent, and hover conditions, and was conducted as a joint acoustics and aerodynamics program by the AFDD/NASA, UTRC and Sikorsky. A rich dataset consisting of blade pressure, acoustics, dynamics and performance was produced, and a range of test conditions were simulated with the aim of understanding the behavior of the UH-60A rotor. The data obtained from the DNW wind tunnel were used to study and identify regions of blade stall, study blade-vortex interaction, and validate numerical methods. At a low advance ratio $\mu = 0.1$, the unsteady airloads were found to be most strongly influenced by the wake effects and by compressibility effects at high advance ratios of $\mu = 0.3$. The compressibility effects combined with cyclic pitch, structural twist and aeroelastic effects created a region of supersonic flow and negative loads on the advancing blade.

1.2.2 UH-60A Flight Test Program

The NASA-Army UH-60A Airloads Program [9] has provided the highly researched and most extensive rotor flight test database, which includes pilot input, vehicle attitudes, blade airloads and structural loads. A number of steady and maneuvering flight counters were flown and studied as a part of this program. A number of maneuvering flight conditions were carried out including level bank-turns, diving bank-angle turns, symmetric pull-ups, rolling pullouts and pushovers, UTTAS maneuvers among the others [9], [10]. A ranking system based on a subset of six measurements was developed to rank the maneuvers based on severity of the loads developed. The six measurements are: the pitch-link load, torsional moment at 0.3R, and the flap and chord bending moment measurements at 0.113R and 0.6R. During the diving turn 11680, the helicopter developed the most severe push-rod loads, torsion moment at 0.3R and chord bending moment at 0.113R. The second most severe maneuver is the longitudinal pull-up (11029) which had the highest flapwise-bending moment at 0.113R.

The two most severe maneuvers encountered by the UH-60A rotor are - Diving Turn maneuver (11680) followed by the UTTAS Pull-up (11029). The diving bank angle turns address flight counters obtained in diving turns where the kinetic energy available in the descent flight provides the necessary power for high load factor and high speed turns.

Significant research has been done in the past decade to model and understand the fundamental phenomena underlying the critical steady flight conditions ([11], [12], [13], [14], [15]) and the UTTAS longitudinal pull-up maneuver [16]. Rajmohan [17] used the Hybrid CFD methodology to study and validate steady level flight conditions [18] and the transient pull-up maneuver 11029 [19], [20]. Marpu *et al.* used the Hybrid CFD methodology coupled to multibody dynamics approach to study the diving turn maneuvers 11680 and 11679 [21], [22].

1.2.3 UH-60A Wind Tunnel Test at NFAC

While steady and maneuvering flight test data provide a valuable resource for validating rotorcraft aeromechanical predictive tools, they are coupled with vehicle dynamics and pilot control inputs and contain uncertainties associated with recording flight test data. In order to address these limitations with flight test data, a controlled set of high quality wind tunnel data for the UH-60A configuration was recently conducted [23].

NASA and the US Army have completed (May 2010) a wind tunnel test on a full-scale pressure-instrumented UH-60A rotor system at the USAF's National Full-Scale Aerodynamics Complex 40- by 80-Foot Wind Tunnel. The primary objective of this NASA/Army test program was to provide an extensive database for the validation of predictive tools [23], [24], [25]. A secondary objective was to meet one of the original goals of the UH-60A Airloads program, that is to provide data to evaluate the similarities and differences between small-scale wind tunnel, full-scale wind tunnel, and full-scale flight tests. A variety of flight conditions was studied, including speed sweeps at constant thrust (for advance ratios up to 0.4) and thrust sweeps at a constant advance ratio. The data acquired from this test included blade airloads and structural loads, steady and oscillatory hub forces and moments, and blade displacements and deformations. Romander *et al.* [24] investigated specific parametric speed and thrust sweeps by employing loosely coupled OVERFLOW and CAMRAD II and obtained detailed airloads and performance data. Yeo *et al.* [26], investigated the quality of aeromechanical load prediction for the speed and thrust sweeps using two approaches comprehensive analysis only (CAMRAD II) and CFD/CSD (CAMRAD II/OVERFLOW 2) and reported significant improvement in predictions using the coupled CFD/CSD analysis. Marpu *et al.* [27] studied the specific parametric speed and thrust sweeps using GT-Hybrid coupled to DYMORE2 and predicted trim settings and performance indicators which showed reasonable agreement with the test data for the conditions studied. Chang *et al.* [28]

found that while empirical corrections (Glauert correction term) to shaft angle of attack are appropriate at low speed, high speed, and low thrust conditions, CFD modeling of wind tunnel walls is important at high thrust conditions. Datta *et al.* [25] studied the behavior of the UH-60A rotor under reduced rotor RPM and high advance ratios.

1.3 Literature survey

1.3.1 Rotorcraft Comprehensive Analysis Methods

Comprehensive analyses codes are typically used for calculating performance, loads, response and stability of helicopter rotors. These have been traditionally used by the helicopter industry. Rotor comprehensive analysis codes solve for the dynamics of flexible blades in flap, lag and torsion, and solve for trim to identify the control positions. Comprehensive analysis codes are equipped with lifting line based aerodynamic model for representing the wake vortex and typically employ empirical models for accounting for rotor inflow models and stall. A semi-empirical unsteady aerodynamic model developed by Leishman and Beddoes [29] is usually included for modeling unsteady aerodynamics, separated flow and dynamic stall. The early comprehensive analyses codes include first generation CAMRAD (Comprehensive Analytical Model of Rotorcraft Aerodynamics and Dynamics) [30] 2GCHAS (Second Generation Comprehensive Helicopter Analysis System) [31], [32] Bell's COPTER and Sikorsky's Rotorcraft System Dynamic Analysis (RDYNE) [33] and UMARC [34]. An extensive literature survey and the development of rotorcraft comprehensive analyses has been documented by Johnson [35].

Beginning in the 1990's, significant progress has been made in comprehensive analysis tools due to the implementation of non-linear finite element method and multibody dynamics techniques for modeling the complex configurations. Comprehensive Analysis such as CAMRAD II [36], RCAS [37], DYMORE [38] and UMARC2 [39] are capable of modeling a rotorcraft using a combination of multibody dynamics, structural dynamics and approximation for rotor wake and blade aerodynamics. CAMRAD II developed by Johnson Aeronautics uses geometrically exact non-linear finite elements and assumes moderate deflections. The Rotorcraft Comprehensive Analysis System (RCAS) [37] was extensively modified from 2GCHAS [32].

The current research effort utilizes DYMORE developed by Bauchau *et al.* [40], [38], [41] at the Georgia Institute of Technology, which uses a geometrically exact finite-elements, without making assumptions about the size of deflections. DYMORE uses a multibody dynamics approach to model components of the rotor, and consists lifting line aerodynamics and auto-pilot trimmer and empirical models for accounting for unsteady aerodynamic phenomena. The cross-sectional properties of the rotor blade which is modeled as a beam is obtained using the Variational Asymptotic Beam Sectional Analysis (VABS) developed by Hodges *et al.* [42], [43], [44] which is an efficient high-fidelity cross-sectional analysis, capable of realistic modeling of initially curved and twisted anisotropic beams with arbitrary sectional topology and materials.

Although all the comprehensive analysis tools use sophisticated finite element models for structural analysis, the aerodynamic methods are of lower fidelity and require CFD for capturing unsteady and compressibility effects.

1.3.2 Rotorcraft CFD methods

In understanding the flow field of a rotor blade, numerous first-principles based methodologies have been proposed in the last two decades. In this section, the past and the existing methodologies for calculating the flow field over a rotor and the developments leading to the use of Navier-Stokes solvers for rotorcraft will be reviewed.

The earliest methods in modeling flow over rotors used extension of Prandtl's lifting line and modeled the individual blades as lifting line vortices. Gray [45] modeled the wake of a hovering model rotor as a helical vortex. Landgrebe [46] used the helical wake geometry to predict the performance of a hovering rotor. The free wake analysis methods were developed by Scully [47] and Summa [48]. In the free wake analysis the tip vortex is modeled as a series of line vortex filaments and tracked in a Lagrangian manner. The velocity field using the free wake methodology is computed using the Biot-Savart law and numerical integration.

The use of transonic small disturbance theory marks the beginning of first principles based study of forward flight for rotors. Several researchers used potential flow methodologies to study the flow field of a rotor in forward flight. Caradonna and Isom [49] developed the transonic small disturbance theory to model flow over rotors. In this work, the effect of the wake vortex and trim were included through a table of angle of attack changes, obtained from a comprehensive analysis. Subsequently, the unsteady potential flow solvers were modified to handle embedded vertical flows. Chang [50] developed the steady form of a full potential flow solver for isolated wings to model rotors and later extended the method to solve unsteady potential flows [51]. Egolf and Sparks [52] used the full potential formulation and embedded vortex element to account for the wake influence. The full potential solvers included viscous effects through a boundary layer correction and could only model mild shocks. Sankar and Prichard [53]developed an unsteady full potential flow based solver for rotors called RFS2 and coupled it to CAMRAD in an open-loop manner. Sankar and Malone [54] modified RFS2 by implementing a velocity transpiration method which could take into effect the unsteady interactions of an airfoil with passing vortices. However, the potential flow method has only a little capability in capturing the compressibility effects and flow separation.

During the late 1980's, Euler methods for forward flight began to be developed and used. Sankar *et al.*[55], Agarwal *et al.* [56] and Hassan *et al.* [57] developed Euler solvers for isolated rotors. Sankar and Tung [58] coupled the Euler solver to CAMRAD in an open-loop manner. Strawn and Barth [59], Srinivasan and McCroskey [60], solved the hovering rotor by capturing the wake in Eulerian manner.

The first instance of Navier-Stokes solver for a rotor was due to Wake and Sankar [61], [62], who used a hybrid ADI implicit time marching algorithm to study rotor flow fields in hover and forward flight. The effects of the rotor wake were incorporated using an inflow table. Srinivasan and Baeder [63], [64] developed Navier-Stokes methods for isolated rotors. The NS solvers can model the advancing blade transonic effects as well as retreating blade dynamic stall phenomena. However, the early NS solvers depended on external wake models for calculation of inflow velocities. Chen, McCroskey, Obayashi [65] used an implicit L-U factorization scheme and an external free wake model to solve forward flight rotor flows. Bangalore [66] used first principles based methods to investigate high lift rotor systems. In most of these analyses, the tip vortex was captured through one revolution, beyond which the vortex diffused due to numerical dissipation. Steinhoff *et al.* [67] and Wang *et al.* [68] proposed vorticity confinement techniques to prevent tip vortex diffusion, which used artificial convective velocities to convect vorticity towards the centroid of the vortices.

The current state-of-the-art in high fidelity rotorcraft CFD simulations is to use a Chimera grid or an overset framework for modeling rotors in forward flight. OVERFLOW [69] is a popular RANS based flow solver developed at NASA, that has been applied to a wide range of fluid dynamic problems. OVERFLOW-D [70] has been applied in the past to solve time-dependent problems. The overset methodology utilizes near-body grid and off-body grids. The near-body grids are body fitted grids that are used for modeling solid boundaries while the off-body grids are used for wake capturing. The wake capturing methods are computationally expensive and typically require a formidable number of grid points and hundreds of computational cores to capture the wake without diffusion. On the other hand, hybrid methodologies where the wake structure is modeled in a Lagrangian manner are computationally efficient and thus offer an attractive alternative. The current work utilizes a computationally efficient hybrid Navier-Stokes/free-wake Methodology, the details of which are discussed in Chapter 2.

It is imperative for the next generation rotorcraft CFD solvers to be built using high performance computing paradigms. One such effort is the Helicopter Overset Simulations dubbed Helios [71] which is currently under development by the high performance computing institute HI-ARMS and CREATE-AV (Air Vehicles) programs sponsored by the DoD HPC Modernization Program Office. Helios provides several features that are different from the existing state-of-the-art in rotorcraft CFD. Some of the features include: utilization of heterogeneous meshing paradigms, parallel overset grid assembling capability with implicit hole cutting, solution adaptation and high-order accuracy in the off-body solver.

1.3.3 Rotorcraft Coupled CFD/CSD Analyses

Coupling between CFD and rotorcraft comprehensive codes is typically accomplished in two ways. In the loose coupling methodology, the information between CFD and CSD is transferred in a periodic manner, after each revolution. In the tight (strong) coupling methodology, the CFD and CSD codes exchange blade deformations and airloads at every time step. The tight coupling method as applied to rotorcraft uses a serially staggered approach wherein the flow solution lags the structural dynamic solution by one time step. Although the tight coupling methodology is a more rigorous approach, it is computationally intensive and rotor trim is a formidable task. Altimus [72] compared the two coupling approaches and showed that the tight coupling requires 2.5 times increase in computational cost while generating the same airload predictions at high speed using a loose coupling approach. Bauchau *et al.* [73] and Pomin *et al.* [74] studied tight coupling with fixed control angles to avoid trimming the rotor.

Seminal work done in the last decade for studying the physical phenomena in high speed and high thrust conditions and other steady flight counters of the UH-60A Airloads Program [9], paved way to the study of maneuvering flight over the last few years. Sitaraman [75] used TURNS [64], a CFD solver computations with CSD (UMARC) in an open-loop coupled approach to investigate unsteady rotor airloads for the UH-60A in steady level flight and reported excellent agreement with test data. Phanse [76] tested and validated tight coupling between a Hybrid CFD/wake coupling code (GT-Hybrid) and DYMORE and loose coupling between GT-Hybrid and CAMRAD2. Datta *et al.* [13]

used CFD (TURNS) computations with CSD (UMARC) in an open-loop coupled approach to gain a fundamental understanding of rotor vibratory loads in different steady flight conditions. Datta [12] also studied the dynamic stall loads in high altitude flight for the UH-60A rotor. Potsdam *et al.* [14], [77] conducted a loosely coupled CFD (OVERFLOW-D) - CSD (CAMRAD 2) study and obtained predictions for UH-60A airloads for a range of different flight conditions and found good agreement with test data.

In the area of unstructured grid methodologies in CFD, Biedron and Lee-Rausch [78] [79] used unsteady RANS based flow solver FUN3D in conjunction with CAMRAD II in a loosely coupled framework for obtaining trimmed aeroelastic computations. Abras *et al.* [80], enhanced the modeling of rotor system using the unstructured CFD/CSD (FUN3D/CAMRAD II) framework by conserving virtual work between CFD and CSD methods and applied this methodology to study a moderate speed flight condition (8424) and a high speed flight condition (8534).

The coupling methods for steady level flight conditions use efficient trim algorithms to estimate the pilot controls required to achieve the trim state. The analysis of maneuvering flight requires knowledge of the instantaneous control pitch settings, the vehicle velocity components, attitudes, and the pitch, roll, and yaw rates and accelerations as a function of time. Thus, the study of maneuvers presents a challenging scenario for the validation of CFD/CSD methodologies. Rajmohan [17] developed "Aeromechanics/Flight Mechanics Coupling Methodology" that eliminates the need to know pilot inputs a priori, which was previously a challenge to simulate new maneuvers. Bhagwat *et al.* [16], [81] were the first to perform tightly coupled simulations of maneuvering flight by coupling OVERFLOW-2 with a rotorcraft comprehensive code, RCAS to study the airloads and structural loads of UTTAS pull-up maneuver of the UH-60A Airloads Program. Silbaugh [82] studied staggered and time accurate tight coupling between TURNS and UMARC for the UTTAS pull-up (counter 11029) maneuver. Rajmohan [17] applied loose and tight coupling methodologies using GT-Hybrid (CFD) and DYMORE (CSD) to study steady and maneuvering flight.

1.3.4 Modeling and Study of Maneuvers

Maneuvers are defined as transient when one or more acceleration or angular acceleration components are non-zero. However, the distinction between steady and unsteady maneuvers is sometimes difficult to make. From a rotor loading perspective, even for short-duration transient maneuvers, there may be multiple consecutive rotor revolutions which for prediction purposes may be considered quasi-steady. The control loads in a maneuver may be three to four times higher than those at the maximum level speed [10].

The study of helicopters in maneuvering flight is a multidisciplinary topic addressing areas such as flight mechanics, optimal control theory, rotor dynamics, interactional aerodynamics and aeroelasticity.

In the area of flight dynamics, Horn *et al.* [83] developed methods to predict maneuvering flight envelope of aircraft within structural load limits. Bottasso *et al.* [84] formulated maneuvers as optimal control problems and developed parameter optimization approach for studying trajectories for maneuvering vehicles. Moon *et al*.[85] used an optimal control approach to study vehicles in aggressive maneuvers for avoiding obstacles and for envelope protection.

In the field of interactional aerodynamics, Ruffin and Lee [86] studied rotor-airframe interaction using efficient viscous approach using a Cartesian grid framework. Renaud *et al.* [87] studied rotor fuselage interaction using a fully unstructured CFD solver FUN3D and obtained good correlations. Duque *et al.* [88] coupled high fidelity LES based CFD, CSA and CAA tools to model noise characteristics for helicopters in maneuvers.

In the field of aeroelasticity, the work of Edward Beno [89] marks one of the earliest efforts in systematically studying maneuver loads for the NH-3A and CH-53A rotors. In this seminal work, the available airload and blade response data were analyzed to gain a better understanding of the sources of rotor vibratory loads in level and maneuvering flight conditions. The emphasis was placed on understanding the mechanisms leading to high-frequency rotor control loads. Beno systematically studied the various factors which affect the blade torsional response: the advance ratio, blade loading, blade/tip-vortex wake interactions, maneuvers, advancing blade critical Mach number, blade bending and aerodynamic pitching moment. It was found that the blade/vortex crossings had little effect on the retreating blade torsional oscillations. There was no correlation observed between the retreating side blade torsional oscillations and the coupling of flapwise and chordwise response. Further analysis of the data identified the aerodynamic pitching moment as primarily contributing to the measured torsional oscillations.

1.4 Research Objectives and Scope

The aim of the current work is to study the aeromechanical loads developed on the UH-60A rotor during steady and maneuvering flight conditions to contribute to the current state-of-the-art in rotor load prediction. A secondary objective is to use a variety of flight test and wind tunnel test data to investigate the physics behind critical aerodynamic and structural phenomena occurring in steady and maneuvering flight conditions. In this work, the influence of several key aerodynamic parameters such as vortex wake bundling, compressibility effects and dynamic stall events on the peak-load prediction will be systematically studied.

The vibratory control loads experienced by the helicopter in high-speed and maneuvering flight conditions, place a limit on the helicopter flight envelope. In order to expand the flight envelope, it is important to understand and identify the various physical mechanisms at play that cause severe loading on the rotor and vibratory loads on the hub.

The goal of the current study is to develop computationally efficient and robust rotor aeromechanics prediction tools that can accurately predict mean, peak-to-peak and harmonic content of rotating system loads. Of particular interest in this work is the prediction of vibratory loads and higher harmonic content of structural loads which are critical in order to accurately identify the complex yet fundamental interaction phenomena occurring in a maneuvering flight. Thus, the objectives may be summarized as follows:

1. Validate the hybrid methodology for thrust sweep and speed sweep conditions by utilizing the high quality wind tunnel test database.
2. Investigate key mechanisms that cause unsteady loads in level flight.
3. Accurately predict loads, performance, blade motions and trim settings of a rotor across the flight envelope

4. To systematically investigate and capture key physical phenomena for two severe diving turn maneuvers for the Black Hawk rotor namely 11680 and 11679 in order to capture
    a. transonic events
    b. extensive dynamic stall phenomena
    c. peak-to-peak and harmonic content of structural loads
5. Decouple the aerodynamic and structural loads prediction problem firstly by imposing measured aerodynamic loads on the structural model to validate the model and thereafter impose the blade deformations on the aerodynamic model to validate it.
6. Capture the advancing side stall phenomena occurring in a region of super-critical flow, unique to severe maneuvers.

1.5 Organization of Dissertation

This dissertation is arranged as follows. The background and the motivation of this dissertation are introduced in Chapter 1. Following the introduction, a brief literature survey of the existing state of the art in rotor aeromechanical load prediction and the objectives of the current work are proposed. Chapter 2 deals with the numerical methodology used in the current work. Chapter 3 discusses appropriate numerical validations suited for various flight conditions. In Chapter 4, the wind tunnel test data are studied using a coupled CFD/CSD analysis. The results for most severe diving turn maneuvers for the UH-60A are discussed in Chapter 5. Chapter 6 consists of conclusions, suggestions for future work and recommendations.

CHAPTER 2

COMPUTATIONAL METHODOLOGY

In this chapter, a brief overview of the governing equations and the numerical formulation used in the Hybrid CFD methodology is given. The hybrid methodology in its current formulation has been developed by Yang [90] and significant enhancements were made by Rajmohan [17].

The CSD methodology is briefly discussed. The loosely coupled delta-trimming approach as applied to steady flight conditions is discussed next, followed by the necessary changes implemented for studying quasi-steady maneuvers.

2.1 Mathematical formulation of the CFD methodology

GT-Hybrid is a three-dimensional unsteady viscous compressible flow solver. The flow is modeled by first principles using the Navier-Stokes methodology. GT-Hybrid solves the three-dimensional unsteady Navier-Stokes equations in the transformed body-fitted coordinate system using a time-accurate, finite volume scheme.

The Navier-Stokes equations in transformed generalized curvilinear coordinate system are given as

$$\frac{\partial \hat{q}}{\partial \tau} + \frac{\partial\left(\hat{E} - \hat{R}\right)}{\partial \xi} + \frac{\partial\left(\hat{F} - \hat{S}\right)}{\partial \eta} + \frac{\partial\left(\hat{G} - \hat{T}\right)}{\partial \zeta} = 0, \tag{2.1}$$

where ξ denotes the chord-wise direction, η denotes the spanwise direction and ζ the normal direction. is the flow vector, represented as,

$$\hat{q} = J^{-1}\begin{Bmatrix} \rho \\ \rho u \\ \rho v \\ \rho w \\ e \end{Bmatrix} \tag{2.2}$$

The inviscid flux vector is defined as follows,

$$\hat{E} = J^{-1}\begin{Bmatrix} \rho U \\ \rho u U + \xi_x p \\ \rho v U + \xi_y p \\ \rho w U + \xi_z p \\ (e+p)U - \xi_t p \end{Bmatrix} \tag{2.3}$$

where J is Jacobian and u,v,w are the Cartesian components of velocity in an inertial coordinate system. e is the total energy per unit volume and pressure p is given by the equation of state as follows:

$$p = (\gamma - 1)\left\{e - \rho\left(\frac{u^2 + v^2 + w^2}{2}\right)\right\} \tag{2.4}$$

The contravariant velcocities U, V, W in the flux vectors are related to the grid metrics.

$$U = \xi_t + \xi_x(u - x_\tau) + \xi_y(v - y_\tau) + \xi_z(w - z_\tau) \tag{2.5}$$

$$V = \eta_t + \eta_x(u - x_\tau) + \eta_y(v - y_\tau) + \eta_z(w - z_\tau) \tag{2.6}$$

$$W = \zeta_t + \zeta_x(u - x_\tau) + \zeta_y(v - y_\tau) + \zeta_z(w - z_\tau) \tag{2.7}$$

where x_τ, y_τ, z_τ represent the motion of the grid relative to the inertial coordinate system (x,y,z). The viscous flux vector is given by,

$$\hat{R} = \boldsymbol{J}^{-1}\begin{Bmatrix} 0 \\ \xi_x\tau_{xx} + \xi_y\tau_{xy} + \xi_z\tau_{xz} \\ \xi_x\tau_{yx} + \xi_y\tau_{yy} + \xi_z\tau_{yz} \\ \xi_x\tau_{zx} + \xi_y\tau_{zy} + \xi_z\tau_{zz} \\ \xi_x\beta_x + \xi_y\beta_y + \xi_z\beta_z \end{Bmatrix} \tag{2.8}$$

$$\hat{S} = \boldsymbol{J}^{-1}\begin{Bmatrix} 0 \\ \eta_x\tau_{xx} + \eta_y\tau_{xy} + \eta_z\tau_{xz} \\ \eta_x\tau_{yx} + \eta_y\tau_{yy} + \eta_z\tau_{yz} \\ \eta_x\tau_{zx} + \eta_y\tau_{zy} + \eta_z\tau_{zz} \\ \eta_x\beta_x + \eta_y\beta_y + \eta_z\beta_z \end{Bmatrix} \tag{2.9}$$

$$\hat{T} = \boldsymbol{J}^{-1}\begin{Bmatrix} 0 \\ \zeta_x\tau_{xx} + \zeta_y\tau_{xy} + \zeta_z\tau_{xz} \\ \zeta_x\tau_{yx} + \zeta_y\tau_{yy} + \zeta_z\tau_{yz} \\ \zeta_x\tau_{zx} + \zeta_y\tau_{zy} + \zeta_z\tau_{zz} \\ \zeta_x\beta_x + \zeta_y\beta_y + \zeta_z\beta_z \end{Bmatrix} \tag{2.10}$$

By assuming Stoke's hypothesis (λ = -2/3μ), the shear terms are written as

$$\tau_{xx} = -\frac{2}{3}\mu\left(u_x + v_y + w_z\right) + 2\mu u_x \tag{2.11}$$

$$\tau_{yy} = -\frac{2}{3}\mu\left(u_x + v_y + w_z\right) + 2\mu v_y \tag{2.12}$$

$$\tau_{zz} = -\frac{2}{3}\mu\left(u_x + v_y + w_z\right) + 2\mu w_z \tag{2.13}$$

$$\tau_{xy} = \tau_{yx} = \mu\left(u_y + v_x\right) \tag{2.14}$$

$$\tau_{yz} = \tau_{zy} = \mu\left(v_z + w_y\right) \tag{2.15}$$

$$\tau_{zx} = \tau_{xz} = \mu\left(w_x + u_z\right) \tag{2.16}$$

$$\beta_x = u\tau_{xx} + v\tau_{xy} + w\tau_{xz} + k\left(\xi_x\frac{\partial T}{\partial \xi} + \eta_x\frac{\partial T}{\partial \eta} + \zeta_x\frac{\partial T}{\partial \zeta}\right) \tag{2.17}$$

$$\beta_y = u\tau_{xy} + v\tau_{yy} + w\tau_{yz} + k\left(\xi_y\frac{\partial T}{\partial \xi} + \eta_y\frac{\partial T}{\partial \eta} + \zeta_y\frac{\partial T}{\partial \zeta}\right) \tag{2.18}$$

$$\beta_z = u\tau_{xz} + v\tau_{yz} + w\tau_{zz} + k\left(\xi_z\frac{\partial T}{\partial \xi} + \eta_z\frac{\partial T}{\partial \eta} + \zeta_z\frac{\partial T}{\partial \zeta}\right) \tag{2.19}$$

where k is the coefficient of thermal conductivity, and μ is the dynamic viscosity.

2.2 Spatial Discretization

Equation (2.1) is discretized using a semi-discrete finite difference approximation in three dimensions as

$$\left(\frac{\partial \hat{q}}{\partial \tau}\right)_{i,j,k} + \frac{\hat{E}_{i+\frac{1}{2},j,k} - \hat{E}_{i-\frac{1}{2},j,k}}{\Delta \xi} + \frac{\hat{F}_{i,j+\frac{1}{2},k} - \hat{F}_{i,j-\frac{1}{2},k}}{\Delta \eta} + \frac{\hat{G}_{i,j,k+\frac{1}{2}} - \hat{G}_{i,j,k-\frac{1}{2}}}{\Delta \zeta}$$

$$= \frac{\hat{R}_{i+\frac{1}{2},j,k} - \hat{R}_{i-\frac{1}{2},j,k}}{\Delta \xi} + \frac{\hat{S}_{i+\frac{1}{2},j,k} - \hat{S}_{i-\frac{1}{2},j,k}}{\Delta \xi} + \frac{\hat{T}_{i+\frac{1}{2},j,k} - \hat{T}_{i,j,k-\frac{1}{2}}}{\Delta \zeta} \tag{2.20}$$

where

$$\begin{aligned} \Delta\xi &= \xi_{i+\frac{1}{2},j,k} - \xi_{i-\frac{1}{2},j,k} = 1 \\ \Delta\eta &= \eta_{i,j+\frac{1}{2},k} - \eta_{i,j-\frac{1}{2},k} = 1 \\ \Delta\zeta &= \zeta_{i,j,k+\frac{1}{2}} - \zeta_{i,j,k-\frac{1}{2}} = 1 \end{aligned} \tag{2.21}$$

2.2.1 Computation of Inviscid Fluxes

The inviscid fluxes *E*,*F*,*G* in the Eq. (2.20), represent the fluxes in mass, momentum and energy respectively. Solutions to NS equations encompass acoustic, vortical and entropy waves. A variety of flux-vector splitting and flux-difference splitting schemes split the flux terms based on contributions from the individual waves [91], [92]. In the current work, Roe's approximate solver is used in the inviscid flux vector splitting [93]. $\hat{E}$ is computed as

$$\hat{E}_{i+\frac{1}{2},j,k} = \frac{1}{2}\left\{\left(\hat{E}_L + \hat{E}_R\right) - \left|\hat{A}\right|(q_R - q_L)\right\} \tag{2.22}$$

where, $q_R$is set equal to the value of q just to the right of the $\left(\mathrm{i} \pm \frac{1}{2}, j, k\right)$ node and q_L is set to the value of q just to the left of $\left(i \pm \frac{1}{2}\ or\ j \pm \frac{1}{2}\ or\ k \pm \frac{1}{2}\right)$ node. The fluxes $\hat{E}_L$ and $\hat{E}_R$are evaluated at half node $\left(i \pm \frac{1}{2}, j, k\right)$ using the flow properties from the left and the right of the cell face, which are given as

$$\hat{E}_L = \begin{Bmatrix} \rho_L U_L \\ \rho_L u_L U_L + \eta_x p_L \\ \rho_L v_L U_L + \eta_y p_L \\ \rho_L w_L U_L + \eta_z p_L \\ \rho_L U_L h_{0L} - \eta_t p_L \end{Bmatrix}, \hat{E}_R = \begin{Bmatrix} \rho_R U_R \\ \rho_R u_R U_R + \eta_x p_R \\ \rho_R v_R U_R + \eta_y p_R \\ \rho_R w_R U_R + \eta_z p_R \\ \rho_R U_R h_{0R} - \eta_t p_R \end{Bmatrix}. \tag{2.23}$$

The quantities U, h_0 and η_t are contravariant velocity, specific total enthalpy and the grid velocity of the coordinate surface $(i+\frac{1}{2}, j, k)$ in the normal direction of the surface, respectively. The term $|\hat{A}|(q_R - q_L)$ in Eq. (2.22) represents the numerical viscosity term as computed by the approach presented by Vinokur and Liu [94], where

$$\left|\hat{A}\right|(q_R - q_L) = \left|\tilde{\lambda}_1\right| \begin{Bmatrix} \Delta\rho \\ \Delta\rho u \\ \Delta\rho v \\ \Delta\rho w \\ \Delta e \end{Bmatrix} + \delta_1 \begin{Bmatrix} \tilde{\rho} \\ \tilde{\rho}\tilde{u} \\ \tilde{\rho}\tilde{v} \\ \tilde{\rho}\tilde{w} \\ \tilde{\rho}\tilde{h}_0 \end{Bmatrix} + \delta_2 \begin{Bmatrix} 0 \\ \eta_x \\ \eta_y \\ \eta_z \\ \tilde{U}_c \end{Bmatrix} \tag{2.24}$$

$$\begin{aligned} \delta_1 &= C_1 \tilde{\rho} \Delta U_c + \frac{1}{2} C_2 \frac{\Delta p}{\tilde{a}} \\ C_1 &= -\left|\tilde{\lambda}_1\right| + 0.5\left(\left|\tilde{\lambda}_2\right| + \left|\tilde{\lambda}_3\right|\right) \\ C_2 &= -\left|\tilde{\lambda}_2\right| - \left|\tilde{\lambda}_3\right| \end{aligned} \tag{2.25}$$

The operator Δ is defined as a jump across the cell face. The characteristic wave speeds are given by:

$$\begin{aligned} \tilde{\lambda}_1 &= \tilde{U} \\ \tilde{\lambda}_2 &= \tilde{U} + a \\ \tilde{\lambda}_3 &= \tilde{U} - a \end{aligned} \tag{2.26}$$

All the “Roe-averaged” quantities are denoted by tilde sign, and are given by

$$R = \sqrt{\frac{\rho_R}{\rho_L}}$$

$$\tilde{\rho} = \sqrt{\rho_R \rho_L}$$

$$\tilde{u} = u_L \left(\frac{1}{1+R}\right) + u_R \left(\frac{R}{1+R}\right)$$

$$\tilde{v} = v_L \left(\frac{1}{1+R}\right) + v_R \left(\frac{R}{1+R}\right)$$

$$\tilde{w} = w_L \left(\frac{1}{1+R}\right) + w_R \left(\frac{R}{1+R}\right) \tag{2.27}$$

$$\tilde{e} = e_L \left(\frac{1}{1+R}\right) + e_R \left(\frac{R}{1+R}\right)$$

$$\tilde{u} = u_L \left(\frac{1}{1+R}\right) + u_R \left(\frac{R}{1+R}\right)$$

$$\tilde{a} = \sqrt{\gamma(\gamma-1)\left[\frac{e}{\rho} - \frac{1}{2}(\tilde{u}^2 + \tilde{v}^2 + \tilde{w}^2)\right]}$$

In the current implementation, the Monotone Upstream Centered Scheme for Conservation Laws (MUSCL) [95] is used. The MUSCL scheme is given as:

$$\begin{gathered} q_L = \left\{1 + \frac{[(1-k)\nabla + (1+k)\Delta]}{4}\right\} q_i \\ q_R = \left\{1 - \frac{[(1+k)\nabla + (1-k)\Delta]}{4}\right\} q_{i+1} \end{gathered} \tag{2.28}$$

where Δ and ∇ are the forward and backward difference operators, respectively.

The choice of parameter k determines the spatial accuracy of the scheme. The value of k = -1 yields a second-order fully upwind scheme, while k = 1 yields a second-order central difference scheme. In the present work, $k = \frac{1}{3}$ yields a third-order accurate upwind scheme.

In regions of large gradients and discontinuities, a high-order scheme must be reduced to a lower order to maintain stability and to restrict numerical oscillations in the solution. This may be accomplished by employing a flux limiter. A limiter is defined as a nonlinear algorithm that reduces the high-derivative content of a subgrid interpolant in order to make it non-oscillatory [96]. In the present methodology, the alternative form of Van Albada flux limiter [97] typically used in high order spatial schemes is used. It is defined as follows:

$$\varphi = \frac{2r}{r^2 + 1} \tag{2.29}$$

where r represents the ratio of the successive gradients on the flow solution, i.e.,

$$r_i = \frac{\nabla q_i}{\Delta q_i} = \frac{q_i - q_{i-1}}{q_{i+1} - q_i}. \tag{2.30}$$

Thus, the flux limiter is implemented as

$$\begin{aligned} \varphi^l &= \frac{2(\nabla q_i)(\Delta q_i) + \varepsilon}{(\nabla q_i)^2 + (\Delta q_i)^2 + \varepsilon} \\ \varphi^r &= \frac{2(\nabla q_{i+1})(\Delta q_{i+1}) + \varepsilon}{(\nabla q_{i+1})^2 + (\Delta q_{i+1})^2 + \varepsilon} \end{aligned} \tag{2.31}$$

where ε is a parameter that ensures there is no indeterminancy in regions of zero gradients.

2.2.2 Computation of Viscous Fluxes

The viscous fluxes R, S, T in Eq. (2.20) are computed using a symmetric second order central difference scheme. The viscous fluxes contain derivatives of the velocity components, such as u_ξ which is computed as,

$$u_\xi\Big|_{i+\frac{1}{2},j,k} = \frac{u_{i+1,j,k} - u_{i,j,k}}{\Delta\xi}, \qquad u_\xi\Big|_{i-\frac{1}{2},j,k} = \frac{u_{i,j,k} - u_{i-1,j,k}}{\Delta\xi} \tag{2.32}$$

2.2.3 Temporal Discretization

The Navier-Stokes equations are expressed in the semi-discrete form as follows:

$$\begin{gathered} \hat{q}^{n+1} = \hat{q}^n - \Delta\tau\left(\delta_\xi\hat{E} + \delta_\eta\hat{F} + \delta_\zeta\hat{G}\right)\Big|^{n+1} + \\ \Delta\tau\frac{M}{Re}\left(\delta_\xi\hat{R} + \delta_\xi\hat{S} + \delta_\xi\hat{T}\right)\Big|^{n} \end{gathered} \tag{2.33}$$

where the superscripts refer to the time levels ‘n’ and ‘$n+1$’. The semi-implicit time marching scheme with first-order backward differencing is used to advance the governing parabolic equations. The operators δ_ξ. δ_η, δ_ζ are the standard central difference operators. The inviscid and viscous fluxes are computed at the half-points.

Note that the vector $\hat{q}$ contains the Jacobian term which is not a constant for deforming grids. The above discretization yields a nonlinear system of algebraic equations for the unknown flow properties. The non-linear fluxes are linearized by performing a Taylor series expansion, so that

$$\begin{aligned} \hat{E}^{n+1} &= \hat{E}^n + [A^n](\hat{q}^{n+1} - \hat{q}^n) \\ \hat{G}^{n+1} &= \hat{G}^n + [B^n](\hat{q}^{n+1} - \hat{q}^n) \\ \hat{H}^{n+1} &= \hat{H}^n + [C^n](\hat{q}^{n+1} - \hat{q}^n) \end{aligned} \tag{2.34}$$

where the quantities $[A^n]$, $[B^n]$ and $[C^n]$ are 5×5 flux Jacobian matrices, defined as:

$$A = \frac{\partial \hat{E}}{\partial \hat{q}}; \quad B = \frac{\partial \hat{F}}{\partial \hat{q}}; \quad C = \frac{\partial \hat{G}}{\partial \hat{q}}$$

The Jacobian matrices are given by Pulliam and Steger [98]. First,

$$\boldsymbol{A} = \begin{bmatrix} \xi_t & \xi_x & \xi_y & \xi_z & 0 \\ -u\theta + \xi_x \varphi^2 & \Theta - (\gamma - 2)\xi_x u & \xi_y u - \sigma \xi_x v & \xi_z u - \sigma \xi_x w & \sigma \xi_x \\ -v\theta + \xi_y \varphi^2 & \xi_x v - \sigma \xi_y u & \Theta - (\gamma - 2)\xi_y v & \xi_z v - \sigma \xi_y w & \sigma \xi_y \\ -w\theta + \xi_z \varphi^2 & \xi_x w - \sigma \xi_z u & \xi_y w - \sigma \xi_z v & \Theta - (\gamma - 2)\xi_z w & \sigma \xi_z \\ \theta(\varphi^2 - E) & \xi_x E - \sigma u\theta & \xi_y E - \sigma v\theta & \xi_z E - \sigma w\theta & \xi_t + \gamma\theta \end{bmatrix}$$

$$\varphi^2 = (\gamma - 1)\left(\frac{u^2 + v^2 + w^2}{2}\right)$$

$$\theta = \xi_x u + \xi_y v + \xi_z w$$

$$\sigma = \gamma - 1$$

$$\Theta = \xi_t + \theta$$

$$E = \frac{\gamma e}{\rho} - \varphi^2$$

Then, the matrices [B] and [C] are evaluated in terms of the respective generalized coordinates η and ζ. Eq. (2.33) can be rearranged as:

$$\left[I + \Delta\tau\left(\delta_\xi \hat{A}^n + \delta_\eta \hat{B}^n + \delta_\zeta \hat{C}^n\right)\right]\Delta\hat{q}^{n+1} = [RHS]^n \tag{2.35}$$

where $\Delta\hat{q}^{n+1} = \hat{q}^{n+1} - \hat{q}^n$, and I is the identity matrix. The term [RHS], referred to as the residual, is given by:

$$[RHS]^n = -\Delta\tau(\delta_\xi \hat{F}^n + \delta_\eta \hat{G}^n + \delta_\zeta \hat{H}^n) + \Delta\tau \frac{M}{\mathrm{Re}}(\delta_\xi \hat{R}^n + \delta_\eta \hat{S}^n + \delta_\zeta \hat{T}^n) \tag{2.36}$$

A second order temporal accuracy version of the current temporal scheme is also available, which uses Newton sub-iterations denoted by superscript 'l'.

$$[RHS]^{n+1,l} = -\Delta\tau\left(\delta_\xi \hat{F}^{n+1,l} + \delta_\eta \hat{G}^{n+1,l} + \delta_\zeta \hat{H}^{n+1,l}\right)$$
$$+ \Delta\tau \frac{M}{Re}\left(\delta_\xi \hat{R}^{n+1,l} + \delta_\eta \hat{T}^{n+1,l} + \delta_\zeta \hat{F}^{n+1,l}\right) - \frac{(3\hat{q}^{n+1,l} - 4\hat{q}^{n} + \hat{q}^{n-1,l})}{2}$$

In this context, $\hat{q}^{n+1,l}$ is the latest estimate of $\hat{q}$ at new time level $n+1$, and a previous sub-iteration l.

In Eq. (2.35), then $\Delta\hat{q}^{n+1}$ is viewed as

$$\Delta\hat{q}^{n+1} = \hat{q}^{n+1,l+1} - \hat{q}^{n+1,l}$$

In steady-state problems, the residual $\Delta\hat{q}$ should be reduced to an acceptably small value for the calculation to be considered converged. In time dependent or unsteady problems, however, the residual does not need to reach a minimum value and may vary with time depending on the flow situation. Equation (2.36) may be viewed as a matrix system,

$$[M]\{\Delta\hat{q}\} = [RHS] \tag{2.37}$$

Solution of Eq. (2.37) is computationally expensive because the unfactored coefficient matrix [*M*], which is a seven-diagonal matrix, requires vast computer storage and computing time to invert. In order to reduce the computational work, this sparse matrix [*M*] is approximately factored into three sparse matrices using a Lower-Upper Symmetric Gauss-Seidel (LU-SGS) implicit scheme proposed by Yoon and Jameson [99]. The LU-SGS method ensures that the matrix is diagonally dominant. This scheme is widely used to solve the compressible Navier-Stokes equations.

2.3 Geometric Conservation Law

The geometric conservation law (GCL) is used to satisfy the conservative relations of the surfaces and volumes of the control cells. In moving meshes, the GCL states that the volumetric increment of a moving cell must be equal to the sum of the changes along the surfaces that enclose the volume. Thomas and Lombard [100] formulated the differential form of the geometric conservation law. The GCL terms can be identified from the differential form of the Navier-Stokes equations in generalized coordinates.

The differential form of the Navier Stokes equations may be expressed as

$$\frac{\partial VQ}{\partial t}+\frac{\partial \hat{F}}{\partial \xi}+\frac{\partial \hat{G}}{\partial \eta}+\frac{\partial \hat{H}}{\partial \zeta}=\frac{M}{\mathrm{Re}}\left[\frac{\partial \hat{R}}{\partial \xi}+\frac{\partial \hat{S}}{\partial \eta}+\frac{\partial T}{\partial \zeta}\right] \tag{2.38}$$

Where V is the cell volume is

$$V=\frac{1}{J}$$

This can be expressed as

$$\frac{V\partial Q}{\partial t}+\frac{Q\partial V}{\partial t}+\frac{\partial \hat{F}}{\partial \xi}+\frac{\partial \hat{G}}{\partial \eta}+\frac{\partial \hat{H}}{\partial \zeta}=\frac{M}{Re}\left[\frac{\partial \hat{R}}{\partial \xi}+\frac{\partial \hat{S}}{\partial \eta}+\frac{\partial T}{\partial \zeta}\right] \tag{2.39}$$

The term $Q\frac{\partial V}{\partial t}$ is known as the GCL term and can be expressed in term of generalized coordinates as

$$Q\frac{\partial V}{\partial t}=-Q\left[\frac{\partial}{\partial \xi}\left(\frac{\xi_t}{J}\right)+\frac{\partial}{\partial \eta}\left(\frac{\eta_t}{J}\right)+\frac{\partial}{\partial \zeta}\left(\frac{\zeta_t}{J}\right)\right] \tag{2.40}$$

The refined governing equation accounting for GCL term becomes

$$\frac{1}{\mathrm{J}}\frac{\partial Q}{\partial \mathrm{t}} + \frac{\partial F}{\partial \xi} + \frac{\partial G}{\partial \eta} + \frac{\partial G}{\partial \zeta} = \frac{\partial R}{\partial \xi} + \frac{\partial S}{\partial \eta} + \frac{\partial T}{\partial \zeta} + \mathrm{RHS_{GCL}} \tag{2.41}$$

where

$$\mathrm{RHS_{GCL}} = Q\left[\frac{\partial}{\partial \xi}\left(\frac{\xi_t}{J}\right) + \frac{\partial}{\partial \eta}\left(\frac{\eta_t}{J}\right) + \frac{\partial}{\partial \zeta}\left(\frac{\zeta_t}{J}\right)\right]$$

2.4 Boundary and Interface Conditions

At the surface of the blade, the solid wall, no-slip, and adiabatic wall boundary conditions and zero pressure gradient at the wall are applied as follows:

$$\vec{V}_{wall} = \vec{V}_{grid} \qquad \text{No slip boundary condition}$$

$$\left.\frac{\partial T}{\partial n}\right|_{wall} = 0$$

$$\left.\frac{\partial p}{\partial n}\right|_{wall} = 0$$

The boundary conditions must be formulated to keep the solution physical and prevent any non-physical reflection at the boundary. The upstream and downstream Riemann invariants imposed at the far-field boundary are given by

$$\begin{aligned} R^+ &= \vec{V}_n + \frac{2a}{\gamma - 1} \\ R^- &= \vec{V}_n - \frac{2a}{\gamma - 1} \end{aligned} \tag{2.42}$$

The Riemann invariants correspond to the incoming R^- and outgoing R^+characteristic waves. Eigen values associated with the characteristic velocities are given by

$$\lambda_1 = \vec{V}_n + a$$

$$\lambda_2 = \vec{V}_n - a$$

The normal velocity vector $\vec{V}_n$ is outwardly directed from the interior computational domain. The velocity at the outer boundary consists of free-stream velocity, velocity component due to grid movement, and the induced velocity due to all the wake filaments and boundary vorticity from other blades. When $\vec{V}_n$ is negative, λ_2 is negative as well and therefore the inflow condition is applied. In such a case, if λ_1 is also negative, all the information comes from the free-stream. On the other hand, if λ_1 is positive, one piece of information comes from the interior and the others come from the free-stream. At the far-field, inboard and outboard surfaces, the characteristics based inflow/outflow boundary condition which are non-reflective are used.

2.5 Turbulence Model

In order to predict turbulent flows by numerical solutions to the Reynolds equations, it is necessary to make closing assumptions about the apparent turbulent stress. The Reynolds stress terms $\overline{u_i' u_j'}$, cannot be solved directly and therefore are modeled. Boussinesq assumption states that the apparent turbulent shearing stresses are related to the rate of the mean strain through an "eddy" viscosity concept, which is represented in the tensor form as:

$$-\rho\overline{u_i' u_j'} = \mu_T \left[\frac{\partial \overline{u}_i}{\partial x_j} + \frac{\partial \overline{u}_j}{\partial x_i}\right]$$

where μ_T is the turbulent viscosity, u_i', u_j' are the instantaneous velocity fluctuations about the mean velocity components $\overline{u}_i$ and $\overline{u}_j$ respectively and $\overline{u_i' u_j'}$ is the time-averaged value of the product u_i' and u_j'. The turbulence models currently implemented in the hybrid CFD solver are Spalart-Allmaras (SA) [101], Spalart-Allmaras-DES (SA-DES) [102], and Kinetic Eddy Simulation (KES) [103], [104].

2.5.1 Spalart Allmaras Model

Some of the key features of the SA model are described. The SA model uses the Boussinesq approximation to relate the Reynolds stresses to a kinematic turbulent eddy viscosity and the mean strain-rate tensor.

$$\nu_t = \tilde{\nu} f_{v1}$$

The transport equation for the variable $\tilde{\nu}$ is given by

$$\frac{D\tilde{\nu}}{Dt} = \underbrace{C_{b1}\tilde{\nu}\left(\Omega + \frac{\tilde{\nu}}{k^2 d^2} f_{v2}\right)}_{\text{Production}} - \underbrace{C_{w1} f_w \left(\frac{\tilde{\nu}}{d}\right)^2}_{\text{Dissipation}} + \underbrace{\frac{1}{\sigma}\left[\nabla \cdot \left((\nu + \tilde{\nu})\nabla\tilde{\nu}\right) + C_{b2}(\nabla\tilde{\nu})^2\right]}_{\text{Diffusion}}$$

The terms on the right hand side consist of the source terms for production, dissipation and diffusion. The turbulent length scale *d* is defined as the distance to the nearest wall. The functions f_{v1}, f_{v2}, f_w and the model constants $C_{b1}, C_{b1}, C_{b1}, k, \sigma$ are described in detail by Spalart and Allmaras [101]. Ω represents the magnitude of vorticity.

2.5.2 Spalart-Allmaras Detached Eddy Simulation (SA-DES)

For modeling separated flows, an extension to the SA model has been proposed by Spalart [102] which blends the RANS turbulence model in boundary layers, together with coarse-mesh LES in regions of separated flow. This approach is called the SA-DES model. Within the boundary layer, the turbulent scales are very small and need to be modeled, and therefore the DES model operates in RANS mode. Outside the boundary layer, SA-DES switches to an LES-type model, where the turbulence scales are well resolved by the grid. In regions away from the wall, this definition is replaced by the maximum cell size as follows:

$$\tilde{d} = \min\left(d, C_{DES}\Delta\right)$$

where $\Delta = \max\left(\Delta x, \Delta y, \Delta z\right)$. The model constant used in this study is $C_{DES} = 0.65$.

2.6 Rotor Inflow Modeling

In low speed operations, the rotor flow environment is strongly modified by the interaction between the rotor blade and the vortices shed from the neighboring blades. The ability to predict this wake is important, especially for blade-vortex interactions (BVI) in forward flight. In addition to the near wake, the rotor far wake that extends up to 4-6 rotor diameters needs to be captured or modeled to accurately predict the rotor inflow field. The requirement that the vortex core in the far wake be resolved without dissipation can make CFD wake capturing methods like OVERFLOW computationally expensive. GT-Hybrid CFD solver utilizes a hybrid methodology where the flow field near the blade is resolved through the Navier-Stokes solution, whereas the influence of the other blades and of the trailing vorticity in the far field wake are accounted for by modeling them as a collection of piece-wise linear bound and trailing vortex elements. The near wake is captured inherently in the Navier-Stokes analysis. The use of such a hybrid Navier-Stokes/vortex modeling method allows for an accurate and economical modeling of viscous features near the blades, and an accurate "non-diffusive" modeling of the trailing wake in the far field.

2.6.1 Rigid/Free Wake Model

The vortex model is based on a Lagrangian wake approach where a collection of vortex elements are shed from the rotor blade trailing edge. This wake model is based on the assumption that all shed vorticity from blade coalesce downstream into a strong tip vortex. The convection of the tip vortex elements depends on differing approaches – rigid wake or free wake model. In the rigid wake model, the wake elements are non-distorting hence they maintain their initial helical structure and they are convected at a speed determined by linear superposition of free stream velocity components and a uniform inflow velocity. This inflow velocity is determined using the Prandtl-Glauert's formula [105]. The convection velocity components in free/distorting wake model include velocity components induced by wake elements on each other in addition to above mentioned velocity components. The effect of bound vortex is also included for computation of self-induced velocity components. These self-induced velocity components are determined using the Biot-Savart law. Free wake methods provide more generality with a minimum dependence on experimental data but they are also computationally more expensive than rigid wake modeling.

In the current implementation, the free/rigid wake model is initialized with prescribed wake geometry. The wake strengths are initialized using an analytical model developed by Mello *et al.* [106]. The number of revolutions of the wake preserved in the model is chosen by the user. In forward flight, 3 to 5 wake revolutions are chosen, depending on the advance ratio. In the hybrid method, the wake strength and geometry are assumed to vary periodically with blade azimuthal location. New wake filaments are added at the vortex shedding point as the rotor is advanced in the azimuthal direction. To keep the fixed number of wake elements small, the oldest elements are dropped from the end of the wake. The induced velocity components and wake geometry distortion are updated for all wake elements each time new wake filaments are shed. Also, in order to reduce the computational cost, the frequency of updating the wake distortion can be controlled, permitting induced velocity and wake geometry updates at periodic azimuthal intervals. The free wake model is a better physical representation of the wake than a rigid wake model, and therefore it is used for all the studies presented in this work.

2.6.2 Navier-Stokes/Wake Model Coupling

The wake model derives its vortex strength from the Navier-Stokes solution. The effect of the wake model on the Navier-Stokes solution is accounted for by applying wake induced velocity components as a boundary condition on Navier-Stokes far-field boundaries. This coupling between the Navier-Stokes solution and wake model is explicit in nature. The effect of the wake lags the Navier-Stokes solution. The strength of the vortex elements in the tip vortex is set to be equal to the peak bound circulation on the rotor blade at the instant the element is shed. The peak bound circulation is obtained from airloads predicted by Navier-Stokes solution using the Kutta-Joukowski theorem. The shedding point of the vortex element is based on the centroid of trailed circulation between the tip and location of peak bound circulation. The wake induced velocity components are computed at domain boundary points using the Biot-Savart law. The wake trailers used for boundary condition computation includes trailing and bound wake from all blades but neglects the contribution of the elements within the CFD volume grid trailed immediately from the blade. It is necessary to exclude the wake trailers inside the CFD volume grid to avoid double counting the vorticity already captured by the Navier-Stokes solution. An imaginary bounding box is used to determine whether a wake marker is inside or outside the Navier-Stokes domain. The induced velocity of the wake trailers inside the bounding box is not considered.

2.7 Multiple Trailer Wake Model

The wake model represented by a single concentrated tip vortex trailing from a region near the blade tip assumes that all inboard wake is either weak or coalesces into the tip vortex immediately that the effect of inboard wake can be easily ignored. This assumption would be appropriate for high speed flight but would be physically less accurate for rotors in low speed forward and descent flight since location and strength of the inboard vortices are critical for predicting blade vortex interaction (BVI) phenomena. To address this issue, full-span wake model or multiple trailer wake model was implemented in the GT-Hybrid solver as an alternative to the tip vortex model. The multiple trailer wake model is based on Prandtl's lifting-line theory [107]. For a three-dimensional blade, the bound vorticity, located at quarter chord line of the blade is trailed into the wake from the blade tip and root. Vorticity is also shed from the blade mid-span regions because of radial changes in the bound circulation. Therefore, the single tip vortex is replaced by user specified number of multiple vortex segments trailed from all the blades. The trailers are equally distributed along the blade span. The strength of the vortex elements is based on radial gradient of bound circulation and number of wake trailers chosen by the user. The vorticity strength of first wake element of trailer *n* at any azimuthal position Ψ is given by

$$\Gamma_{tr}(\Psi, n) = \Gamma(\Psi, n+1) - \Gamma(\Psi, n) \tag{2.43}$$

The geometry of the far wake undergoes distortion due to the influence of the self-induced velocity components and also due to the time rate of change in circulation of each wake trailer segment. The multiple trailer wake model uses the Vatistas core model [108], [109] and the Bhagwat-Leishman core growth model [110]. Turbulence in the tip vortex affects the diffusion of vorticity, and these effects were incorporated using an empirically validated correction for the average apparent or "eddy" viscosity. The vortex induced velocity profiles measured in experiments were found to exhibit strong self-similarity when using the vortex core radius as a length-scale, suggesting that a generalized model is possible. This model accounts for the effect of both laminar and turbulent viscosities on viscous core growth. The analytical expression for the core growth is given as follows,

$$\begin{aligned} r_c &= \sqrt{4\alpha\delta\nu\left(\frac{z+z_0}{V_\infty}\right)} \\ \delta &= 1 + a_1 \operatorname{Re}_v \end{aligned} \tag{2.44}$$

where $\vec{r_c}$ is viscous core radius, a_1 and α are empirical parameters, V_∞ is freestream velocity.

The use of the multiple trailer model significantly increases computational time because the calculation of wake geometries scale approximately as n^2 where n is the number of wake trailers. A comparison of single tip vortex model vs. multiple trailer model on airloads predictions for UH-60A will be addressed in the next chapter.

2.8 Shed Wake model

The multiple trailer vortex does not include the wake shed due to temporal change in bound vorticity strength. Kelvin's theorem [107] states that the circulation around a closed curve moving with the fluid remains constant with time. This means a counter-rotating vortex is shed equal in magnitude to the change in bound circulation. This additional wake is modeled through a shed wake model. The effect of the shed wake on the source blade is adequately captured by the Navier-Stokes solution but its effect on adjacent blades needs to be modeled. The vorticity strength of wake element shed between trailer n and $n+1$ at azimuth Ψ is given as follows,

$$\Gamma_{sh}(\Psi, n) = \Gamma(\Psi, n) - \Gamma(\Psi - \Delta\Psi, n) \tag{2.45}$$

Even though the wake is shed continuously, new shed wake elements are created only at periodic azimuthal intervals for computational efficiency. The viscous core growth for shed wake elements is modeled in the same way as for the trailed wake elements. The effect of the shed wake model on airloads predictions will be addressed in the next chapter.

2.9 Computational Grid

The computational grid used in GT-Hybrid is based on C-H grid topology. The baseline grid has $131 \times 65 \times 45$ nodes in chordwise, spanwise and normal directions, respectively. The blade surface has 91 chordwise points and 50 spanwise points. The far field boundary is located about nine chord lengths away from the blade surface. The normal grid spacing at the blade surface is about $1 \times 10^{-5}c$, where c is the reference chord length. This grid spacing corresponds to a y^+ of $O(1)$ for all the flight conditions tested in this study. The grid is clustered near the tip and near the leading and trailing edges to handle regions of high gradients. Additionally finer grids $263 \times 65 \times 90$ and $263 \times 128 \times 90$ were also used in this research effort to more accurately capture compressibility effects for maneuvering flight conditions. The baseline grid with C-H topology is shown in Figure 2.1.

2.10 Grid Deformation

Rotor blades are long, slender and flexible. This makes them extremely susceptible to structural deflections and three types of deformations. To compute the airloads on a rotor blade, the CFD methodology needs to account for these deformations. These deformations are applied to the computational grid using the methodology specified in this section.

The blade motions obtained from the CSD analysis includes linear (Δx, Δy, Δz) and rotational deformations ($\Delta\phi$, $\Delta\theta$, $\Delta\psi$). These deformations are written out as a function of azimuth and radial station. These blade motions are interpolated using a bi-linear interpolation scheme from CSD to CFD radial stations and to intermediate azimuthal points to match the CFD azimuthal time step. The rotational deformation is applied to the initial un-deformed grid following an updated *x-y-z* sequence of the orientation angles rotation around the reference point as follows.

$$\begin{bmatrix} x \\ y \\ z \end{bmatrix}_r = L_r \left[\begin{bmatrix} x \\ y \\ z \end{bmatrix}_{initial} - \begin{bmatrix} x \\ y \\ z \end{bmatrix}_{ref} \right]$$

$$L_r = L_3(-\Delta\psi) L_2(-\Delta\theta) L_1(-\Delta\phi) \tag{2.46}$$

$$= \begin{bmatrix} CS \cdot CT & -SS \cdot CF + ST \cdot CS \cdot SF & SS \cdot SF + ST \cdot CS \cdot CF \\ SS \cdot CT & CS \cdot CF + SS \cdot ST \cdot SF & -CS \cdot SF + SS \cdot ST \cdot CF \\ -ST & CT \cdot SF & CT \cdot CF \end{bmatrix}$$

Where:

$$CS = \cos(\Delta\psi), CT = \cos(\Delta\theta), CF = \cos(\Delta\phi)$$

$$SS = \sin(\Delta\psi), ST = \sin(\Delta\theta), SF = \sin(\Delta\phi) \tag{2.47}$$

Here, $[x \quad y \quad z]^T_{initial}$ is the initial grid coordinates placed at 0 degree azimuth without pre-cone, elastic deformation, flapping and pitch control input, but with built-in twist angle. The point, $[x \quad y \quad z]^T_{ref}$, is the reference point, where the deformations were obtained after interpolation. Note that the expression above represents rotation applied to the grid point with positive $\Delta\phi$, $\Delta\theta$, and $\Delta\psi$ angles. Thus, the angles in the rotational matrixes (L_1, L_2, L_3) for the axis have negative sign. The final grid at the desired azimuthal angle is then obtained after applying linear transformation, pre-cone angle and rotation to the azimuthal location as follows.

$$\begin{bmatrix} x \\ y \\ z \end{bmatrix} = L_{IB}\left[\begin{bmatrix} x \\ y \\ z \end{bmatrix}_r + \begin{bmatrix} x \\ y \\ z \end{bmatrix}_{ref} + \begin{bmatrix} \Delta x \\ \Delta y \\ \Delta z \end{bmatrix}\right]$$

$$L_{IB} = L_3(-\Psi)L_2(\theta_p) \tag{2.48}$$

$$= \begin{bmatrix} \cos\Psi\cos\theta_p & -\sin\Psi & -\cos\Psi\sin\theta_p \\ \sin\Psi\cos\theta_p & \cos\Psi & -\sin\Psi\sin\theta_p \\ \sin\theta_p & 0 & \cos\theta_p \end{bmatrix}$$

Here Ψ is the azimuthal angle (+, counterclockwise from top view), and θ_p is the pre-cone angle (+, flap up). Again, note that the angles in the rotational matrixes have the opposite sign of the grid rotation. The positive pre-cone angle is defined as flap-up direction, which is the opposite of the right hand rule. Thus, its sign in the rotational matrix is positive.

The grid deformation may be gradually reduced from the blade surface to the outer boundary of the computational domain using a decay function, so that the outer boundary remains undeformed. However, deformations observed in this study were small, and the same deformations have been applied at a radial location throughout the constant spanwise plane.

2.11 CSD Methodology

DYMORE [38], [40] is a computational structural dynamics (CSD) solver used in this study. It is a multi-body finite element code for arbitrary non-linear elastic systems. The multi-body models are constructed by connecting basic structural elements; the data for these elements are stored within an element library. Each of these elements has its own system of equations which when integrated create larger and more complex equations. The multi-body code incorporates robust and efficient time integration algorithms for integrating the resulting large scale, nonlinear, differential or algebraic equations. The rotor blades are modeled as elastic beams with geometrically exact composite beam finite element formulation. Rotorcraft comprehensive analyses solvers typically include internal lifting line based aerodynamic model as well as autopilot algorithm which can be used to perform a fully trimmed aeroelastic simulation of an isolated rotor configuration. DYMORE has been used extensively by researchers for performing comprehensive analyses because of the in-built lifting line aerodynamics, non-linear inflow models as well as auto-pilot trimmer. DYMORE can be coupled to external CFD solver to perform aeroelastic computations. In the simulations presented in this study, a four bladed UH-60A rotor model is used. The model includes blade, lag damper, pitch link, rotor hub and swash plate. A lifting line based 2-D table lookup aerodynamics with dynamic wake model is used for computing airloads internally.

2.12 Loose Coupling Methodology

The CFD solver (GT-Hybrid) and CSD solver (DYMORE) communicate in a loosely coupled manner. The delta-trim algorithm or loose coupling procedure pioneered by Tung, Caradonna and Johnson [111] is used to obtain trim solution and convergence of the CFD/CSD coupled analyses. The delta trimming methodology is an incremental formulation, wherein the methodology replaces the comprehensive airloads with CFD airloads while using lifting line aerodynamics to trim and CSD for accounting for blade deformations. The schematic of the delta-trimming methodology is shown in.

At the beginning of the coupling process, the comprehensive analysis computes initial quarter chord motions as a function of radius and azimuth, by utilizing the internal lifting line aerodynamic solution. The computed elastic blade deformations of the quarter chord are then given as input to the CFD solver which in turn solves for the flow-field. This concludes the first CFD/CSD iteration.

$$F_0 = F_0^{LL} \tag{2.49}$$

For the subsequent coupling iterations, the aerodynamic forces and moments used in the comprehensive analysis are the comprehensive lifting line solution (LL) required to trim plus the correlation based on CFD. The difference between the CFD airloads and the lifting line airloads from the previous iteration, are added to the lifting line solution for the current iteration. Thus, the total airloads within the comprehensive solver are incrementally replaced by the airloads predicted by external CFD code, in an iterative manner.

$$F_n = F_n^{LL} + (F_{n-1}^{CFD} - F_{n-1}^{CFD}) \tag{2.50}$$

Upon convergence, the forces do not change between subsequent iterations because no trim or aeroelastic changes are required. All trim constraints are satisfied by the final CFD solution. There is a possibility that while trying to trim, the lifting line aerodynamics will move the solution in the wrong direction. This might be a problem when parts of the rotor are stalled. During the delta-trimming methodology, it is not necessary for the flow solution to be fully converged, which provides a form of relaxation. If the CFD solution is used as a restart condition for the current CFD calculation, for a 4-bladed rotor, ¼ of a revolution is sufficient, since the flow is assumed to be periodic over the 4 blades. The final coupled solution is converged when the collective and cyclic control angles and CFD aerodynamic forces do not change between iterations. Upon convergence the total airloads used in the comprehensive analysis are CFD airloads. GT-Hybrid outputs the surface grid, flow variables, at user-specified intervals. It is not necessary to save the flow-field. The post-processed files consist of normal force, pitching moment, chord force as a function of radius and azimuth.

2.13 Maneuver Simulation Methodology

Maneuvers are characterized as steady and transient. The assumption for steady maneuvers is that forces acting on the helicopter act in equilibrium. A level banked turn is considered an example of a steady maneuver. For a coordinated turn, the only accelerations experienced by the flapping blade are centrifugal force and out of plane motion of a flapping blade. However, a transient maneuver is characterized by non-zero accelerations. These accelerations could be nominal. In a transient maneuver, the hub is free to translate and rotate and therefore the velocities and accelerations of the hub contribute to the accelerations at a blade element. These accelerations at the blade element must be considered in the simulations. In this section, the modifications required in the current methodology to account for the hub motion are reviewed.

The reference frame in DYMORE is the hub/shaft frame. Assuming that the aircraft CG moves with time-varying velocity components u,v,w and p,q,r under the action of applied forces X,Y,Z and L,M,N, the hub velocity components in the hub/shaft reference system are related to the C.G. velocities through the following transformation

$$\begin{bmatrix} u_h \\ v_h \\ w_h \end{bmatrix} = \begin{bmatrix} \cos\gamma_s & 0 & \sin\gamma_s \\ 0 & 1 & 0 \\ -\sin\gamma_s & 0 & \cos\gamma_s \end{bmatrix} \begin{bmatrix} u - qh_R \\ v + ph_R + rx_{CG} \\ w - qx_{CG} \end{bmatrix},$$

where γ_s is forward shaft tilt, $h_R$is the distance between hub and C.G. in the negative z-direction and x_{CG} is the distance between the hub and the CG in the x-direction. A kinematic link must be added in the CSD methodology to account for the difference between the shaft and the C.G. motion. Alternatively, calculated flight test hub velocities at the shaft may be specified in the CSD methodology. The components of gravitational force are obtained in the body frame using the Euler transformation, which consists of a series of rotations, first rotation by the heading angle (ψ), followed by a pitch rotation (θ) and finally a roll rotation (φ). The wind vector is transformed from the wind frame to the body frame. This involves two rotations: first, a rotation about z_w axis through $-\beta$ followed by a rotation about the y-axis through α.

2.14 CFD/CSD Modeling Changes for Quasi-Steady Maneuvers

The reference frame for the loosely coupled CFD simulations is the non-rotating hub/shaft frame. Therefore, modifications were made to simulate the hub motion. In the CFD and CSD methodologies, the free-stream conditions are superceded by shaft motion. The fuselage is modeled as a massless rigid beam with end nodes at C.G. and hub center. Rotor model is changed from single blade to multi-blade. For periodic rotor dynamics, a single blade solution may serve as initial conditions for an unsteady maneuver.

During the simulation of a maneuver, the grid points in the CFD grid see additional velocity components due to the translation as well as the angular motion of the hub. These hub velocities are included through grid velocity components to avoid reorienting the computational grid. The vehicle global frame motions namely the translatory hub motion is accounted for through FSI using the orientation and velocities of DYMORE vehicle frame. Additionally, the wake geometry is made to evolve with respect to an observer on the hub. For loosely coupled trim calculations, inclusion of hub motion through grid metrics ensures that the correct vehicular attitudes are transmitted to the CFD solver as the trim solution advances. In the tightly coupled methodology, the effective free-stream velocity in CFD changes with time as vehicle orientation changes. This is implemented in the CFD solver through the use of a text file.

2.15 Enhancements to GT-Hybrid 3.51

The version of hybrid solver that is used in the current study is GT-Hybrid-3.51. The current version implements several enhancements which are documented as follows:

1. In the parallel version of the solver, the computational domain is split along the spanwise direction according to the number of computational cores for obtaining Navier-Stokes solution. Efficient handling of memory and accession were implemented which resulted in an increased computational efficiency of the solver. Enhancements to memory handling also increased the maximum size of computational grids that can be handled by the CFD solver. This was done by ensuring that each processor has access only to the grid points belonging to the zone assigned to it.
2. Two separate versions of the solver - loosely and tightly coupled codes were combined into a common single source code. In the latest version of the hybrid solver, the user can choose either loose or tight mode during compilation.
3. The code was extended to compute integrated hub loads for studying performance of the rotor

4. The hybrid code fixed wing mode of the solver, resulted in an over-prediction of viscous drag which was resolved.

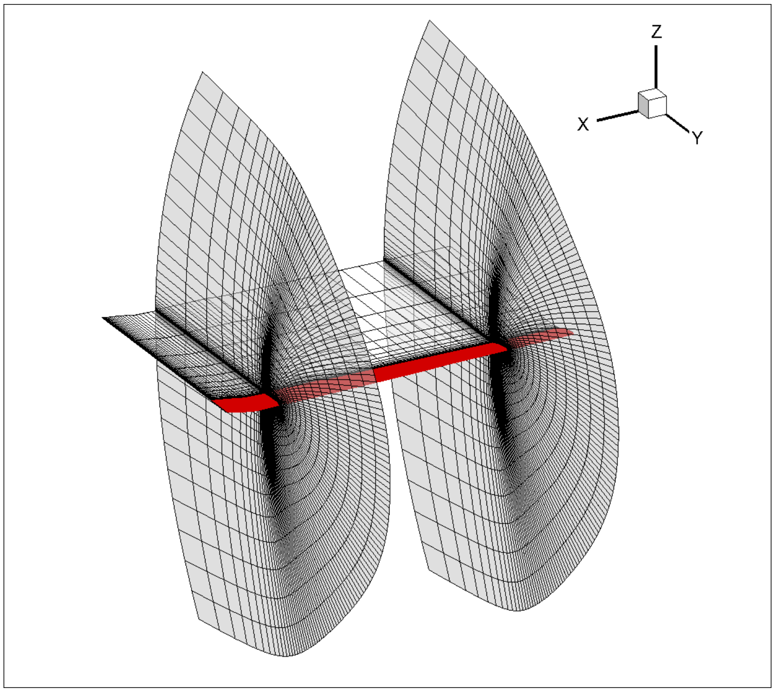

Figure 2.1 Baseline computational grid of C-H topology consisting of 131×65×45

CHAPTER 3

VALIDATION STUDIES

In this chapter, the effect of aerodynamic modeling parameters on the quality of airloads prediction will be assessed. The quality of the predicted airloads dictated by the quality of the CFD grid, the effects of wake effects on the rotor and subsequently the induced inflow. An accurate CAD based rendering of the blade surface is important for high fidelity aerodynamics and structural analyses. Other parameters affecting the quality of the predicted loads include turbulence model, CFD grid density, representation of trailing vortices and shed wake, and interpolation effects associated with the transfer of information between the CFD solver and the CSD solver. In order to determine the effects of these crucial parameters on the structural loads, a series of assessment tests were first performed for selected steady flight counters of the UH-60A Airloads Program.

3.1 Effect of CAD Based CFD grid on Computed Loads

The effects of a blade surface representation extracted from a CAD surface geometry, relative to the baseline grid geometry, were studied to determine the degree to which the nominal surface geometry changes between these two definitions affects the quality of predicted loads. The differences between the two grids, apart from the CAD surface representation is that the baseline grid has a trailing edge with finite thickness and the radial position of its trim tab differs by 3 inches from the actual geometry of the UH-60A blade. It is to be noted that neither of the grids model the shank shaft which produces drag penalties at very high advance ratios.

The normal loads and pitching moments for the baseline grid vs. CAD-based grid for high speed steady level flight counter 8534 are shown in Figure 3.1 and Figure 3.2. These results indicate that the CAD based grid captures the peak-to-peak marginally better, from the midspan to the outer-board regions. This may be attributed to the fact that the trim tab, the swept part of the blade tip and the trailing edge regions are better modeled in the CAD geometry based grid. However, the air loads in the fourth quadrant do not show any improvement with this grid. The CAD based representation of the surface geometry improves the inboard and mid-span load predictions. The improved grid is used for all the subsequent studies in this thesis.

3.2 Effect of Wake model on Computed Loads

The primary motivation for using full span wake trailer model is to account for the effect of inboard vortices. The single tip vortex model ignores the effect of inboard wake based on the assumption that all inboard wake is either weak or coalesces into a strong tip vortex. This representation although appropriate for high-speed flight, is inadequate to capture inboard variations of vorticity at low speed flights. The full span wake/ multiple trailer model in GT-Hybrid, is based on the radial gradient of bound circulation.

Figure 3.3 depicts the single vs. multiple trailer representations in GT-Hybrid. In the current implementation, the trailers are distributed equally along the spanwise direction. CFD/CSD simulations for the high speed flight counter 8534, using 1 trailer and 15 wake trailers as depicted in Figure 3.4. It was observed that the inboard normal loads on the advancing side were captured accurately in phase and peak-to-peak only upon using the multiple trailer representation. Currently since the multiple trailer model is not fully parallelized, the cost of computations scales as n^2, where n is the number of trailers. The vortex trailed from inboard regions is significant enough to affect the loading on the advancing blades. It was found that the multiple trailer representation predicts the strength and geometry of these inboard vortices effectively, as seen from the inboard locations such as – 22.5% and 40%R. (Figure 3.4).

3.3 Effect of Shed Wake on Computed Loads

The effects of the shed wake that are not captured directly in the CFD simulation were examined by including shed wake filaments in the free wake model of the GT-Hybrid methodology. In most cases, the effect of the shed wake was found to be negligible, presumably because the near shed wake (up to 6 chords downstream of the rotor blade) was reasonably captured by the CFD simulation and generally the strength of the shed wake is much weaker than the trailed wake so that it is not required in the far wake model. However, in high thrust cases like counter 9017, dynamic stall events occur on the retreating side causing rapid azimuthal variations in lift and bound circulation. Vortex shedding is observed. In general, the strength of the shed vortices is large when dynamic stall events occur, which results in a higher magnitude of downwash. It is presumed that this shed vorticity should be included in the far wake model such that the following blade will experience its effect. It was found that the inclusion of the shed wake model for counter 9017 resulted in an improved dynamic stall prediction as shown in Figure 3.5.

3.4 Effect of Turbulence Model on Computed Loads

The effect of turbulence models discussed in Chapter 2 was assessed on the airload prediction quality for high speed flight counter (8534) using the same set of blade prescribed motions. This isolates the effect of the response on the aerodynamic model.

For the flight counter studied, the compressibility effects were better captured using the SA and SA-DES models, which predicted the magnitude and phase of the advancing shock more accurately, as seen in Figure 3.6. There was marginal difference found in the prediction quality of SA and SA-DES models in capturing the transonic phenomena. The SA-DES model was chosen for subsequent studies in the thesis because of its ability to predict massively separated flows characteristic of maneuvering flight conditions. When using a coarse CFD grid, the SA-DES turbulence model may not show significant differences compared to the baseline SA model. In order for the SA-DES model to resolve smaller turbulence length scales, finer grids must be employed.

3.5 Interpolation of Loads

The DYMORE blade model of UH-60A rotor used in the present work, validated by Liu [112], consists of 99 stations. In the previous simulations, blade motions were transferred to the CFD grid at only 24 locations. Motions at other locations were linearly interpolated. For the current computations, loads were exchanged at all the 99 available spanwise stations. It was found that increased number of spanwise stations available for interpolation had negligible effect on the quality of the airloads, giving an increase in thrust by only 1%.

The prediction quality of airloads using various parameters may be quantitatively assessed by using a metric introduced by Bousman *et al.* [113] which has been documented in Appendix A.

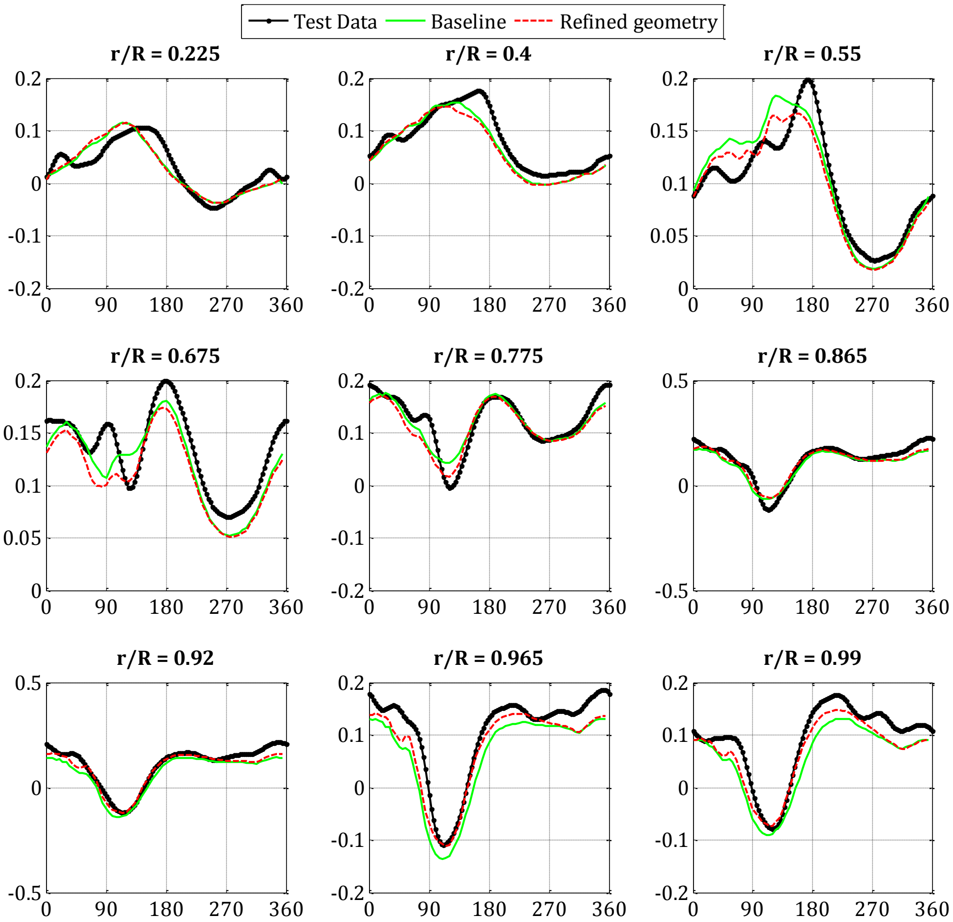

Figure 3.1 Comparison of non-dimensional sectional normal loads for counter 8534 using regular and CAD-based grid at different radial locations

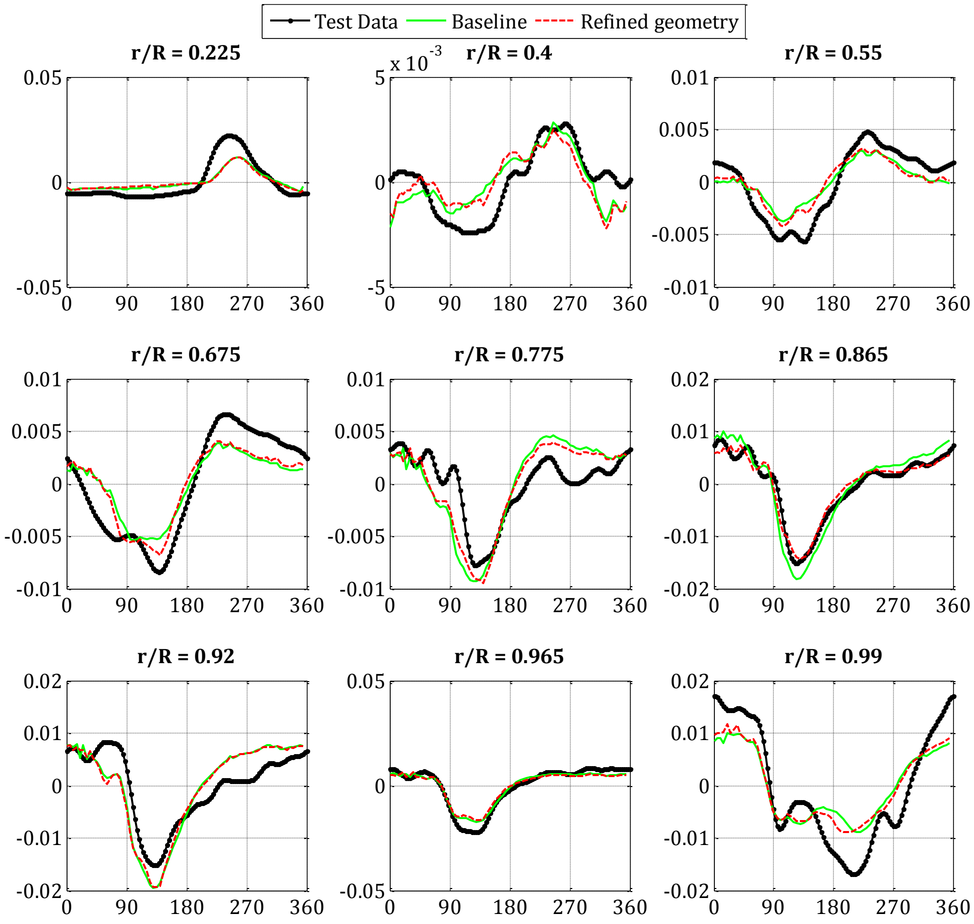

Figure 3.2 Comparison of non-dimensional sectional pitching moments for counter 8534 using regular and CAD-based grid at different radial locations

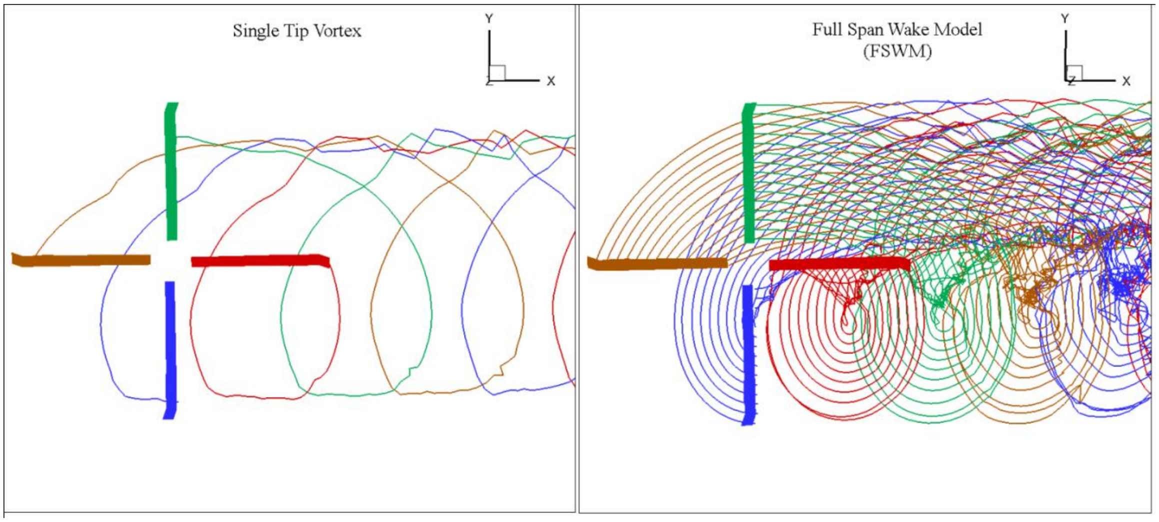

Figure 3.3 Single tip vortex representation vs. multiple trailer model

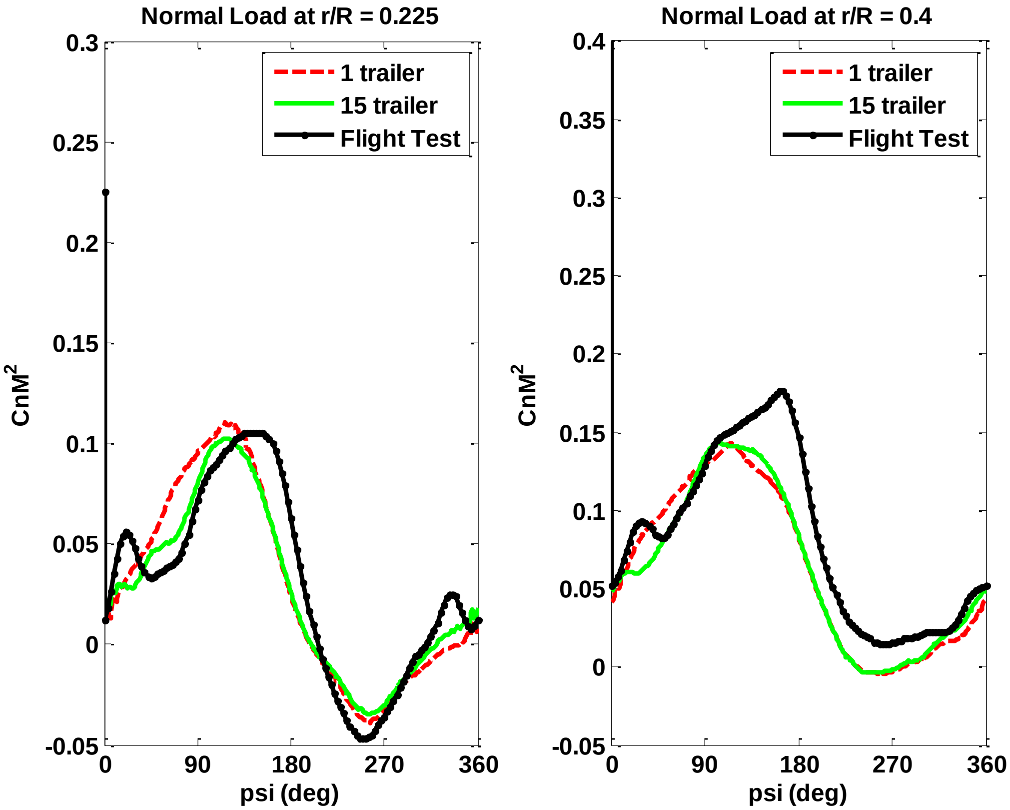

Figure 3.4 Effect of single tip vortex vs. multiple trailer representation on inboard sectional normal loads for a rotor in high speed counter 8534

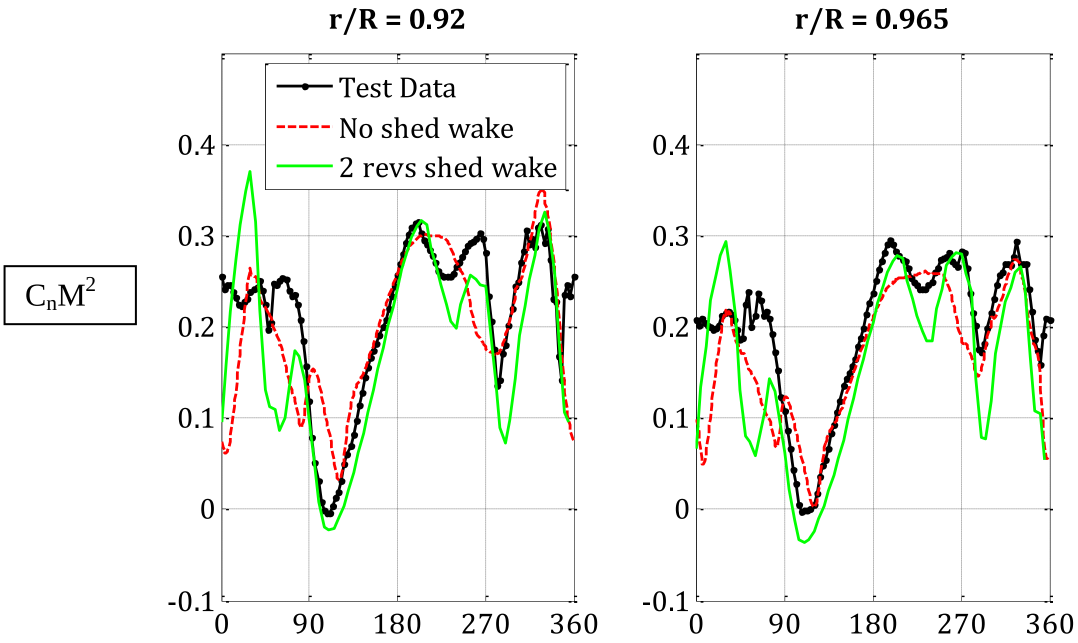

a. Sectional normal loads near tip region for high-thrust counter 9017

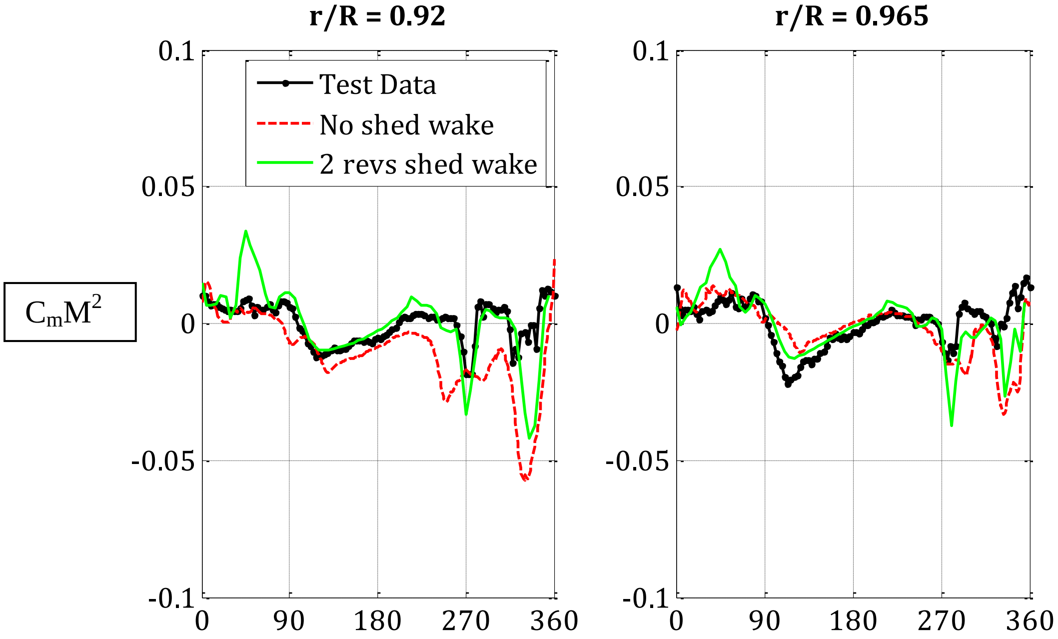

b. Sectional pitching moments near tip region for high-thrust counter 9017

Figure 3.5 Influence of shed wake on load prediction for high thrust counter (9017)

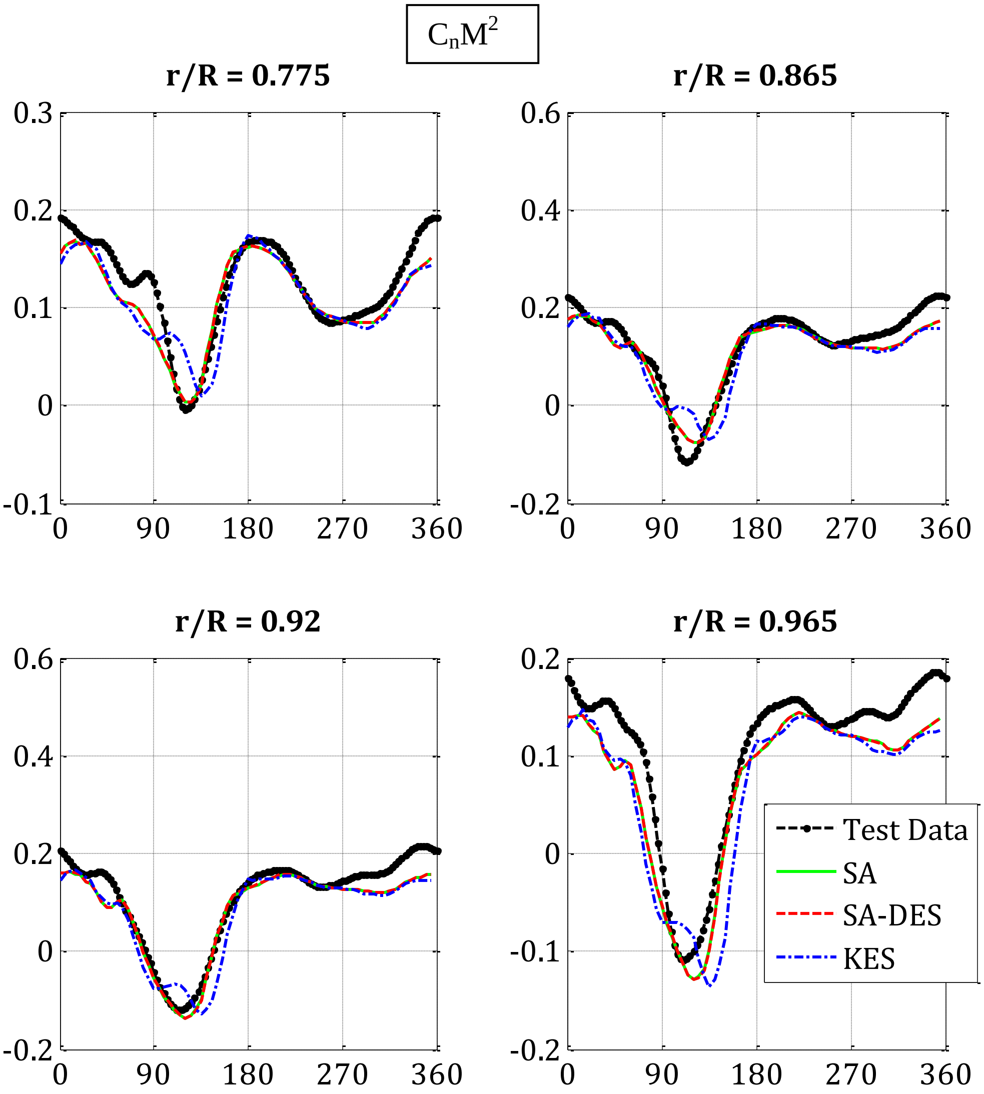

Figure 3.6 Effect of turbulence models (SA, SA-DES and KES) on the sectional normal loads at out-board radial stations for high-speed flight counter (8534).

CHAPTER 4

UH-60A WIND TUNNEL VALIDATIONS

A number of researchers have attempted to acquire reliable test data for the UH-60A rotor in forward flight. One excellent set of data is by Norman *et al.* [23] consisting of a comprehensive set of wind tunnel test conditions for the full-scale UH-60A rotor. In this chapter, the full-scale wind tunnel data for the UH-60A rotor will be used to compare measured rotor airloads, structural loads and performance indicators with predictions. Two specific parametric sweeps are investigated in the current work. The first parametric sweep study consists of a range of advance ratios, $\mu = 0.15$ to 0.4, at constant lift ($C_L/\sigma = 0.09$) and constant tip Mach number of 0.65. The second study consists of a thrust sweep from a lightly loaded rotor through deep stall conditions, at a constant advance ratio ($\mu = 0.3$) and a constant tip Mach number of 0.625. The goal is to utilize the high-quality wind tunnel data to validate the present computational methodology without uncertainties associated with the flight test data.

This chapter is arranged as follows. The test procedure and instrumentation and available data are first discussed. The experimental and computational trim procedure are discussed. The computed and measured trim values are presented. Because the integrated thrust, propulsive force, lift to drag ratio and power values are often of interest in rotorcraft design, these quantities are discussed next. This chapter concludes with discussions on airloads and structural loads.

4.1 Description of the Test

The experiment was conducted at the NFAC 40-by 80-foot wind tunnel using the UH-60A rotor system mounted on the Large Rotor Test Apparatus (LRTA). Figure 4.1 shows the rotor installed in the wind tunnel. The experiment has been described in detail by Norman *et al.* [23]. In the current section the blade instrumentation and test procedure will be reviewed.

4.1.1 Instrumentation

Two of the blades were heavily instrumented: one with 242 pressure transducers and the other with strain gauges. The pressure blade was built with 242 sub-miniature pipette-type absolute pressure transducers embedded below the skin surface of the blade. The majority of the transducers were located in one of the nine chordwise arrays, with the remainder located near the blade leading-edge in order to determine blade vortex interaction locations. The location of the pressure transducers on the blade is shown in Figure 4.2. The chordwise transducers were spaced in a Gaussian distribution to enable accurate integration of the measured radial loads.

The blade normal, edgewise and torsional moments were measured with a total of 26 two- or four-leg strain-gage bridges bonded to the second instrumented blade. The gages were located at the blade root (11.3% R) and evenly distributed along the blade at 10% increments of rotor radius (20% to 90%). Most of the gauges were bonded directly to the blade spar and used during the Airloads flight test. Five additional torsion gauges were bonded to the blade skin, including one at the same radial station as a spar-bonded gauge to ensure measurement consistency. The blades were calibrated statically prior to testing. Separate calibrations were performed for flap bending, chord bending, and torsional moments, and corrections were made for the blade twist distribution in the applied loading. Gauge cross-coupling effects were accounted for in the calibration. The cross coupling among flap bending, chord bending, and torsion moments was found to be small for the conventional operating conditions [23]. Yeo *et al.* [26] noted that the cross coupling was sometimes significant at the high advance ratio cases due to the changes in the relative magnitudes among flap bending, chord bending, and torsion moments.

The blade motions were measured using two independent specially designed blade motion measurement systems, which determined the blade flap, lag, and pitch angles at the root of each blade. The first system, designated the blade motion hardware (BMH) or "crab arm," was used during the Airloads flight test [9]. The BMH comprises mechanical measurement devices that span the main rotor blade hinge points and includes three rotary variable differential transformers (RVDTs) on each blade to measure the relative motions of its own articulations. The true blade motions are obtained through three kinematic equations that account for the cross coupling between measurements. The second system, designated the rotor state measurement system, is composed of four sets of three laser distance transducers (one set mounted to each hub arm). Each transducer produces a laser beam that is reflected back to a sensor in the same enclosure by reflective objects within a specified distance range. The transducer then produces a voltage proportional to the distance to the object (and related to one of the blade root angles). The accuracy of these blade root motion measurement systems is currently under review.

The LRTA includes a five component rotor balance to measure steady and unsteady rotor hub loads (normal, axial, and side forces plus pitch and roll moments).

Additionally, the LRTA has an instrumented flex coupling which measures rotor torque and residual normal force. Additional details on the LRTA's capabilities and functionalities are described by Norman *et al.* [23].

The blade pressure data were acquired at 2048 samples per revolution (rev). The motion and load data were acquired at 256/rev. Data used in this paper were averaged over 128 revolutions.

4.1.1 Rotor Experimental Trim Procedure

The trim controller was designed to continuously control up to three trim parameters through collective, longitudinal cyclic, and lateral cyclic pitch commands to the dynamic actuators. Parameters available for control during this test included rotor thrust or lift, hub pitching and rolling moment (from the LRTA balance), hub pitching and rolling moment (from a moment gage on the UH-60A shaft extender), and lateral and longitudinal flapping (from the BMH flapping RVDT on the pressure blade). Either dimensional or non-dimensional parameters could be specified. In addition, the rotor propulsive force could be set through manual changes to the model shaft angle. The trim controller calculated the shaft angle change required to obtain the desired propulsive force based on a look-up table of the propulsive force sensitivity to shaft angle change. Typically one or two shaft angle change iterations were required to converge on the desired rotor propulsive force.

Precise force and moment trim values were then entered into the trim controller operator interface and the trim controller was activated in 'continuous' mode to drive the dynamic actuators to reach the desired condition. The trim controller continually updated the swash-plate commands to maintain the desired trim condition throughout the duration of the data point. Trimming to propulsive force required changes to the model shaft angle. These changes were calculated by the trim controller and the shaft angle was changed manually. During this shaft angle change, the trim controller remained in ‘continuous’ mode to hold the other trim parameters (typically rotor lift and hub pitch and roll moments) at the desired values.

4.1.2 Test Procedure

The objective of the 1-g level flight sweeps was to provide data that showed the effects of advance ratio for representative flight conditions, including various levels of aircraft weight. A speed sweep at level flight was conducted, wherein the shaft angle and trim targets are varied from one speed to another, such that the vertical force and propulsive force targets match those expected to occur in flight.

Representative trim conditions for the wind tunnel test were determined through a series of pre-test calculations where aircraft weight, M_{tip}, fuselage drag, and aircraft c.g. position were assumed constant. These calculations provided the target lift, propulsive force, and hub moments to be used during testing. For each wind tunnel test condition, the rotor RPM and tunnel speed were set to match the target M_{tip} and μ, and the shaft angle set to match the predicted value. The trim controller then targeted the appropriate lift and hub moments and estimated the shaft angle change necessary to match propulsive force. The lift and propulsive force used as targets included corrections for wind tunnel wall effects. The shaft angle was then manually adjusted until all trim targets were met.

The 1-g level flight sweeps were performed at three lift levels, $C_L/\sigma=0.08$, 0.09, and 0.10, up to an advance ratio of $\mu=0.4$. A subset of the speed sweep runs which have been simulated in the present work corresponding to $C_L/\sigma=0.09$ have been tabulated in

Table 4.1. For each wind tunnel test condition, the rotor RPM, tunnel speed, and shaft angle were set to match the target M_{tip}, μ and α_s. The trim controller then targeted the appropriate rotor thrust (C_T/σ), and zero fixed-system hub moments.

A thrust sweep was performed at each set of conditions until limits were reached. If these limits were associated with rotor stall, collective pitch was manually varied to better define the phenomena. A limited number of sweeps at M_{tip}=0.625 were conducted to attain higher non-dimensional thrusts and advance ratios without reaching load limits. During the collective sweeps, the trim controller only controlled hub moments. A subset of the thrust sweep conditions that have been studied in this work have been tabulated in Table 4.2.

4.1.3 Analytical Trim Methodology

In the numerical predictions, the trim targets are specified in the CSD methodology (DYMORE) to be the measured rotor thrust (C_T/σ), the measured hub moments, and the corrected shaft angle (α_c). The corrected shaft angle (α_c) was derived by applying a Prandtl-Glauert wall correction to the geometric shaft angle (α_s) [23] to account for the effects of the tunnel walls. The hub moments were approximately zero for the thrust sweep and were non-zero for the speed sweep conditions (simulating a rotor in 1-g flight). The autopilot algorithm in DYMORE adjusts the collective and cyclic controls to match the specified trim targets.

4.2 Parametric Speed Sweep

All the speed sweep conditions were carried out at $C_L/\sigma = 0.09$ and a constant tip Mach number M_{tip} of 0.625. In this section, the effects of increasing the advance ratio for the same value of non-dimensional lift will be discussed. The blade root motion, the integrated performance predictions, sectional airloads (normal force and pitching moment) as well as the blade structural loads for the parametric speed sweep run are discussed.

4.2.1 Comparison of Trim Settings

The time history of blade root motion from the converged CFD/CSD analysis was used to extract the collective, longitudinal and lateral cyclic control angles. These values are compared with the measured collective, longitudinal and lateral cyclic angles as shown in Figure 4.3 a-c. As the advance ratio increases, the propulsive power increases thereby resulting in an increase in the collective. With increase in advance ratio, the longitudinal cyclic is increased to counteract the increasing nose-down pitching moment thereby maintaining trim in the longitudinal direction. As shown in Figures 4.3 a-b, the collective and longitudinal cyclic compare well with the measured values for the parametric speed-sweep. However, there is a constant difference of 1-1.5 deg between measured and predicted lateral cyclic angles, as seen in Figure 4.3 c.

4.2.2 Integrated Performance Results

The non-dimensional predicted performance indicators for thrust, propulsive force, power coefficient and lift to equivalent drag obtained from the coupled CFD/CSD analysis are compared against the test data for the parametric speed sweep in Figure 4.4. The solution domain from where the performance indicators were extracted (CFD or CSD) is indicated in the legend. The CFD/CSD methodology employed performs well in predicting the integrated performance indicators as a function of advance ratio. The prediction of thrust is within experimental error limits, which is expected since thrust is one of the trim targets. The small differences between CFD and CSD predictions is due to interpolation effects not accounting for force conservation at the fluid and structure interface. The measured and predicted power coefficients compare well for all advance ratios. The agreement between predicted and measured propulsive force for the parametric speed sweep is good at lower advance ratios, while there is an over-prediction at higher advance ratios. Since the propulsive force is over-predicted at higher advance ratios, the L/De is over-predicted as well. Note that the use of fully turbulent flow, an assumption made in the current CFD methodology, tends to over-predict the viscous drag and may affect the stall behavior.

4.2.3 Lowest Advance Ratio run (5215)

The lowest advance ratio, $\mu = 0.15$ presents a challenge to the Hybrid CFD methodology since there is occurrence of Blade Vortex Interaction (BVI) phenomena at this advance ratio. The effects of the near-wake are critical for capturing the BVI events accurately. Using the current Hybrid approach, the effects of the near wake elements are very diffused. Therefore, it is important to study how well the Hybrid methodology is able to predict airloads at this advance ratio. Since the advance ratio is low, the wake is not convected away from the blades quickly and remains in the plane of rotor rotation. The older vortices released from the blades convect above the rotor plane and interact with the flow over the subsequent blades to give rise to impulsive loading.

The impulsive loading due to BVI is sensitive to wake modeling effects as the wake representation determines the induced inflow over the rotor disk. Therefore, the effect of using a single tip vortex representation vs. multiple trailing and shed vortices representation has been studied for this advance ratio. The sectional normal loads and pitching moments for this test condition are shown in Figure 4.5. Results indicate that the inboard loading behavior in between 22.5% and 40% radial stations, is better captured using the multiple trailer wake in conjunction with the shed wake model. The multiple trailer wake model appears to better predict the strength and geometry of the inboard vortices. This in turn improves the induced velocity prediction over the rotor disk. Therefore, the trends in sectional normal force are well matched using the multiple trailer and shed wake model. In contrast, the single tip vortex model has been observed to over-predict the peak-to-peak magnitude of sectional airloads at all radial locations. It may be inferred that the vortices trailed from the in-board radial locations for this flight condition have a considerable effect on the blade loading. Quantitative assessment of the accuracy of airload predictions obtained using multiple trailer model vs. single tip model was performed using the approach documented in Appendix A. A linear regression of the predicted data provides the quantitative metrics of the linear curve fit – slope (m) and coefficient of determination (r^2). As correlation between the measured and the predicted data improves, the values of m and r^2 reach unity. The quantitative metrics for sectional normal loads at each radial location have been tabulated in Table 4.3, from which it is evident that the multiple trailer in conjunction with the shed wake model predicts better.

The BVI phenomenon is sensitive to miss distance, vortex strength as well as crossing of the vortices. The high frequency impulsive loading characteristic of BVI events is evident in the sectional pitching moment data near $\psi = 75°$ and $\psi = 270°$ azimuthal locations. The impulsive behavior starts at r/R =0.775 and extends through the tip region. Although the agreement in the sectional normal loads is adequate, the pitching moment data misses peak-to-peak predictions. The vortex trailer trajectories from r/R = 0.865 to the tip region have been plotted in Figure 4.6 colored according to the vortex strength. It can be seen that the strongest vortices are found near ψ = 270°. In Figure 4.7, the vortex crossings above and below the rotor tip path plane are shown. The vortices are colored according to their vicinity from the rotor tip path plane. The vortices trailed by the previous blade (shown at ψ = 0° in Figure 4.7) intersect the blade tip region of the successive blade at ψ = 270°. Similar vortex crossings are seen at ψ = 90°. The CFD predictions capture the BVI events reasonably well, although the peak-to-peak of the impulsive loading has not been well-captured by the hybrid CFD methodology.

4.2.4 Sectional Airloads

The effects of increasing the advance ratio for a constant tip Mach number were studied for the conditions enlisted in Table 4.1. For the low advance ratio cases runs 5215 and 5220, the CFD solution required a larger number of rotor revolutions within the coupling process for achieving convergence of the rotor hub loads. The contribution of induced inflow towards the blade sectional angle of attack is higher at lower advance ratios. Therefore, it takes a larger number of rotor revolutions for the wake induced loads to attain steady state solution. In rotorcraft experimental testing, e.g. Lorber [8], errors in the blade pressures can have large effects on integrated section pitching moments. Bad trailing edge pressure taps in the dataset considerably skew the pitching moment mean values. For this reason, all plots of pitching moment have the mean removed.

A qualitative representation of the predicted sectional normal loads and pitching moments for 3 advance ratios μ = 0.15, 0.3 and 0.37 is shown in Figure 4.8. The pitching moments data in Figure 4.8 a, show impulsive loading in the first and fourth quadrant due to the occurrence of BVI phenomena. Sectional normal loads in Figure 4.8 b and c corresponding to μ = 0.3 and 0.37, depict negative loading on the advancing side tip region, which is produced to accommodate roll moment balance in high speed flight. The negative normal loads at the inboard stations on the retreating side are also seen due to reverse flow. Similarly, the pitching moment data in Figure 4.8 b and c show negative moments on the advancing side, characteristic of high speed flight.

A detailed comparison of sectional normal loads and pitching moments near the tip region r/R = 0.92, at the same advance ratios $\mu = 0.15$, 0.3 and 0.37 is shown in Figure 4.9. On the advancing blade, transonic flow sets in at the tip region, causing negative lift at the end of the first quadrant. With increase in advance ratio, the negative loading in the blade sectional normal loads becomes more pronounced as compressibility effects intensify. Increased nose down pitching moments are observed as well. The CFD/CSD predictions show an under-prediction in peak-to-peak magnitude of pitching moments.

4.2.5 Structural Loads

The blade structural loads namely the flapwise bending moment, torsional moment and edgewise bending moment at 40%R have been compared in Figure 4.10, Figure 4.11, and Figure 4.12 respectively for advance ratios of 0.15, 0.3, and 0.37. Steady values have been removed from the measured and predicted data. The waveform of the flapwise bending moments follows the waveform of the normal loads data. At $\mu = 0.15$, there are two troughs observed in the flapwise bending moment predictions, the first corresponding to the impulsive down-up loading in the normal loads data, the second trough occurring in the second quadrant as a result of negative sectional angles of attack. With increase in advance ratio, compressibility effects become more prominent on the advancing blade, giving rise to the corresponding waveform in the flapwise bending moment predictions. The flapwise bending moments are slightly under-predicted by

CFD/CSD predictions. A consistent phase difference is observed between the measurement and the predictions.

The oscillatory torsional moment predictions show strong 4P variation at μ = 0.15, which has not been captured accurately in CFD/CSD predictions. As advance ratio increases, the waveform for torsional moments is well-captured on the advancing side, while the sharp drop in torsional moment on the retreating side near ψ= 250° is not well-predicted. The peak-to-peak magnitude is well-predicted. The prediction quality of oscillatory torsional moments is directly related to that of sectional pitching moments.

The test data for oscillatory chordwise bending moment at 40%R shows high frequency content at μ = 0.15. The peak-to-peak of chordwise bending moment is significantly under-predicted and the phase is not well-captured. The correlation quality does not improve with increase in advance ratio. The comparison of measured vs. predicted time histories of push-rod loads has been shown in Figure 4.13 for the speed-sweep conditions. The advancing side wave-form is captured well while the dual-peak behavior on the retreating side is not well-captured.

4.3 Parametric Thrust Sweep

Results have been obtained for parametric thrust sweep conditions as tabulated in Table 4.2. These conditions range from an un-stalled condition to deeply stalled conditions. The parametric thrust sweep was carried out at a fixed μ = 0.3 and a constant tip Mach number M_{tip} of 0.625.

4.3.1 Comparison of trim settings

Figure 4.14 a-c show comparison of measured and predicted collective, longitudinal and lateral cyclic angles. For the same forward speed, increase in blade loading results in increase in the rotor collective. The measured and predicted collective angles compare very well. There is good agreement between measured and predicted longitudinal cyclic angles for the thrust sweep. The lateral cyclic angle is over-predicted by the CFD/CSD analysis by a marginal amount, as seen in Figure 4.14 c.

4.3.2 Integrated Performance Results

Figure 4.15 shows performance indicators for the measured and simulated thrust sweep conditions. The agreement between measured and predicted thrust coefficient values is excellent, since the rotor is trimmed to the specified thrust target. The power coefficient increases steeply with increase in blade loading value. There is a slight over-prediction in the power predictions. At low blade-loading values, the propulsive force coefficients are over-predicted for the parametric thrust-sweep. However, the lift to equivalent drag prediction matches the test-data. The equivalent drag is obtained by subtracting propulsive power from the total power. Since there is an over-prediction in both, the values of equivalent drag match well with the test data giving rise to a decent agreement in the L/D_e ratio.

4.3.3 Sectional Airloads

The contour plots of predicted sectional normal loads and pitching moments for 3 thrust conditions $C_T/\sigma = 0.02, 0.06$ and 0.12 are shown in Figure 4.16. The distribution of sectional normal force and pitching moments for the thrust sweep is significantly different from that of the speed sweep (Figure 4.8). Since the rotor is operating at $\mu = 0.3$, compressibility effects on the advancing blade tip are observed for all the blade loading values in the parametric thrust sweep. At $C_T/\sigma = 0.02$, negative loading is observed on the advancing side in both the normal sectional loads and pitching moments at the blade tip.

As the blade loading value increases, the reverse flow region on the retreating side becomes pronounced as seen in normal loads data in Figure 4.16 b and c. At $C_T/\sigma = 0.12$, the pitching moment prediction shows two distinct stall regions on the retreating side. These regions are spread over a narrow range of azimuth and are characteristic of dynamic stall phenomena. The normal sectional loads at this blade loading value show four distinct areas of high lift.

Detailed sectional normal loads and pitching moment predictions at 92% radial station for the same 3 representative thrust sweep conditions are shown in Figure 4.17. For the thrust sweep runs, the shaft angle of attack α is very close to zero. The measured as well as predicted data show negative normal loads at 92% spanwise station on the advancing side. In Figure 4.17, at $C_T/\sigma = 0.06$, BVI-induced pulses in the first quadrant are observed, similar to speed-sweep condition at $\mu = 0.15$ (Figure 4.9). The current methodology is able to capture the impulsive pitching moment variation in the first quadrant at $C_T/\sigma = 0.06$. There is a phase difference observed in the sectional normal loads on the advancing blade at this radial station. At higher thrust values, dynamic stall sets in and is clearly observed in the pitching moment data at $\psi = 290°$ and $\psi = 340°$. The first dynamic stall cycle has been predicted accurately in magnitude and phase, while there is under-prediction in magnitude of the second dynamic stall at $C_T/\sigma = 0.12$. The stall cycles were observed only at blade loading values equal to and greater than 0.12.

4.3.4 Structural Loads

The structural loads for the thrust sweep runs are shown in Figure 4.18, Figure 4.19 and Figure 4.20 respectively. The peak-to-peak predictions of flapwise bending moment for the 3 representative thrust sweep runs compare well with the test data. At

C_T/σ = 0.02 and 0.06, the flapwise bending moment at 40%R shows high frequency oscillations near the end of the first quadrant and the beginning of the second. At C_T/σ = 0.12, the torsional moments prediction captures the waveform of the test data associated with dual dynamic stall on the retreating side. There is significant under-prediction of chordwise bending moment at all values of C_T/σ. The CFD/CSD predictions show significant 5P oscillations manifesting as a result of dynamic stall events. The blade 2nd chord frequency is 4.69P and first torsion frequency is 4.53P, therefore, the structural response due to 5P aerodynamic forcing function as a result of dynamic stall is magnified [26].

Figure 4.21 shows oscillatory push-rod loads for all the test conditions studied in the thrust sweep. The waveform of the push-rod loads is similar to the waveform of the torsion moments at r/R = 0.4. The peak-to-peak loads are well-predicted at lower blade-loading values. As the blade-loading increases, the magnitude of compressive push-rod loads on the retreating blade is magnified in the CFD/CSD predictions, due to stall effects.

4.4 Summary of Results

Two parametric runs namely speed sweep at constant lift and thrust sweep at constant advance ratio were investigated for full-scale wind tunnel UH-60A rotor using a Hybrid CFD methodology and a multi-body dynamics CSD approach using loosely coupled CFD/CSD methodology. All the fundamental flow phenomena have been modeled by the current CFD/CSD methodology. The following are the key conclusions from the study.

Speed Sweep

1. The prediction of airloads at low advance ratio was found to be sensitive to the wake modeling effects. The multiple span wake model was found to be better in predicting impulsive loading arising due to blade-vortex interaction on the advancing and retreating sides. For accurately capturing the impulsive loading due to blade and vortex interactions using hybrid CFD methodology, embedded grids to ensure less dissipation of the near-wake may be used.
2. Best agreement in structural load prediction was obtained for flapwise bending moment data, followed by torsional moments. Torsional moments for $\mu = 0.15$ show a strong 4P variation. While the peak-to-peak values of pushrod loads are captured, the retreating side waveform was not well-predicted. The retreating-side behavior needs to be further investigated.
3. The integrated performance results showed best agreement between measured and predicted thrust and power coefficients. The propulsive force agreement was found to be better at lower advance ratios while it was over-predicted at higher advance ratios. The equivalent lift to drag ratio was over-predicted at high advance ratios.
4. The trim control settings – collective, longitudinal cyclic are well predicted for the speed sweep, while lateral cyclic was consistently over-predicted by 1° to 1.5° at the most, for the parametric speed sweep.

Thrust Sweep

5. The test condition with $C_T/\sigma = 0.06$ is characterized by BVI impulses seen on the advancing blade. At $C_T/\sigma = 0.12$, dynamic stall phenomena is seen on the retreating side. There is a slight over-prediction in the magnitude of normal loads.

6. The peak-to-peak and waveform of flapwise bending moment and torsional moments have been predicted moderately well. The 5P variation in the predictions for chordwise bending moment is amplified due to the dynamic stall events. The chordwise bending moments are under-predicted and phase is not well-matched.
7. The integrated results showed reasonable agreement in thrust coefficients, while an over-prediction in the power and propulsive force coefficients was observed. At lower blade-loading values, the percentage error in the prediction of propulsive force was found to be higher.
8. The trim control settings – collective, longitudinal cyclic as well as the lateral cyclic angles are captured consistently for the thrust sweep.

Run*	**Data Point**	**Advance Ratio (μ)**	**Corrected shaft angle of attack (deg)**
52	15	0.15	0.89
52	20	0.20	-0.31
52	25	0.24	-1.50
52	31	0.30	-3.49
52	35	0.35	-5.58
52	40	0.37	-6.74

Table 4.1 Wind-tunnel speed-sweep conditions at $C_L/\sigma = 0.09$.

Run*	**Data Point**	**C_T/σ**	**Corrected shaft angle of attack (deg)**
45	28	0.020	0.15
45	29	0.040	0.31
45	30	0.060	0.47
45	33	0.090	0.70
45	36	0.120	0.94
45	40	0.123	0.97

Table 4.2 Wind-tunnel test database comprising of thrust-sweep conditions at μ= 0.3

Figure 4.1 UH-60A rotor system installed on the Large Rotor Test Apparatus in the NFAC 40-by 80-foot wind tunnel [23]

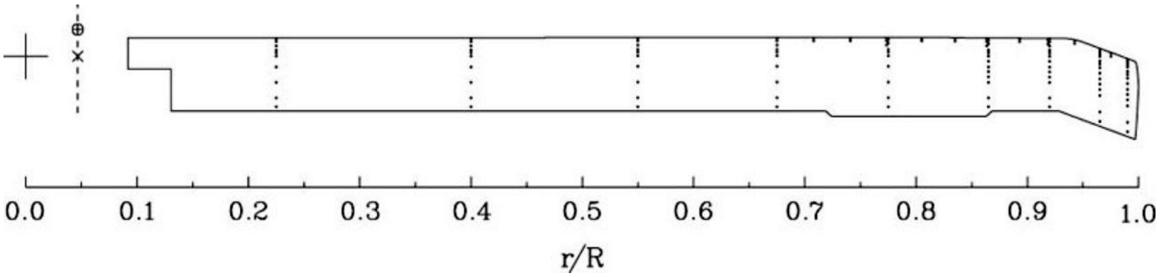

Figure 4.2 Location of pressure transducers on the instrumented blade [23]

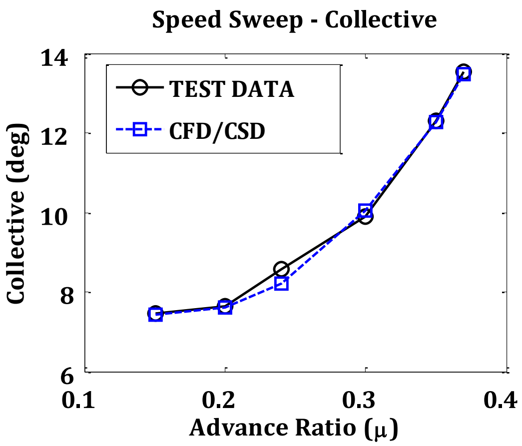

a) Collective

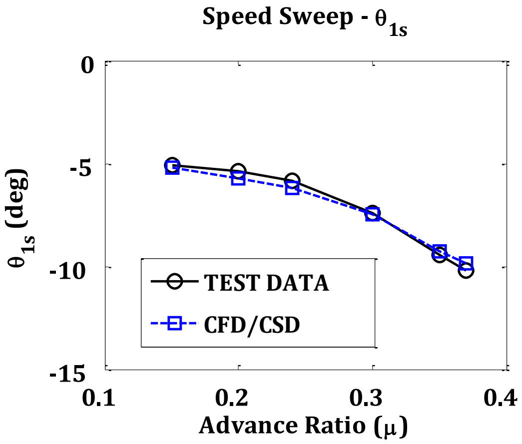

b) Longitudinal cyclic

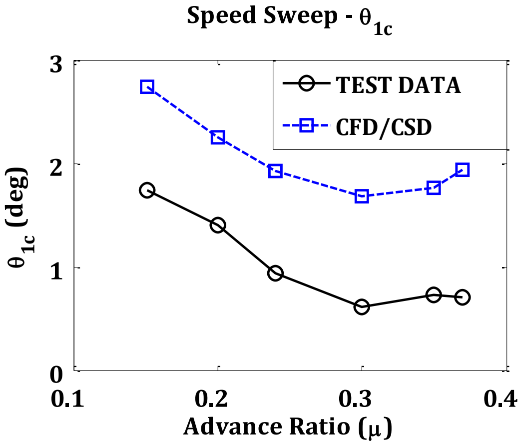

c) Lateral cyclic

Figure 4.3 Calculated and measured blade pitch angle for speed sweep.

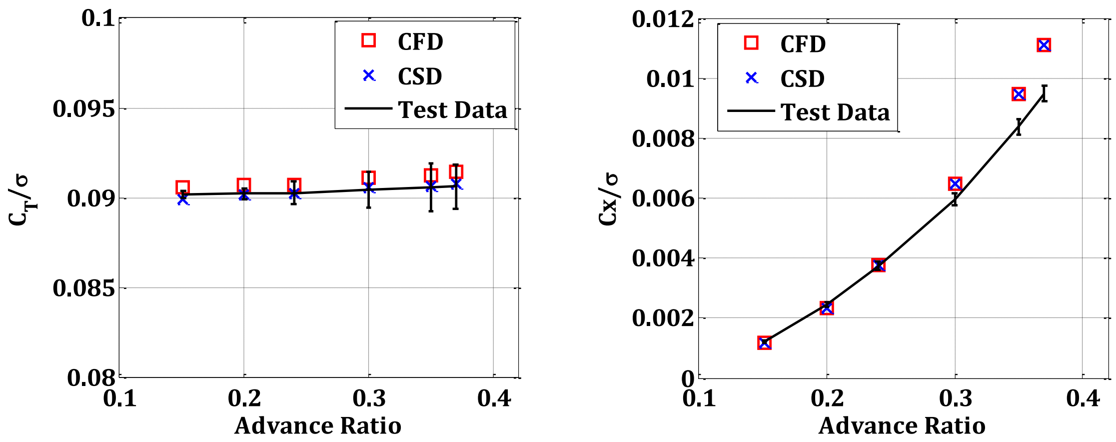

a) Integrated thrust coefficient

b) Integrated propulsive force coefficient

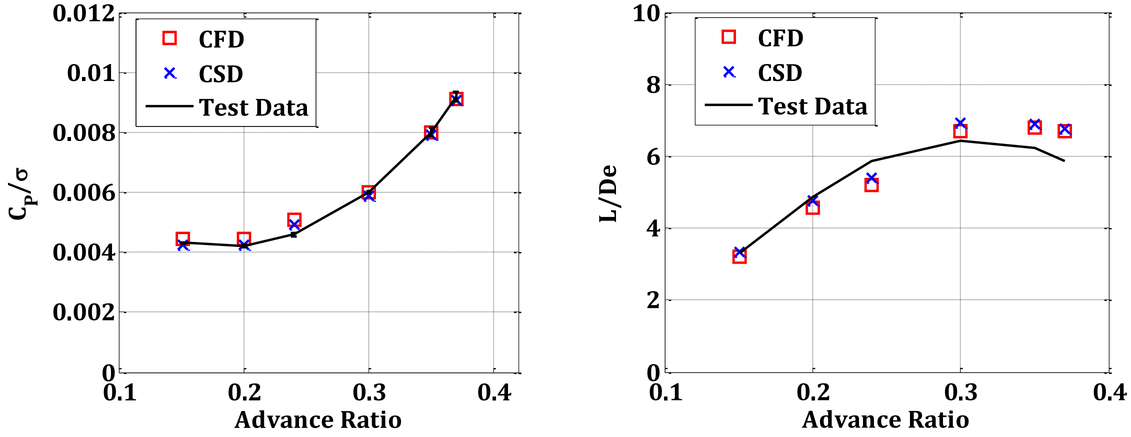

c) Integrated power coefficient

d) Lift to equivalent drag ratio

Figure 4.4 Performance indicators as a function of advance ratio.

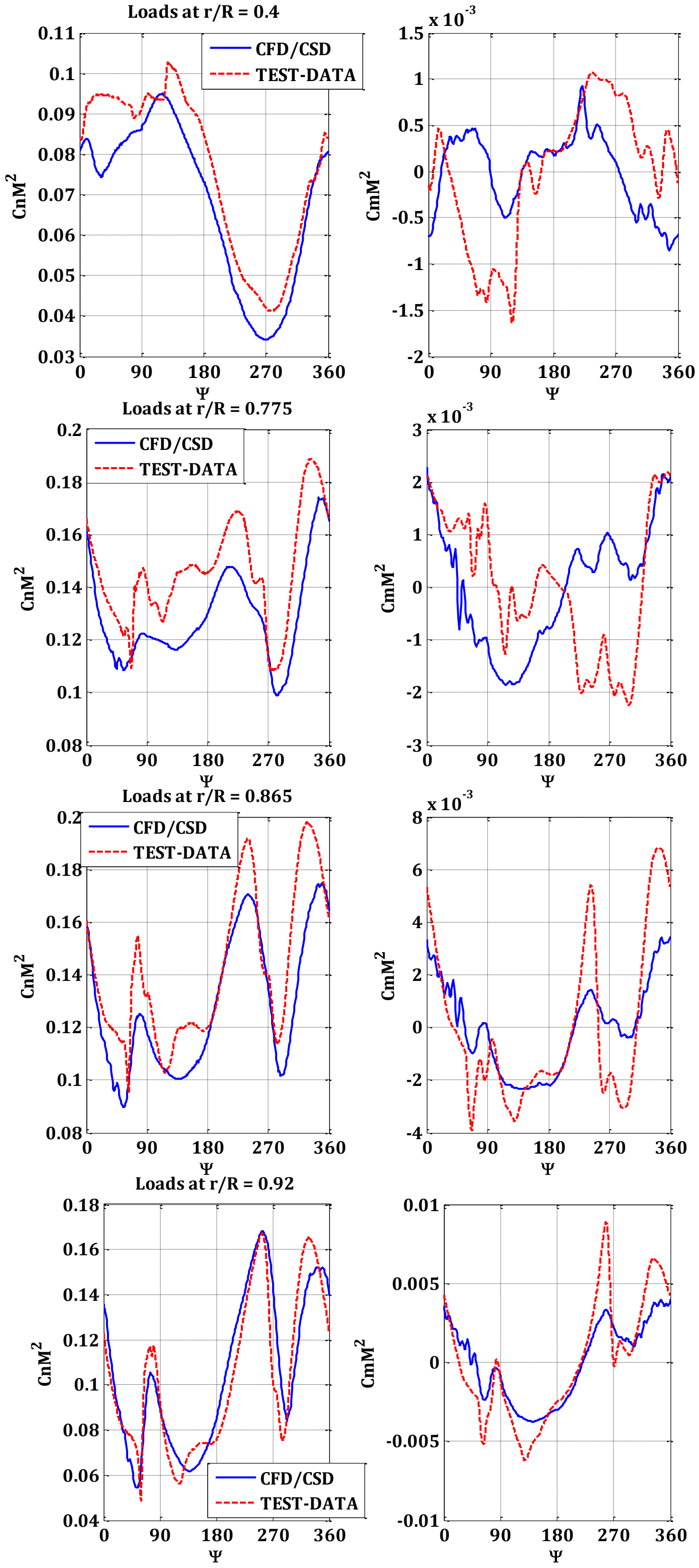

Figure 4.5 Sectional normal loads and pitching moments (means removed) for Run 5215 with μ = 0.15.

	Single trailer model		Multiple trailer + shed wake	
Radial location (r/R)	**Slope (m)**	**Coefficient of determination (r^2)**	**Slope (m)**	**Coefficient of determination (r^2)**
0.225	1.4803	0.7573	1.2454	0.9583
0.400	1.1974	0.8448	0.9594	0.9475
0.675	0.3333	0.1335	0.7538	0.7494
0.775	0.3807	0.1335	0.8092	0.8043
0.865	0.6684	0.2879	0.8213	0.8104
0.920	0.8992	0.4203	0.9249	0.8384
0.965	0.9249	0.5436	0.8564	0.8529
0.990	1.0342	0.5661	0.9523	0.8164

Table 4.3 A comparison of the prediction accuracy of sectional normal loads using single concentrated tip vortex vs. spanwise distribution of vorticity in conjunction with shed wake, for a low speed flight condition (Run 5215) at μ = 0.15.

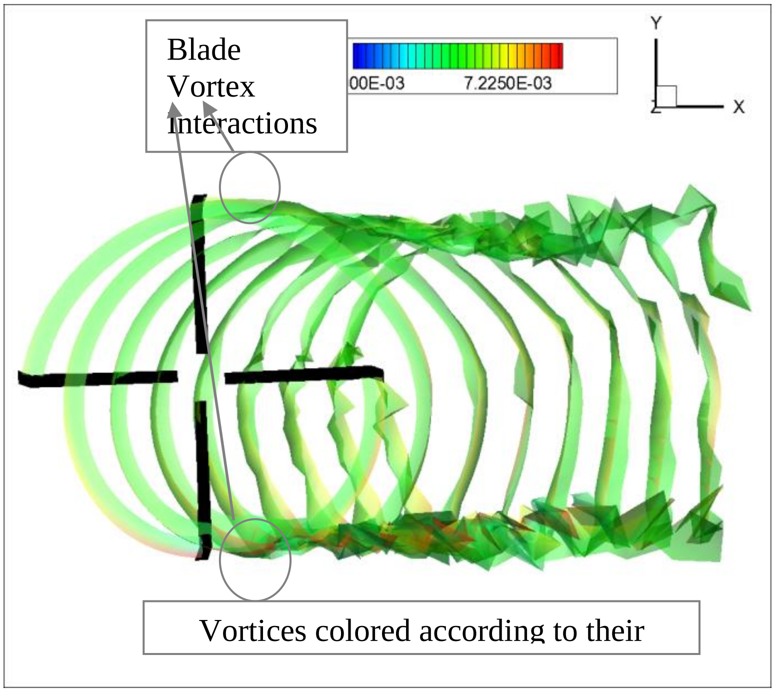

a) Tip vortices colored according to strength

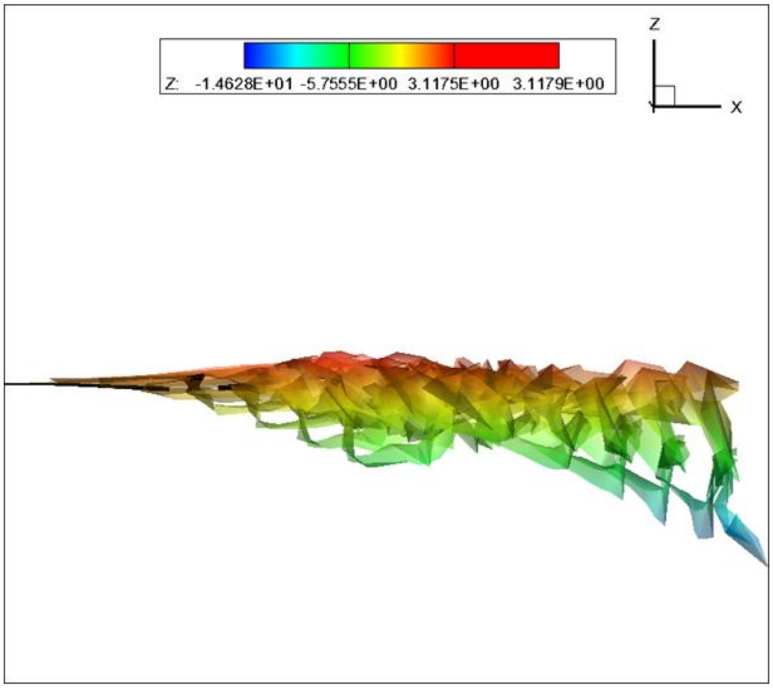

b) Vortices colored according to vicinity from tip-path-plane

Figure 4.6 Wake geometry obtained using Hybrid CFD methodology for μ = 0.15 condition. Only the vorticity near the tip region has been visualized for clarity.

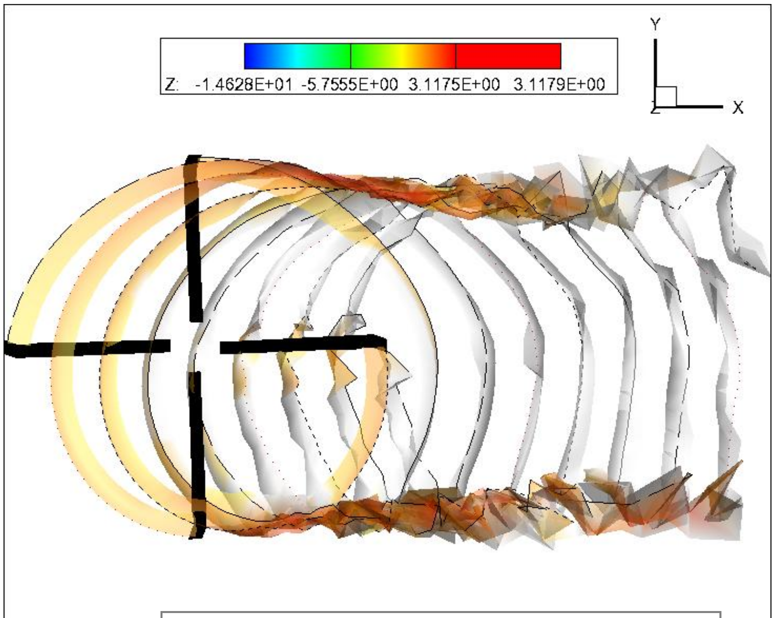

Vortices above the rotor TPP

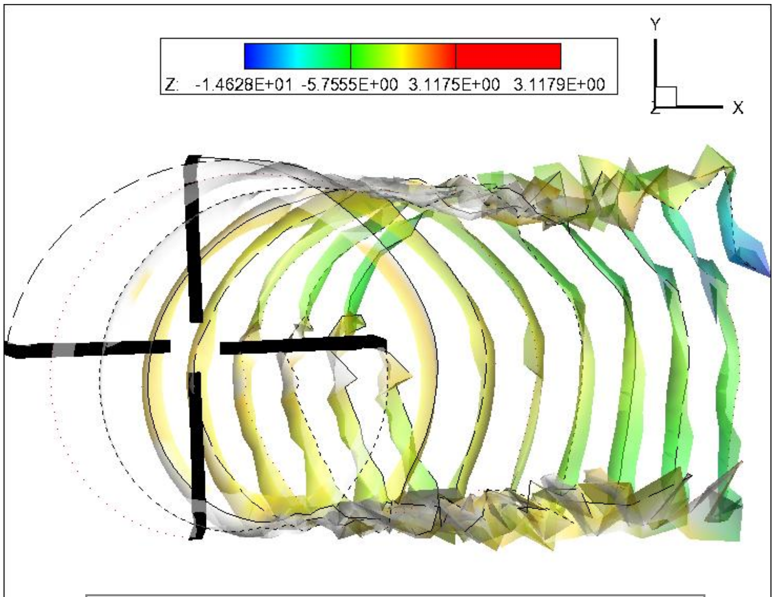

Vortices below the rotor TPP

Figure 4.7 Vortices above and below the rotor tip path plane at μ = 0.15 condition. Only the vorticity near the tip region has been visualized for clarity.

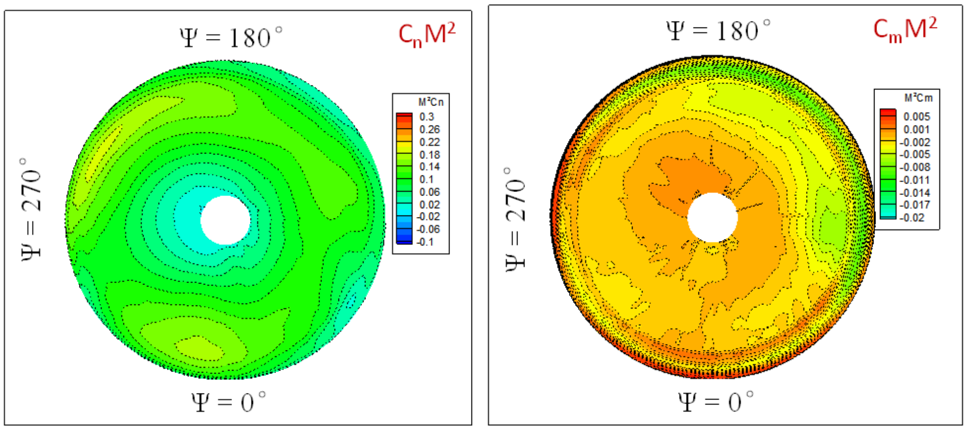

a) $\mu = 0.15$, $C_T/\sigma = 0.09$, **Test Run 5215**

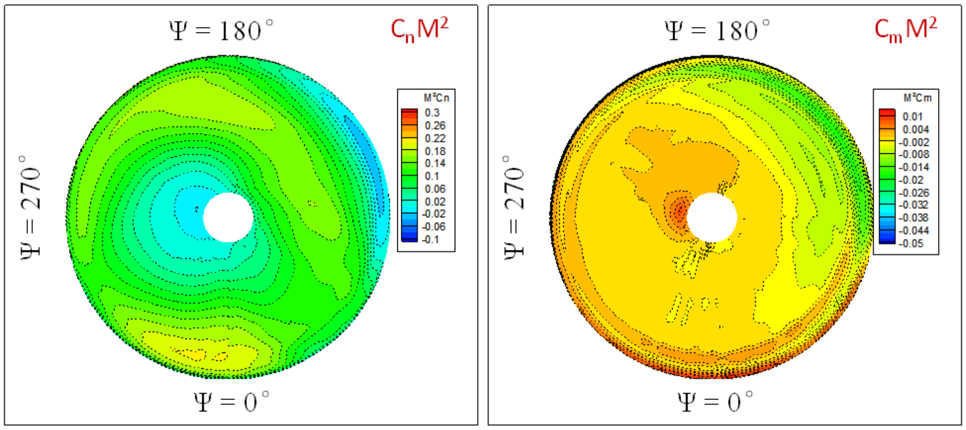

b) $\mu = 0.3$, $C_T/\sigma = 0.09$, **Test Run 5231**

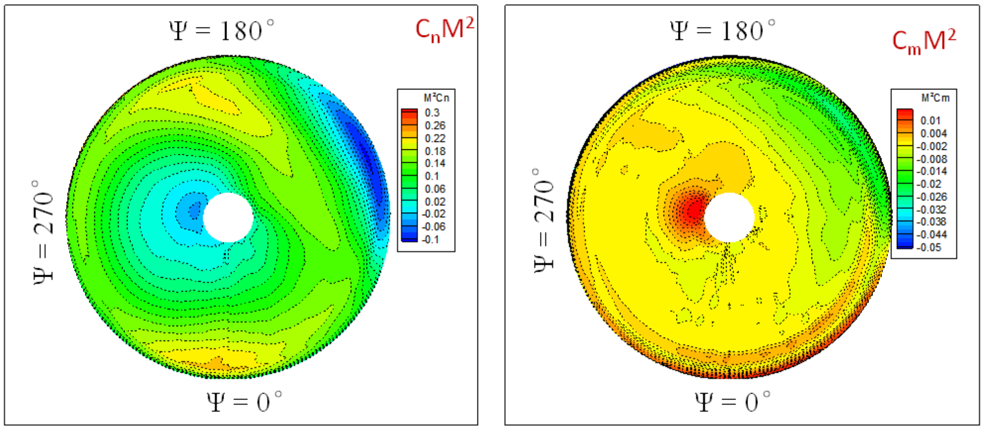

c) $\mu = 0.37$, $C_T/\sigma = 0.09$, **Test Run 5240**

Figure 4.8 Predicted sectional normal loads and pitching moments for selected speed sweep conditions.

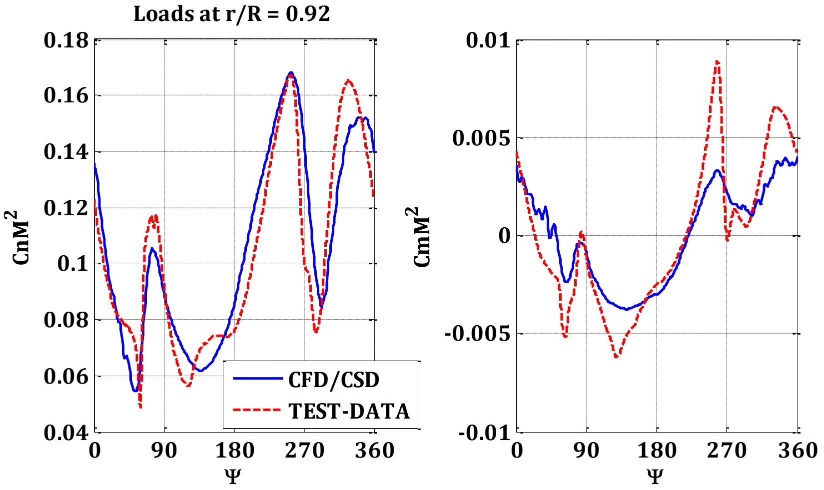

a) μ = 0.15, C_T/σ = 0.09, **Test Run 5215**

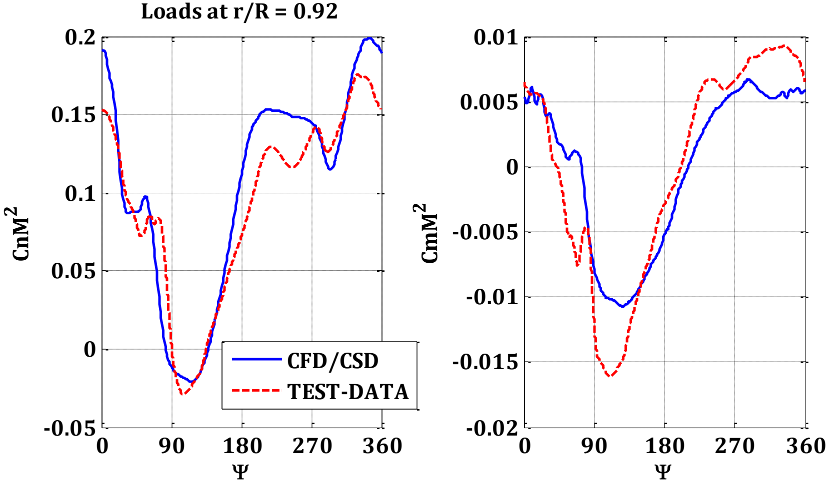

b) μ = 0.3, C_T/σ = 0.09, **Test Run 5231**

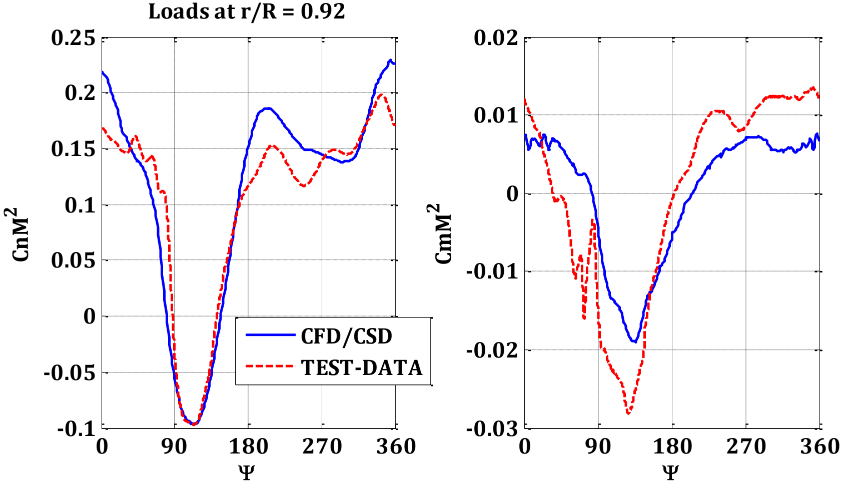

c) μ = 0.37, C_T/σ = 0.09, **Test Run 5240**

Figure 4.9 Comparison of measured and predicted sectional normal loads and pitching moments (means removed) at r/R = 92%, for selected speed sweep conditions.

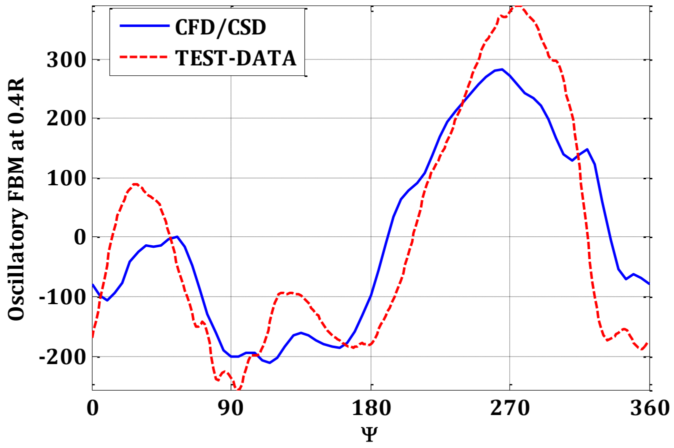

1. μ = 0.15, C_T/σ = 0.09, **Test Run 5215**

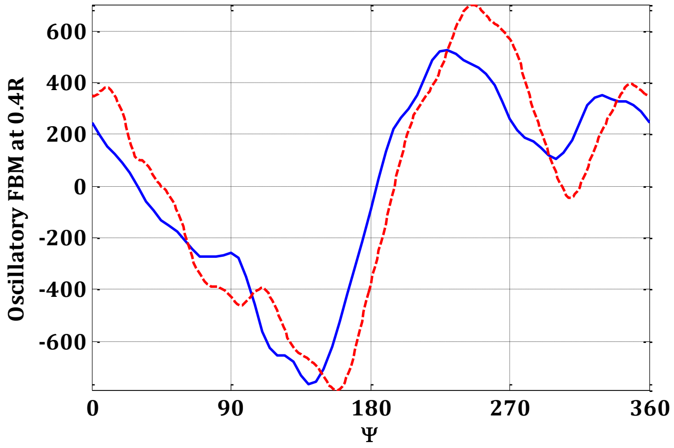

2. μ = 0.3, C_T/σ = 0.09, **Test Run 5231**

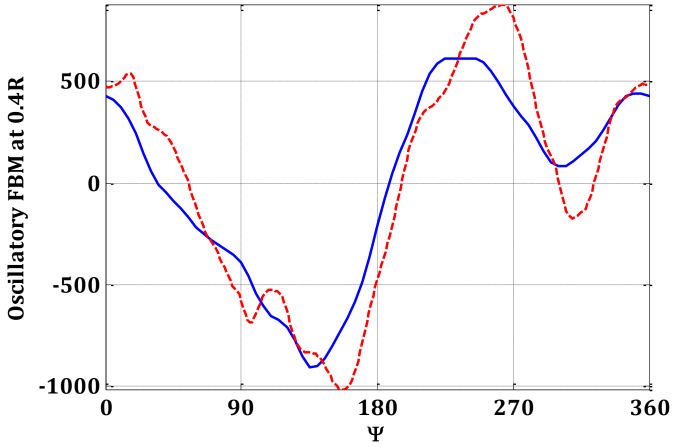

3. μ = 0.37, C_T/σ = 0.09, **Test Run 5240**

Figure 4.10 Comparison of Flapwise Bending Moment at r/R = 0.4 for speed sweep conditions.

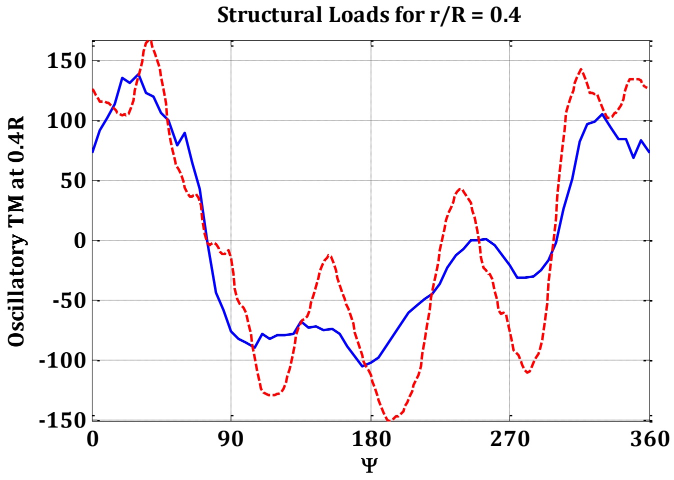

a. μ = 0.15, C_T/σ = 0.09, **Test Run 5215**

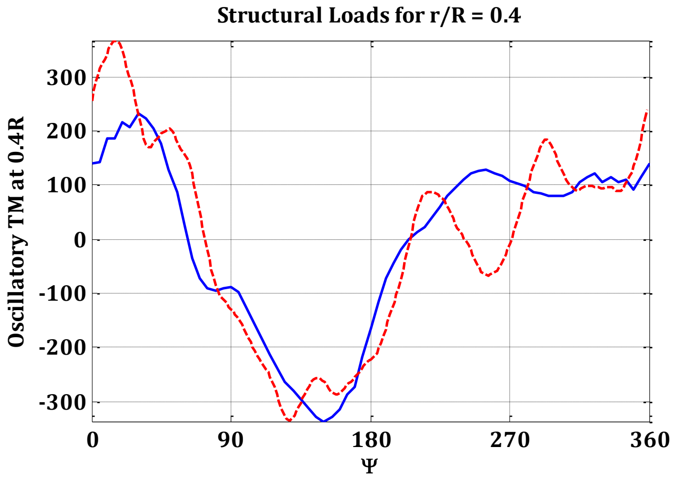

b. μ = 0.3, C_T/σ = 0.09, **Test Run 5231**

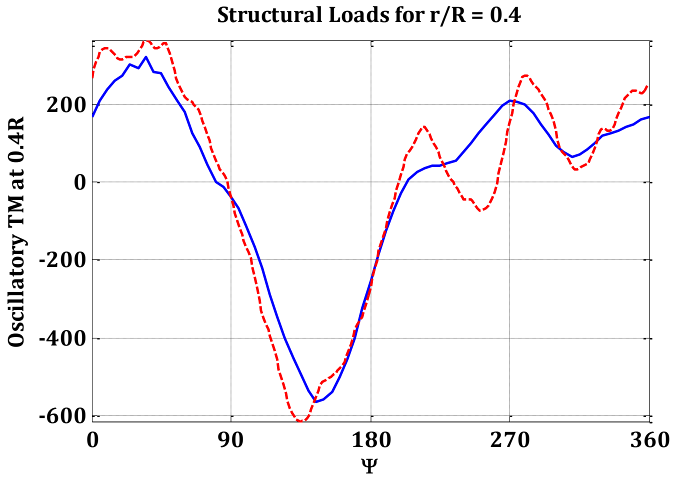

c. μ = 0.37, C_T/σ = 0.09, **Test Run 5240**

Figure 4.11 Comparison of Torsional Moment at r/R = 0.4 for speed sweep conditions.

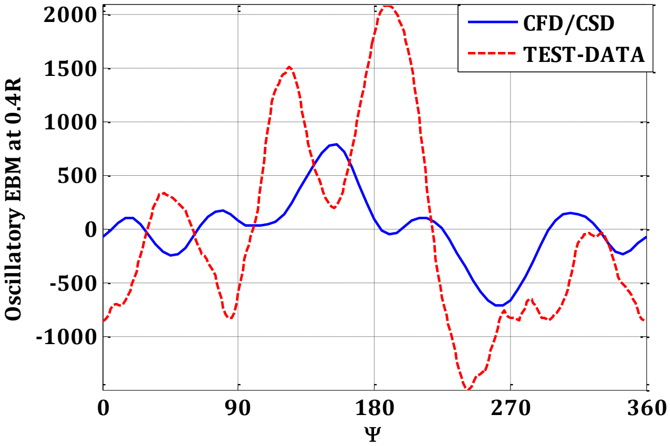

a. $\mu = 0.15$, $C_T/\sigma = 0.09$, **Test Run 5215**

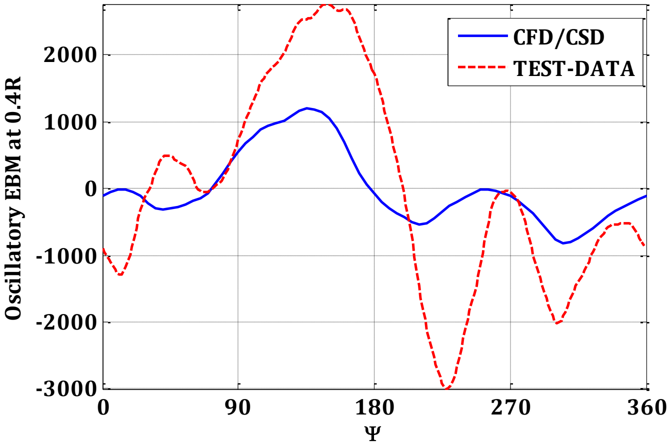

b. $\mu = 0.3$, $C_T/\sigma = 0.09$, **Test Run 5231**

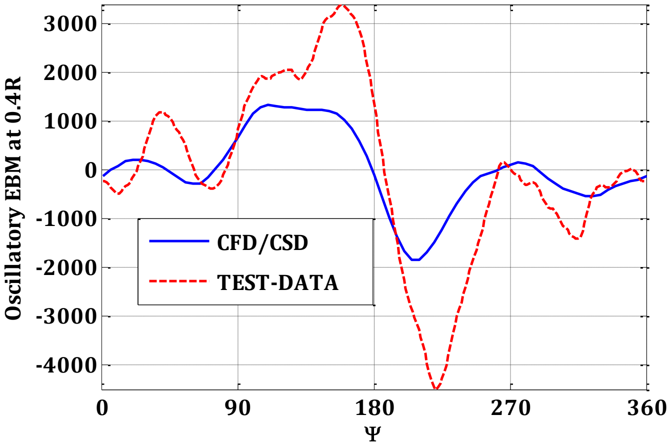

c. $\mu = 0.37$, $C_T/\sigma = 0.09$, **Test Run 5240**

Figure 4.12 Comparison of Edgewise Bending Moment at r/R = 0.4 for speed sweep conditions.

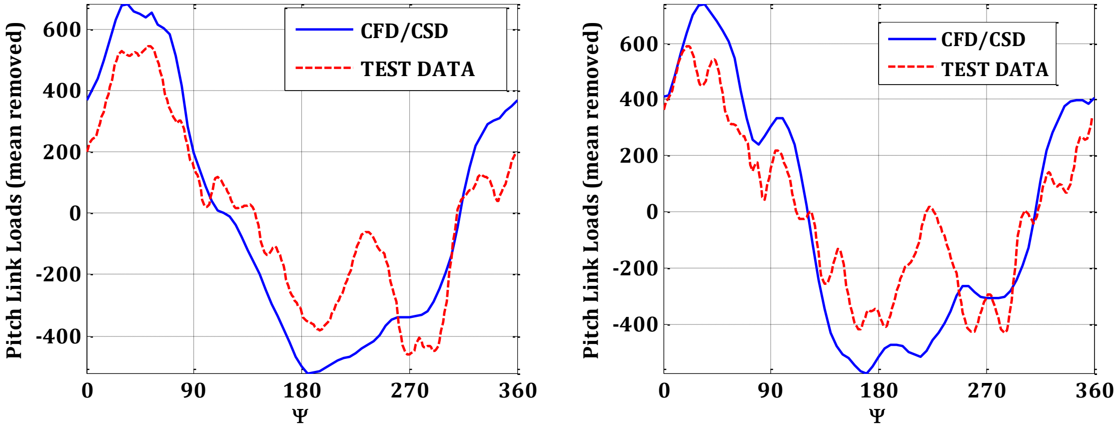

a. μ = 0.15, C_T/σ = 0.09, **Run 5215**

b. μ = 0.2, C_T/σ = 0.09, **Run 5220**

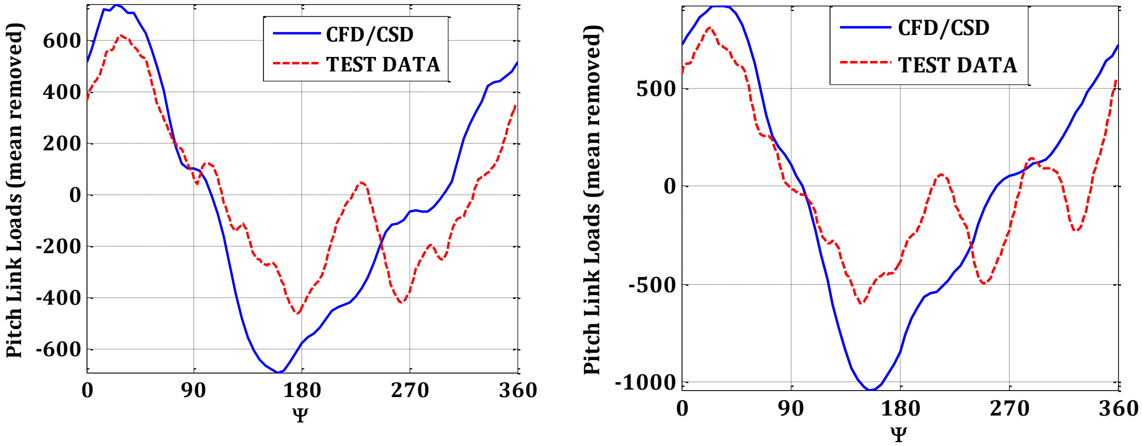

c. μ = 0.24, C_T/σ = 0.09, **Run 5225**

d. μ = 0.30, C_T/σ = 0.09, **Run 5231**

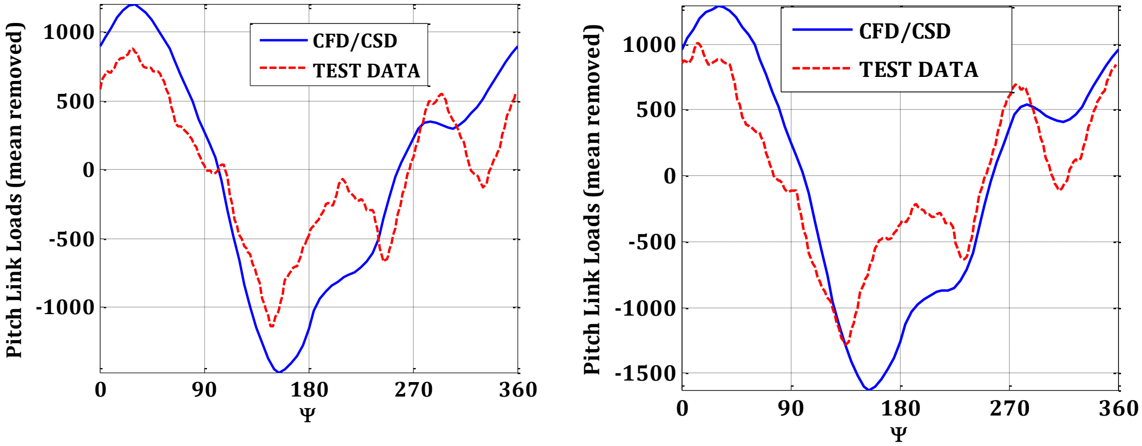

e. μ = 0.35, C_T/σ = 0.09, **Run 5235**

f. μ = 0.37, C_T/σ = 0.09, **Run5240**

Figure 4.13 Comparison of measured and predicted blade oscillatory pitch link loads for speed sweep conditions.

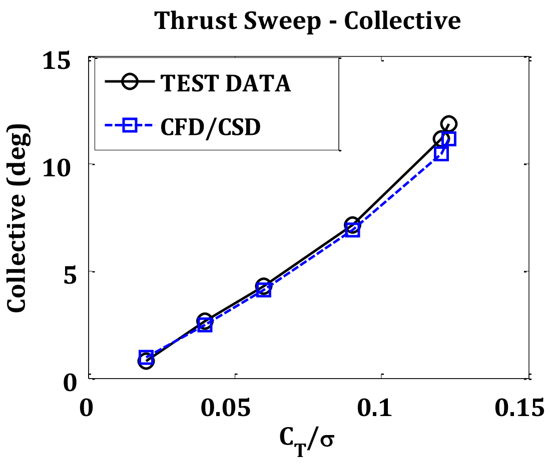

a. Collective

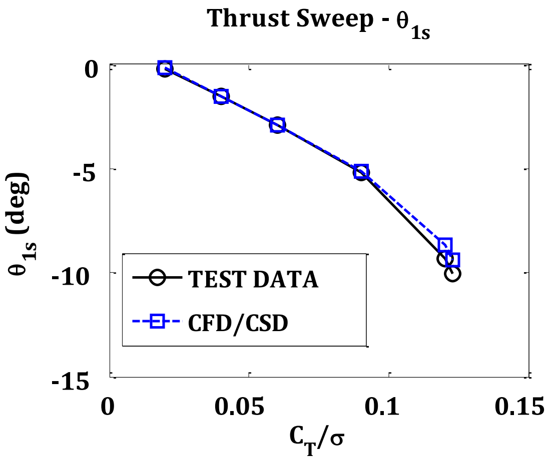

b. Longitudinal cyclic

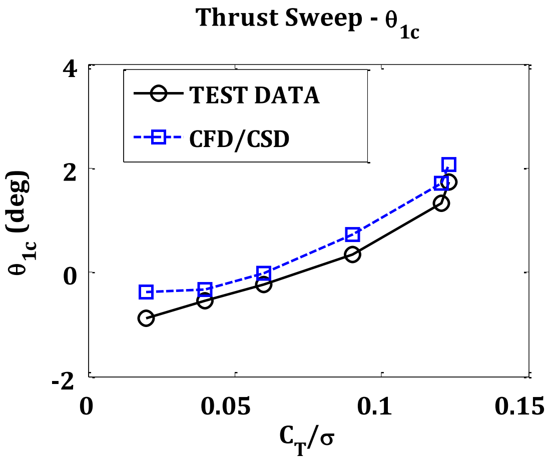

c. Lateral cyclic

Figure 4.14 Calculated and measured blade pitch angle for thrust sweep.

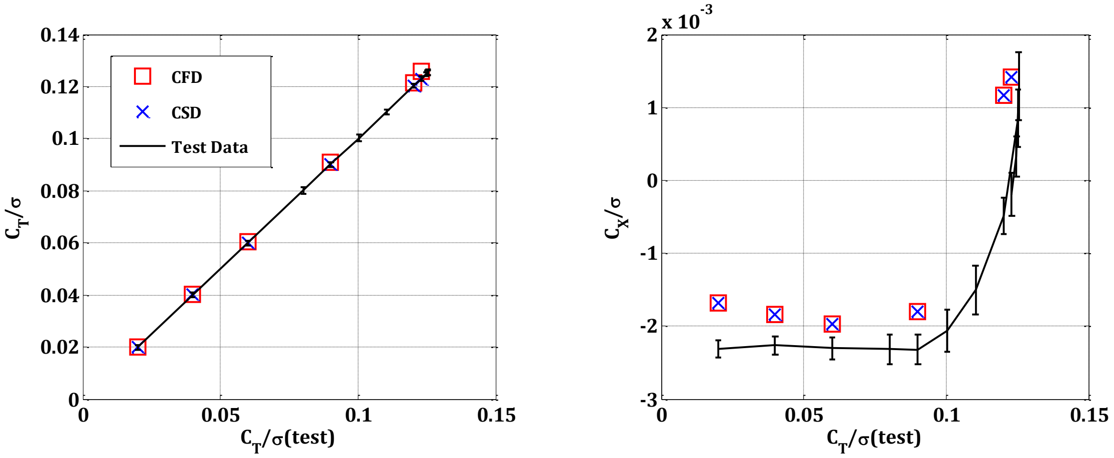

a. Integrated thrust coefficient

b. Integrated propulsive force coefficient

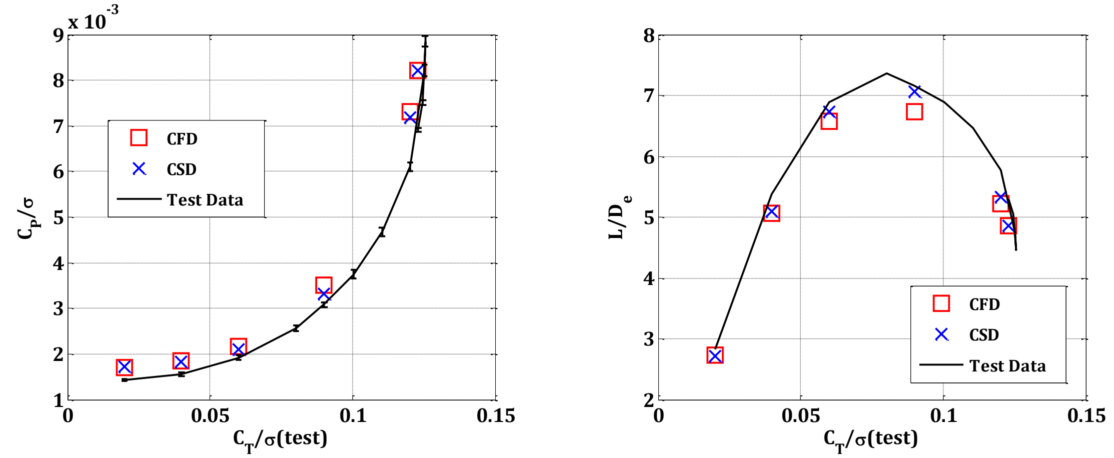

c. Integrated power coefficient

d. Lift to equivalent drag ratio

Figure 4.15 Performance indicators as a function of blade loading value.

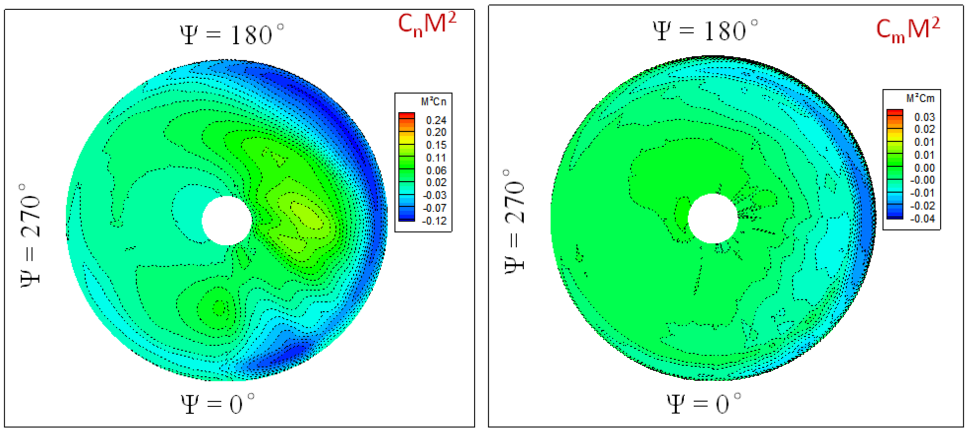

a) $C_T/\sigma = 0.02$, $\mu = 0.3$, **Test Run 4528**

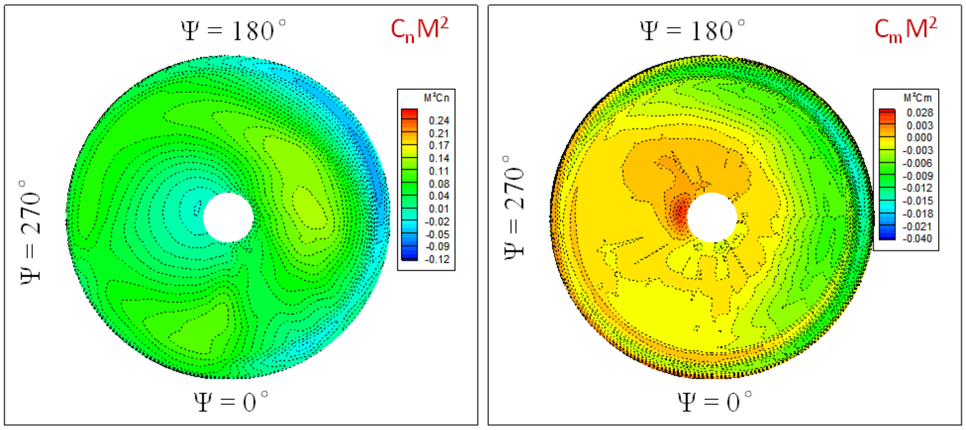

b) $C_T/\sigma = 0.06$, $\mu = 0.3$ **Test Run 4530**

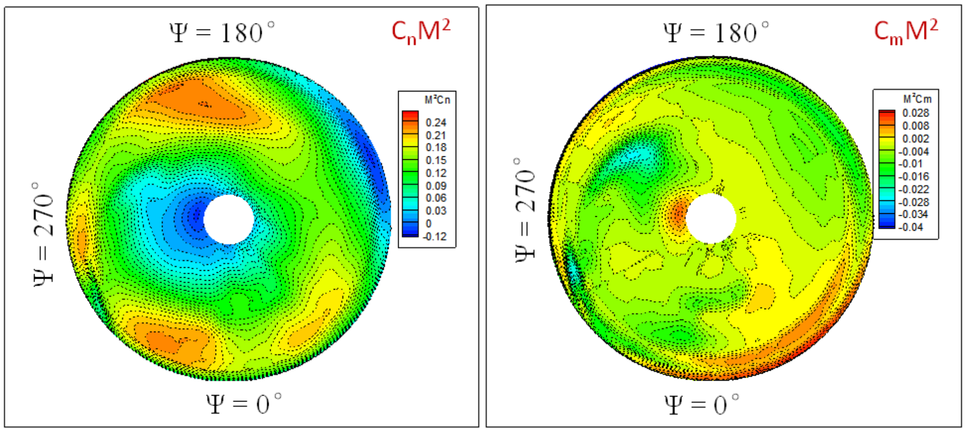

c) $C_T/\sigma = 0.12$, $\mu = 0.3$ **Test Run 4540**

Figure 4.16 Predicted sectional normal loads and pitching moments for selected thrust sweep conditions.

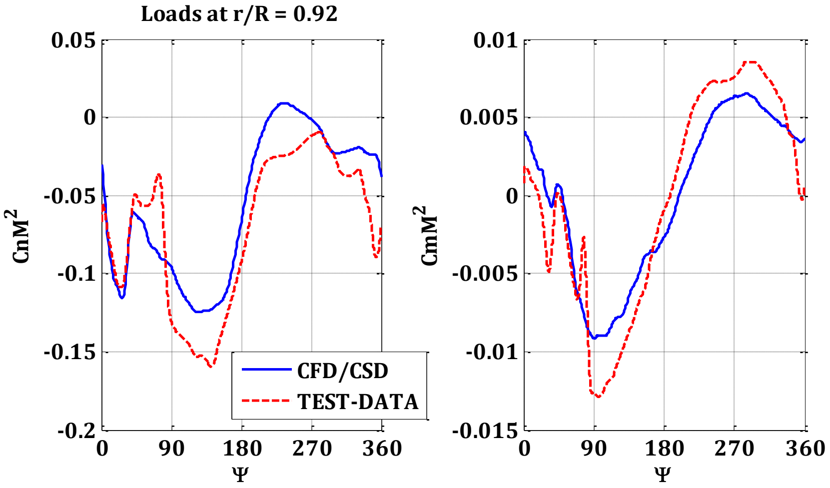

a. $C_T/\sigma = 0.02$, $\mu = 0.3$, **Test Run 4528**

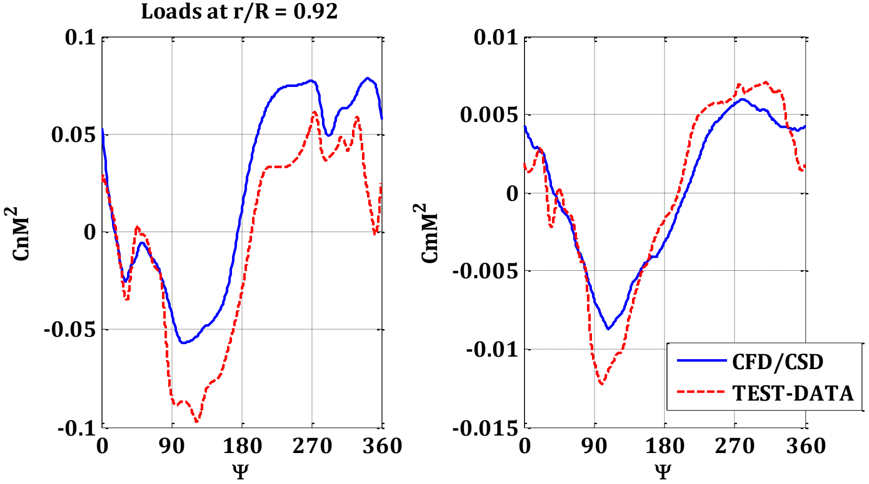

b. $C_T/\sigma = 0.06$, $\mu = 0.3$, **Test Run 4530**

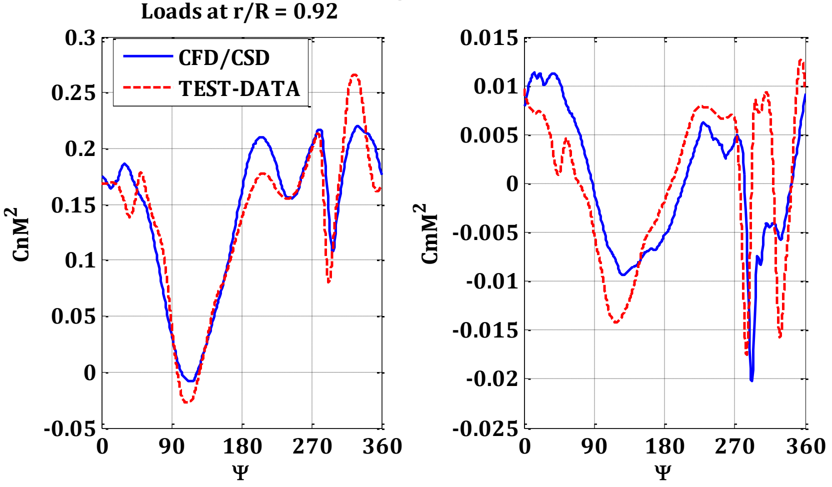

c. $C_T/\sigma = 0.12$, $\mu = 0.3$, , **Test Run 4540**

Figure 4.17 Comparison of measured and predicted sectional normal loads and pitching moments (means removed) at r/R = 0.92, for selected thrust sweep conditions.

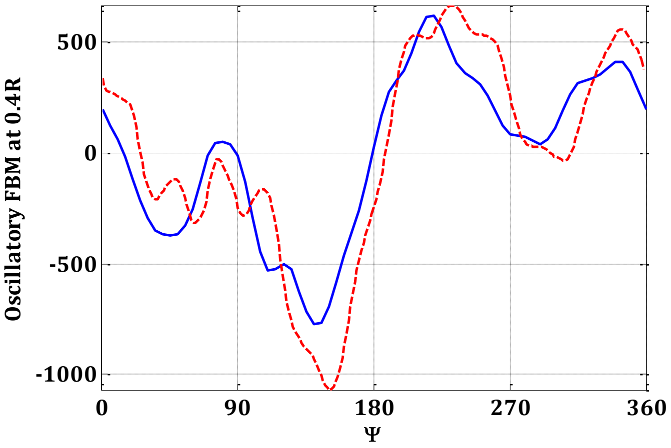

a. $C_T/\sigma = 0.02$, $\mu = 0.3$, **Test Run 4528**

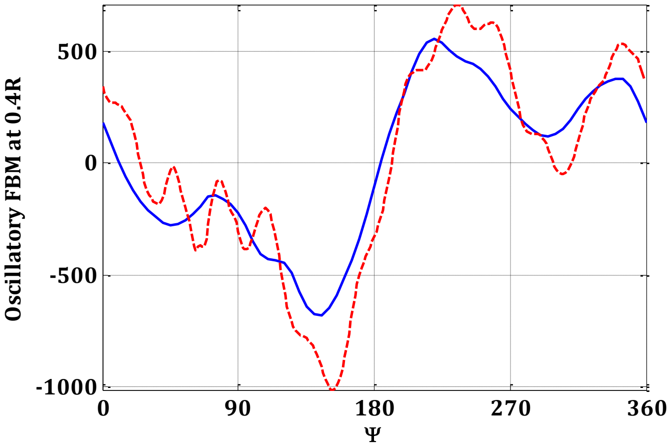

b. $C_T/\sigma = 0.06$, $\mu = 0.3$, **Test Run 4530**

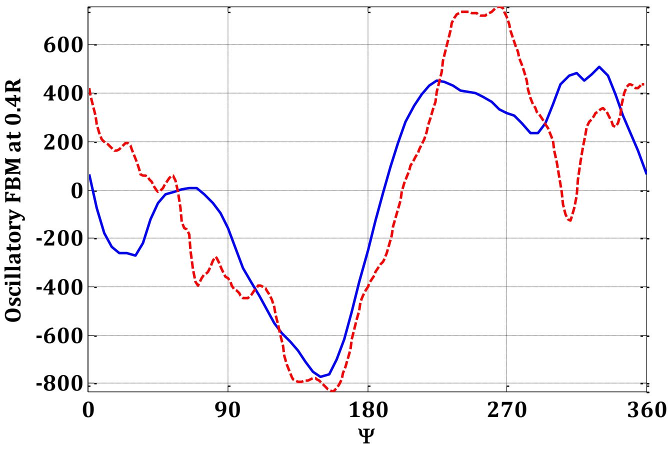

c. $C_T/\sigma = 0.12$, $\mu = 0.3$, **Test Run 4540**

Figure 4.18 Comparison of Flapwise Bending Moment at r/R = 0.4 for the thrust sweep conditions.

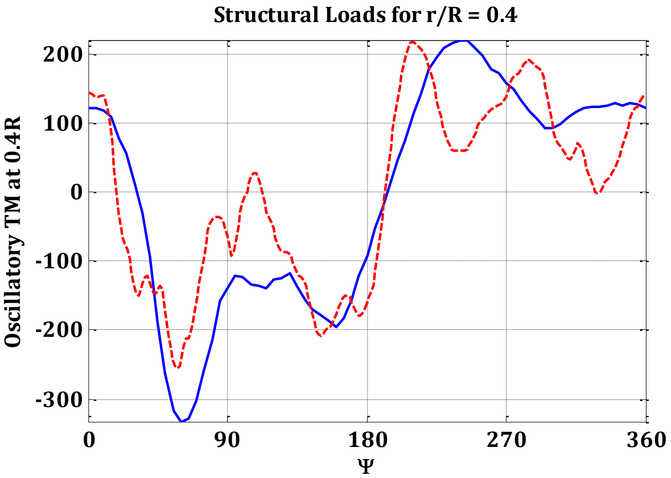

a. $C_T/\sigma = 0.02$, $\mu = 0.3$, **Test Run 4528**

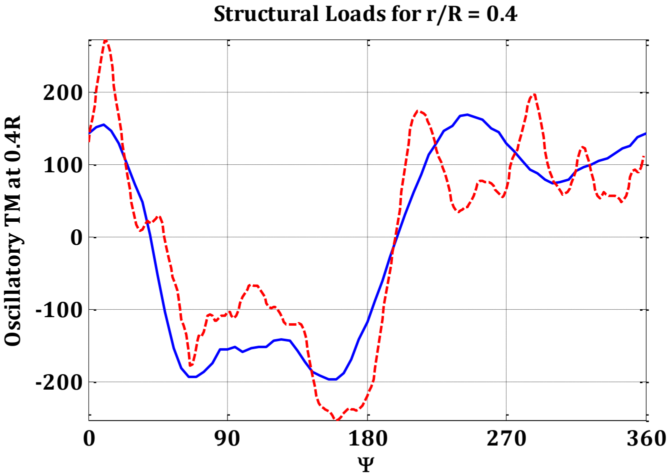

b. $C_T/\sigma = 0.06$, $\mu = 0.3$, **Test Run 4530**

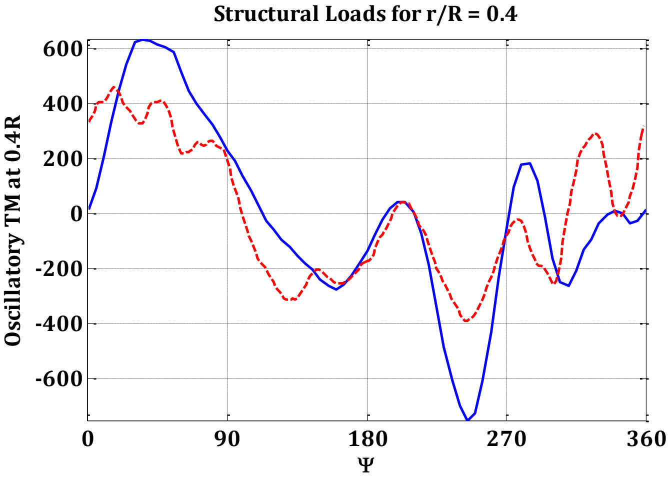

c. $C_T/\sigma = 0.12$, $\mu = 0.3$, **Test Run 4540**

Figure 4.19 Comparison of Torsional Moment at r/R = 0.4 for the thrust sweep conditions.

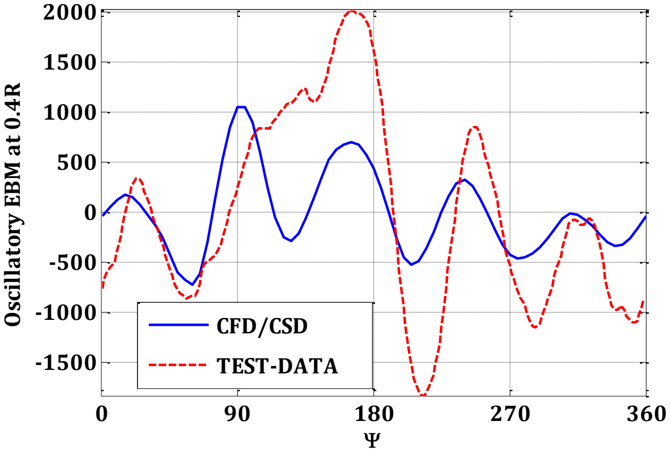

a. $C_T/\sigma = 0.02$, $\mu = 0.3$, **Test Run 4528**

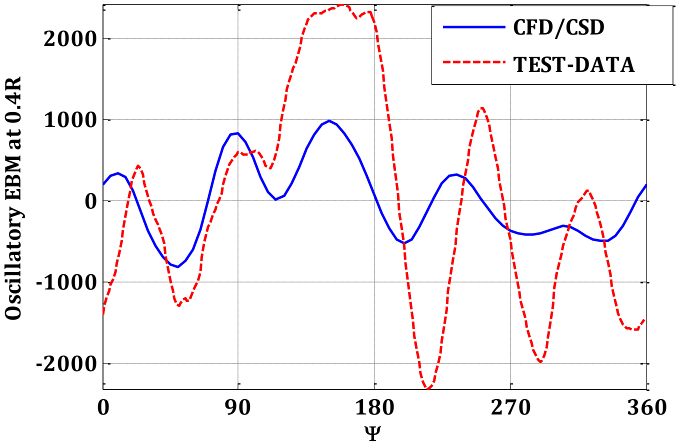

b. $C_T/\sigma = 0.06$, $\mu = 0.3$, **Test Run 4530**

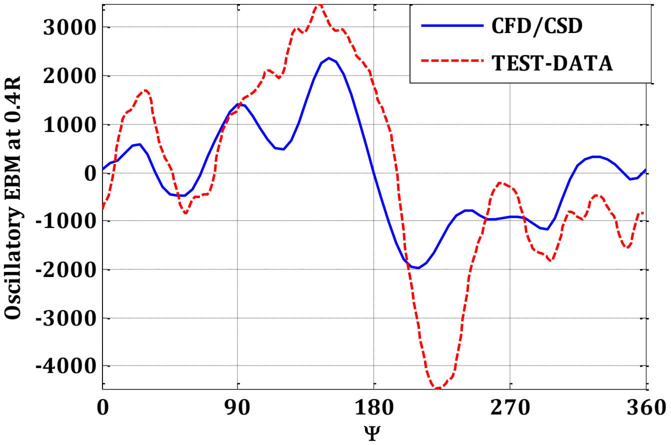

c. $C_T/\sigma = 0.12$, $\mu = 0.3$, **Test Run 4540**

Figure 4.20 Comparison of edgewise bending moments at r/R = 0.4 for thrust sweep conditions.

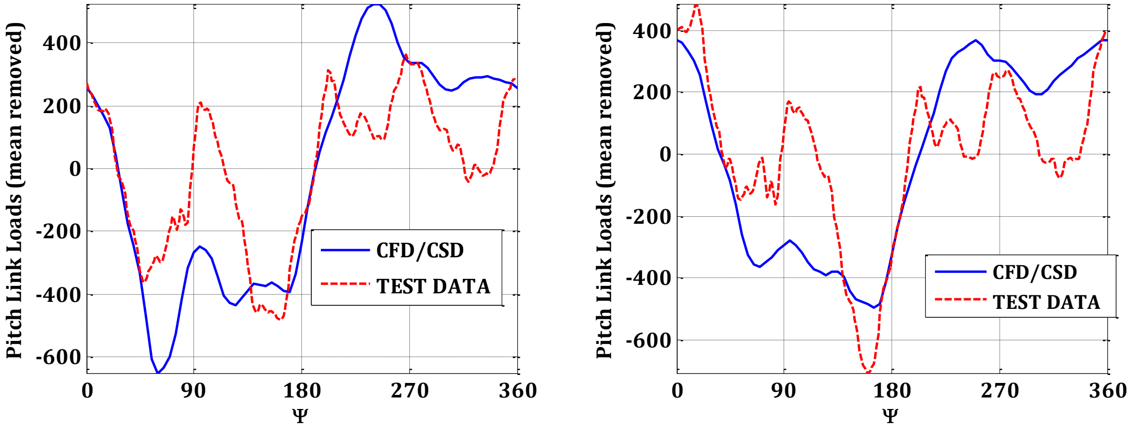

a. $C_T/\sigma = 0.02$, $\mu = 0.3$ **Test Run 4528**

b. $C_T/\sigma = 0.04$, $\mu = 0.3$, **Test Run 4529**

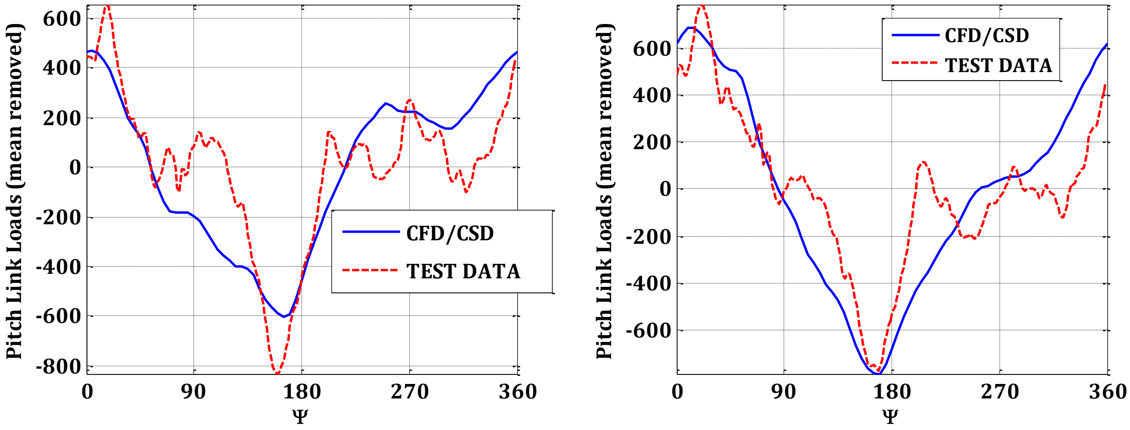

c. $C_T/\sigma = 0.06$, $\mu = 0.3$, **Test Run 4530**

d. $C_T/\sigma = 0.09$, $\mu = 0.3$, **Test Run 4533**

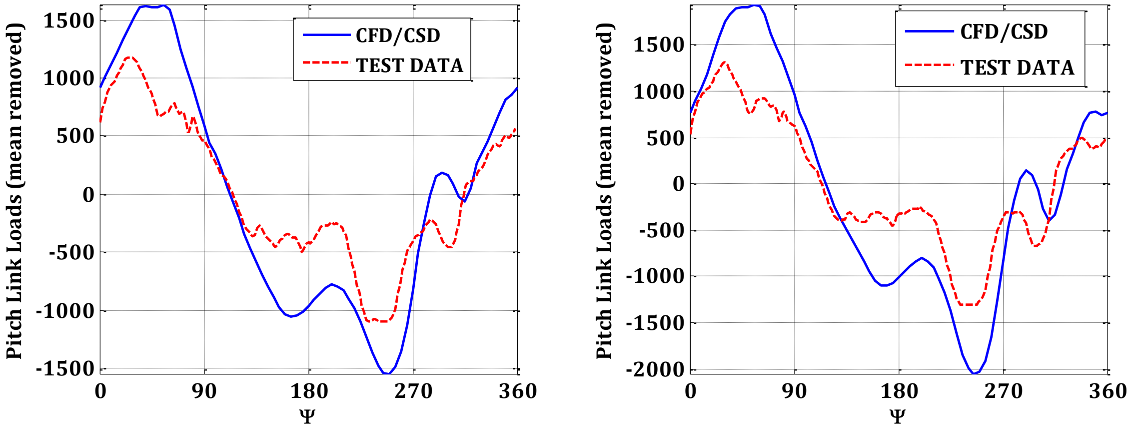

e. $C_T/\sigma = 0.1203$, $\mu = 0.3$, **Test Run 4536**

f. $C_T/\sigma = 0.1231$, $\mu = 0.3$, **Test Run 4540**

Figure 4.21 Comparison of measured and predicted blade oscillatory pitch link loads for thrust sweep conditions.

CHAPTER 5

UH-60A DIVING TURN MANEUVERS

As discussed in the introduction, the state-of-the-art in the prediction of rotor loads using coupled CFD and CSD analyses has seen significant progress over the past four decades. Much of this work has been for steady level flight conditions. However, loads prediction in unsteady maneuvers which is critical for peak design loads, continues to be a challenging task. The unsteady aerodynamic phenomena such as bundling of wake vortices, compressibility effects and extensive dynamic stall phenomena affect the rotor to various levels during maneuvering flight. The availability of the UH-60A Airloads database has opened the opportunity to gain a fundamental understanding on the principle mechanisms involved in various maneuvering flight conditions, as well as in improving the state-of-the-art in airloads prediction. This database [9] consists of highly repeatable and accurate set of flight test data for steady flight conditions and maneuvers. The data includes pilot input, vehicle attitudes, blade airloads and structural loads. Three extreme maneuvering flight conditions were recorded by the UH-60A rotor – a longitudinal pull-up (11029) maneuver, and two diving turn maneuvers (11680 and 11679). The most severe of all the three maneuvers is the right turn diving maneuver counter 11680 with a banking angle of 60 deg. This assessment is based on the highest loads for pitch-link force, torsion moment at 0.3R and root chord bending moment at 0.113R [10]. The flap root bending moment at 0.113R has been ranked fifteenth most severe.

In the current chapter, the focus is on the prediction of aeromechanical loads encountered during two transient maneuvering flight conditions for the UH-60A rotor: Counter 11680 and Counter 11679. This chapter is organized as follows. The test procedure and available data for the two diving turn maneuvers are first discussed. The structural model is next validated by utilizing the measured airloads, which helps in decoupling the physics of structural dynamics and aerodynamics. Next, CFD grid sensitivity studies are performed using a baseline coarse grid and a fine grid with the same set of blade deformations. Finally the blade aeromechanical loads, push-rod loads and harmonic content results are presented for the two maneuvers.

Diving turn maneuvers are high-speed and high-load factor turns where the available potential and kinetic energy of the vehicle is drawn upon to provide the power required to maintain a constant load factor. The high speed, diving turn is characterized by non-zero angular rates but nominally zero angular accelerations. The maneuvers extend well beyond the static stall limit (McHugh lift boundary) for steady flight counters as seen in Figure 5.1 and Figure 5.2. This gives rise to significant vibratory loads.

Counter	Climb rate (ft/min)	μ	n_z	C_T/σ
11679	-3878	0.393	1.69	0.1437
11680	-5324	0.388	1.48	0.1219

Table 5.1 Characteristics of two diving turn maneuvers.

Flight counters 11679 and 11680 are two right-turn diving maneuvers at 55 deg bank angle and 60 deg bank angle respectively, lasting about 9 seconds each. The characterization of these two maneuvers in terms of the advance (μ), normal load factor (n_z) and C_T/σ averaged over 39 revolutions has been recorded in Table 5.1. The transient maneuver conditions result in severe pitch link loads and represent design conditions for the military aircraft [114]. The pushrod loads experienced during severe maneuvers are about 2.5 times greater than the loads in maximum speed flight.

5.1 Flight Test Data – Diving Turn Maneuver, 11680

In the current section, the diving turn 11680 is studied. Figure 5.3 (a) shows the time history of angular rates for the dive turn maneuver based on rotor revolutions. While the yaw rate is relatively constant throughout the maneuver, the pitch and roll rates change considerably. At the start of the maneuver, the helicopter has a high pitch rate of 10.34 degrees/sec. As seen in Figure 5.3 (a), the vehicle experiences a peak pitch rate in Revs 8-11 with a peak average pitch rate of 11.1 deg/sec in the ninth revolution. Figure 5.3 (b) shows peak load factor, which occurs 2 revolutions later at Rev 11 with an average load factor of 1.9. Figure 5.3 (c) shows vehicle pitch (θ), angle of attack (α), and flight path angle (γ), while Figure 5.3 (d) shows side slip angle (β), roll attitude (φ) and heading ($\Delta\psi$) in the inertial frame. Figure 5.4 shows oscillatory pitch-link loads lagging the load factor time history by approximately a revolution with the peak pushrod loads occurring at Rev 12. The oscillatory pitch-link loads (half peak-to-peak) during the dive turn maneuver gradually increase starting from the first revolution. Peak pitch-link loads are developed at about Rev 11. Following revolution 14, the rotor thrust represented by load factor starts to decrease gradually and the pitch-link loads rapidly decrease until Rev 20. Lowest peak-to-peak pitch-link loads are found at the completion of the maneuver.

The advance ratio for this maneuver has an average value of 0.388 and a maximum of 0.404. During the maneuver, the rotor RPM is fairly constant with a value of 255 RPM. The gross weight of the aircraft is approximately 16400 lbs. Because of the high advance ratio combined with an average diving rate of 5324 ft/min, the flight test data has considerable amount of noise in the normal load factor and angular rates data.

Furthermore, there are possible sources of error in the static pressure measurements because of the effects of the fuselage on the air-stream.

5.2 Estimation of thrust target and hub moments for Maneuvers

The rotor thrust was not directly measured during the UH-60A Airloads Program. Thus it is not possible to directly evaluate the accuracy of the calculated rotor thrust. There are two ways of estimating the thrust- from the normal load factor as discussed below, or from the integrated blade pressure measurements of flight test data. The measured rotor thrust may be obtained via the gross weight of the helicopter plus estimates for the fuselage and tail rotor loads.

5.2.1 Limitations of Flight Test Data

Airloads are computed by integrating measured pressures over the blade chord. Even with exact pressure measurements, integration errors are introduced because of the limited number of transducers. The bias error in the transducers for the UH-60A test data was performed by comparing blade thrust with aircraft weight, after accounting for fuselage, stabilator download and tail rotor lift. Kufeld *et al.* [10] have shown that the integrated thrust is about 7% high and this is assumed to be the cause of errors in steady load measurements such as thrust target for flight test data.

The integration of the measured pressures over the rotor result in poor agreement with measured thrust and moments. For example, for the high speed test point (8534), the integrated thrust is 10% higher and the total integrated hub moment is 50% larger with an 80-degree phase difference compared to the measured values [77]. The fuselage and tail downloads are calculated from empirical model of the UH60 mathematical model [115], [116]. The mathematical model includes fuselage aerodynamic force and moment equations specific to the UH-60, a canted tail rotor, a horizontal stabilator with variable incidence. The sum of the fuselage, tail loads and rotor force is equal to the net z-force on the helicopter. Within the same maneuver, the fuselage and tail loads can be positive or negative for parts of the maneuver. For example, during the pull-up maneuver (Counter 11029) for the UH-60A, the fuselage and tail lift loads vary between a download of 1700 to maximum positive loads of 5000 lbs. The estimates for measured hub moments, vehicle roll, and pitch were determined from the upper shaft bending moment gauge measurements.

5.3 Structural Validation using Measured Airloads

The aeromechanical loads prediction for a rotor is an inherently coupled problem. Incorrect prediction of aerodynamic pitching moments would produce incorrect elastic twist which would, in turn, affect the blade circulation and the wake induced inflow. Therefore, in order to verify the structural model, it is important to isolate the physics of blade aerodynamics from the rotor trim and the blade structural dynamics. In an effort to do the same, the structural model is decoupled from the aerodynamic model and validated by imposing airloads obtained from flight test on the structural model. This method is known as the mechanical airloads problem, proposed by Ormiston *et al.* [117]. A prescribed set of airloads are imposed on the structural model, which remain fixed and do not change in response to blade deformations. The time-varying measured airloads are not contaminated with the errors associated with predicted airloads. However, since the prescribed airloads do not depend on the blade response, the system results in a zero aerodynamic damping, which renders the mechanical airloads simulation a fundamentally ill-posed problem. This poses a significant challenge in obtaining a converged periodic solution in steady level flight with no structural damping, as the 1P flapping frequency for the UH-60A rotor lies close to the rotor harmonics. Therefore, during the course of the analysis, an additional damping (0.02% of critical) was used in DYMORE methodology. The maneuver was initiated for 40-60 revolutions before the measured transient loads were introduced on the structure. The structural model consisted of a non-linear hydraulic lag damper model and the pilot controls and the measured airloads were prescribed. The flapwise and edgewise bending moments at 30%, 50% and 70% are compared with test data in Figure 5.5. In the normal bending moment data, there is a slight over-prediction of high harmonics compared to test data at 30% and 50%R, while the loads are under-predicted at 70%R. The edgewise bending moments are captured well in magnitude, while the mean loads are under-predicted. The waveform on the retreating side is not well-captured. Figure 5.6 shows torsional moments at 30% and 50%R. The torsional moments exhibit high frequency content on the retreating side, which has not been predicted accurately by the mechanical airloads simulation. The pushrod loads are shown in Figure 5.7. The agreement of the pushrod loads on the retreating side is not satisfactory despite using the hydraulic lag damper model. Note that the pitch link loads developed on the helicopter during the diving turn is the severe most experienced by the UH-60A rotor. Therefore, in order to accurately capture the retreating side waveform and the higher harmonic content, the structural model needs to be further refined. Improvements to the structural model may be made by systematically refining individual structural components (swash-plate model, hub motion) and through correct specification of root boundary conditions. The structural loads obtained from the coupled CFD/CSD analysis are expected to be of inferior quality compared to the structural loads due to the inaccuracies stemming from aerodynamic prediction.

Next, the deformations obtained from the mechanical loads problem are imposed on the CFD model in order to perform grid sensitivity studies.

5.4 Grid Sensitivity Study

The prediction quality of airloads for a particular high load revolution (Rev 12) of the diving turn maneuver was studied by employing 3 different grids. The baseline grid consists of 131 in the streamwise, 65 in the spanwise and 45 in the normal direction. Two additional grids with the same y^+ values were created. The first grid has twice the grid density over the baseline grid, in the streamwise and normal direction, while the spanwise grid density was maintained the same (263×65×90). Thus, the effect of increasing the grid density only along the direction of propagation of normal shock was studied. The second grid consisted of twice the grid density in all the 3 directions (263×128×90). A common set of prescribed deformations obtained through the structural validation study, discussed in the previous section were applied to the 3 different grids in order to study the sensitivity of the airloads prediction using different grid densities. For all the grids, the exact same wake representation namely multiple trailer wake model with 4 revolutions of shed wake, was used. This ensures that the differences in airloads prediction are exclusively due to the changes in grid density.

Figure 5.8 shows sectional airloads at the inner spanwise stations (22.5%, 40% and 67.5% R). At the inner-spanwise locations of 22.5%, 40% and 67.5% the negative pitching moments on the blade, right above the aircraft nose (between $\psi = 135°$ and $\psi = 180°$) are characteristic of excessively high blade loading value (~1.7) for this revolution.

The pitching moments at the inboard locations for grids 1, 2 and 3 differ. At radial stations greater than 67.5%R (Figure 5.9), the pitching moment phase associated with first dynamic stall shifts in the right direction for grids 2 and 3 compared to the baseline grid. Additionally, grids 2 and 3 show improved prediction of compressibility effects in the normal loads at the out-board stations, which is due to the finer grid density in the shock-propagation direction. The advancing side stall phenomenon, as observed in test data for the outer spanwise stations near $\psi = 45°$, is not captured by the current predictions. This is attributed to the fact that the prescribed blade motions obtained from the mechanical airloads solution do not contain the aeroelastic response terms which are required for capturing the 5P torsional response, essential for predicting the third stall phenomena. At blade location r/R = 0.92, the finer grids tend to over-predict the dynamic stall cycles. Accurately capturing the complex aerodynamics at the blade tip is a challenging task which is dependent on the grid topology as well as grid spacing near the tip. The tip loads are also significant and have an impact on the prediction of pitching moment, torsional loads and the torque. Thus, the tip planform and the shape in the wrap-around direction need to be carefully accounted for.

Quantitative metrics for assessing the quality of CFD grid are obtained through metrics evaluated using linear regression (as documented in Appendix A). The slope (m) and coefficient of determination (r^2) for baseline grid, fine grid and finest grid have been plotted for sectional pitching moments in Figure 5.10. It is seen that the finer grids have a better slope (m), and coefficient of determination (r^2), closer to unity in the mid span region ($0.5 < r/R < 0.8$). The metrics for sectional normal loads as a function of percentage radius are plotted in Figure 5.11. It is seen that the baseline grid results in a slight over-prediction of slope (m) at the inboard radial locations, while the slope improves for finer grids at the outboard locations ($0.9 < r/R < 1$). The coefficient of determination (r^2) in Figure 5.11 consistently shows decreased quality of prediction near r/R = 0.775. The reduced quality of predictions at this station is hypothesized to be due to the presence of the trim-tab on the blade at this radial location.

Based on these studies, it was concluded that the baseline 131 x 65 x 45 coarse grid is a satisfactory compromise between solution accuracy and computational time. This grid is able to qualitatively capture much of the flow physics. Therefore, the baseline coarse grid has been used for all further results.

5.5 Aeromechanical Loads Prediction

Accurate estimates of the mean values, peak values, peak-to-peak variations and harmonic content of structural loads are all important for adequate sizing of the blades and the hub. Aeromechanical loads prediction was carried out for the first 15 revolutions of the maneuver, since it comprises of the most severe part of the maneuver, in terms of normal load factor and peak-to-peak of pitch-link loads. A loose CFD-CSD coupling methodology was used, and each revolution was simulated as a separate run. Detailed aerodynamic and structural loads for the rotor revolution with the highest load factor have also been computed with the aim of identifying important flow phenomena.

5.5.1 Sectional Airloads Using Trim Targets

Blade sectional airloads consisting of sectional normal loads and pitching moments for the first 10 revolutions are shown in Figure 5.12- Figure 5.15. The mean loads as well as the waveform are captured reasonably well for this extreme maneuver.

The stall characteristics for each revolution remain the same except for differences in magnitude of the loads. It is observed that although the inboard stations give accurate loading results at the 0 and 180 (nose) azimuth positions, there was a phase difference between simulated and flight test data for stations outboard of 0.675R to the tip.

Although strictly speaking the diving turn is a transient maneuver, the waveform is repeated between one revolution to the next, indicating that this is a relatively slow maneuver. This justifies the use of the loosely coupled CFD/CSD analysis for this maneuver. The flow features for a revolution (Rev 12) with the highest push-rod loads are examined in detail.

The non-dimensional sectional normal loads for Rev 12, characterized by high load factor of 1.89, obtained using CFD/CSD and CFD with prescribed deformations are shown in Figure 5.16. The normal loads at 67.5% radial location indicate the first occurrence of stall at 210 deg followed by another stall at 270 deg. Lift stall is observed beginning in the fourth quadrant, continuing into the first quadrant at radial locations between 0.675R and 0.865R. This stall has been predicted with a phase lag of about 12 deg compared to flight test data.

For the same representative revolution (Rev 12), pitching moment data with the means removed have been plotted in Figure 5.17. Moment stall for this flight condition is observed at nearly all the radial stations. At 22.5%R, moment stall occurs between 140 and 160 deg as indicated by flight test data, whereas there is a phase lag of about 15 deg observed in the simulated results shown on the same plot. At 40%R moment stall is observed at about 170 deg in both measured and predicted data. At the inner-spanwise locations of 22.5%, 40% and 67.5%R the negative pitching moments on the blade in between ψ = 135° and ψ = 180° are characteristic of high thrust flight condition for the UH-60A rotor. This behavior is also observed at high blade loading values of the parametric thrust sweep for the wind tunnel UH-60A tests, as discussed in Chapter 4. At the outboard locations of 67.5%R to 77.5%R, moment stall associated with first dynamic stall cycle is seen in the flight test data near 210 deg. This first dynamic stall cycle lags the test data by 4-5 deg. This stall event is three-dimensional in nature, over a narrow azimuth 67.5%-77.5%R. A second stall cycle is apparent from 67.5%R to the tip and occurs between 330 and 360 deg. A third cycle occurring at about 45 deg in the first quadrant causes large moments from 77.5%R to 92%R. The third dynamic stall vortex sheds from a location with pre-dominant supercritical flow over the front of the airfoil. This complex interaction between the supercritical flow and dynamic stall vortex has been captured by the CFD/CSD simulations with a phase lag.

In Figures 5.16 and 5.17, CFD results using prescribed deformations do not predict the advancing side stall phenomena observed at the outer-blade locations, indicating that the torsional response prediction is essential for capturing this event. However, the CFD/CSD simulations are able to capture this event. There is also a fourth stall cycle present in the flight test data in the first quadrant at 0.92R location in the pitching moment data, which has been captured by the CFD/CSD prediction while it has not been predicted by CFD with prescribed deformations. It may be inferred that the dynamic stall events in the first quadrant occur quickly since they occur over a small range of azimuth of five to ten degrees. The prediction of sectional pitching moments as a function of percentage radius is assessed using the metric suggested by Bousman, tabulated in Table 5.2 and plotted in Figure 5.18. It is seen that CFD with prescribed deformations performs better at the inboard stations while the CFD/CSD coupled analyses yield slightly better results at the midspan stations.

In Ref. [114], Bousman makes the observation that “torsional dynamics of the rotor controls determine where the dynamic stall may occur, while the flight condition and the resulting aerodynamic inflow determine whether it will occur.” Thus, the prediction of dynamic stall is dependent on torsional dynamics or inflow distribution at that location, or possibly both. Since the advance ratio is considerably high, major contribution to the dynamic stall event is due to the torsional response. The dynamic stall events are sensitive to the blade sectional angle of attack which is in turn dependent on control pitch angle, the elastic torsional response as well as induced flow angle. The induced flow angle is dependent upon the wake of the blade, the inflow induced by the other blades and the flow induced by the fuselage. These angles are not easily captured due to the complex interaction between flow features in a severe maneuvering flight condition.

5.5.2 Blade Structural Loads

The Normal bending moments at 0.3R and 0.5R blade sections for the first 10 revs have been plotted in Figure 5.19. The peak-to-peak and mean values of the normal bending moment have been captured reasonably well. The time histories of normal bending moments are captured well in magnitude and phase. At 0.3R location, there is a spike observed in normal bending moment time history at the beginning of every rotor revolution. This may possibly be due to over-prediction in lift coefficient at this azimuthal location (ψ=0). The waveform and peak-to-peak normal bending moments at

0.5R are captured well and the prediction results are consistent with flight test data at this radial station.

The torsional moments for the first 10 revolutions are shown in Figure 5.20. Torsional moments at any given location are both a function of elastic response at that station as well as the torsional loads acting on the blade outboard of that station. Although peak-to-peak is being captured reasonably well, torsional moments at 0.3R show that the waveform is not predicted accurately at the 210 deg azimuth position. The waveform of the torsional loads at 0.3R is quite similar to the waveform of the pitch-link loads developed during the maneuver, as seen in Figure 5.21. There is an over-prediction of compressive push-rod loads in the third quadrant between $\psi = 180°$ and $\psi = 225°$. Harmonic content for the pitch-link loads has been plotted in Figure 5.22. While 1P, 2P, 3P magnitude and phase of pitch-link loads are predicted reasonably well, 4P, 5P and 6P magnitudes are under-predicted.

The harmonic content (magnitude) of the normal bending moments of a representative revolution (Rev 7) has been plotted in Figure 5.23. The variation of each harmonic vs. radial station has been plotted for flight test and predicted data. The over-prediction in normal bending moment at 0.3R, as seen in Figure 5.19, may be attributed to the incorrect prediction of 4P harmonic at this radial location. Since the magnitude of harmonic content at 0.5R are predicted close to flight test results, the time history results at this station are consistent.

Examining the harmonic content of the torsional loads at 0.3R and 0.5R, as seen in Figure 5.24, shows that there is inconsistency in the prediction of 4P harmonic at 0.3R location with the CFD/CSD model. However, the harmonic 4P is predicted well in magnitude at 0.5R location. This explains the difference in prediction quality of time histories of torsional moments (Figure 5.20) at 0.3R and 0.5R locations. In particular, the wake model being used for these simulations is one that uses uniformly spaced wake trailers, whose vorticity is based on the strength of the bound circulation in the Navier-Stokes domain. Alternate wake models that better represent the wake developed during diving turn maneuver are expected to shed some light on the under-prediction of 4P harmonic.

5.6 Diving Turn Maneuver 11679

This maneuver was computed using a methodology identical to that for 11680. Figure 5.25 (a) shows the time history of angular rates for the dive turn maneuver C11679 based on rotor revolutions. While the yaw rate is relatively constant throughout the maneuver, the pitch and roll rates change considerably. At the start of the maneuver, the helicopter has a pitch rate of 6.26 deg/s. The vehicle experiences a peak pitch rate at Rev 15 with a peak average pitch rate of 9.4 deg/s. The load factor changes relatively slowly over the first 10 revolutions as shown in Figure 5.25 (b). The vehicle attitudes, angle of attack and sideslip angle are shown in Figures 5.25 (c) and (d). The vehicle pitch attitude does not coincide with the vehicle angle of attack, the difference being the flight path angle for this maneuver. The sideslip is nominally zero throughout the maneuver with the vehicle roll attitude varying between a minimum of 55 deg and maximum of 60deg. The alternating pitch-link loads (half peak-to-peak) during the dive turn maneuver C11679 gradually increase reaching a peak at Rev 28, as shown in Figure 5.26. Lowest half peak-to-peak pitch-link loads are found at Rev 10. The slight variation in rotor RPM was accounted for in the structural and aerodynamic models.

5.6.1 Sectional Airloads, C11679

Blade sectional airloads consisting of sectional normal loads and pitching moments for the first 7 revolutions are shown in Figure 5.27 - Figure 5.30. The mean loads as well as the waveform are captured reasonably well for this extreme maneuver. The stall characteristics for Revs 1-7 remain the same except for differences in magnitude of the loads. For Maneuver 11680, the starting revolutions are characterized by a high load factor of nearly 1.9, which causes the rotor to operate in complex aerodynamic environment starting from maneuver initiation. Unlike the first few revolutions of Maneuver 11680, there is no advancing transonic stall observed for the starting revolutions of Maneuver 11679, since the normal load factor is less than 1.5. It is observed that although the inboard stations give accurate loading results at the 0 and 180 (nose) azimuth positions, stations from 0.675R to the tip have a phase difference between simulated and flight test data. Although mean loads are predicted reasonably well, the peak loads especially at the 0.675R and 0.775R are not adequately captured. Lift stall is observed beginning in the fourth quadrant, continuing into the first quadrant at radial locations between 0.675R and 0.865R, as seen in Figure 5.28. This stall has been predicted with a phase lag of about 12 deg compared to flight test data.

The pitching moment data without removing the means have been plotted in Figures 5.29 and 5.30. In Figure 5.29, at the inboard stations 0.225R and 0.4R, negative pitching moments are observed at 170 deg azimuth over the nose of the vehicle likely due to increased angle of attack resulting from flow over the fuselage. This effect is not accurately captured in the predictions, since the fuselage is not being simulated. Moment stall for this flight condition is observed at almost all the radial stations. At 0.225R, moment stall occurs between 140 and 160 deg as indicated by flight test data. At 0.4R moment stall is observed at about 170 deg in both measured and predicted data. At the outboard locations of 0.675R to 0.775R, moment stall associated with first dynamic stall cycle is seen in the flight test data near 210 deg. The first dynamic stall event is three-dimensional in nature and sets in at 0.775R and becomes more pronounced as one goes out-board in the span-wise direction, as seen in Figure 5.30. A second stall cycle occurs between 330 and 360 deg.

Similar to Rev 12 of Maneuver 11680, Rev 20 of Maneuver 11679 is characterized by peak-load factor of 1.7g, and an advance ratio 0.3 for Maneuver 11679. Therefore, Rev 20 has been studied in detail. The sectional normal loads and pitching moments at selected stations for this revolution are presented in Figure 5.31. In this revolution, the advancing side stall event is seen in addition to stall cycles on the retreating side. At 0.775R the first stall vortex sets in at about 220 deg azimuth. The sectional airloads for this revolution are very similar to the aerodynamic loading observed in Rev 12, Counter 11680. Multiple and distinct localized stall cycles are observed toward the blade tip region. Over the retreating side, there is a large region of separated flow, which extends to the first quadrant, following which there is advancing side stall seen at about 45 deg azimuth, similar to that found in Rev 12, Counter 11680.

For a high thrust flight condition (C9017) of the UH-60A consisting of two stall cycles on the retreating side, a study by Datta *et al.* [12] showed that the first retreating blade stall was caused by high trim settings (collective and longitudinal control) which led to high local angles of attack on the retreating blade. If the trim state is correctly computed, the first stall event may be captured. His study also showed that the second stall event which occurs a few degrees of azimuth behind the first stall event is due to the 5P elastic twist deformation. In order to capture the second stall event, it is important to employ accurate aerodynamic and turbulence models so that the flow reattachment and separation is captured adequately. Very often, the flow may not reattach leading to the merging of first and second stall events indistinguishable from each other, spreading over a large region on the retreating side. The third stall event in the diving maneuvers is associated with supercritical flow over the front of the leading edge [114]. Accurate prediction of the retreating stall cycles is important for capturing the advancing side stall which is affected by a right combination of control angles, elastic twist as well as effective angle of attack.

5.6.2 Structural Loads, C11679

Normal bending moments at 0.3R and 0.5R blade sections for the first 6 revs have been plotted in Figure 5.32. The first thing that is observed is that the load behavior between one revolution and the other are repetitive showing periodicity in solution. The peak-to-peak and mean values of the normal bending moment have been captured reasonably well. The time histories of normal bending moments are captured well in magnitude, however there is a phase difference observed. Similar to the previous maneuver, there is a spike observed in normal bending moment time history at 0.3R location at the beginning of every rotor revolution. This may possibly be due to over-prediction in lift coefficient at this azimuthal location (ψ=0) or an artifact of solution restart for every revolution. The waveform and peak-to-peak normal bending moments at 0.5R are captured well and the prediction results are consistent with flight test data at this radial station. There is an over-prediction of compressive push-rod loads in the third quadrant between $\psi = 180°$ and $\psi = 225°$.

5.7 Summary of Results

1. The mean and waveform of sectional normal loads and pitching moments were captured moderately well despite the severity of the maneuver. In particular, the peak-to-peak sectional airloads at inboard locations are modeled reasonably accurately.
2. Due to the combination of high advance ratio (0.4) and high normal load factor (1.8), there is extensive occurrence of dynamic stall phenomena. The interaction of dynamic stall vortex with supercritical flow is critical for this maneuver, and crucial for the prediction of the advancing side third stall event at 0.675R to 0.775R radial locations. This was not captured by the current simulations.
3. The peak-to-peak structural loads and the mean loads are accurately predicted. The harmonic content of structural loads with harmonics 1P to 3P is well-captured.
4. The prediction quality of harmonic content of structural loads varies with radial location. For instance, for the torsional moments, the 4P harmonic 4P is well predicted at 0.5R location, while it is poorly predicted at 0.3R location.
5. The peak-to-peak pitch-link loads were reasonably well-predicted and the time history of pitch-link loads correlates well with the time history of blade torsional moment at 0.3R. However, there is an inconsistency in the prediction of the pitch-link loads at $\psi = 180°$.
6. Harmonics 4P to 6P of structural loads were not accurately captured. However, the higher harmonic content (> 7P) of pitch-link loads was adequately captured.

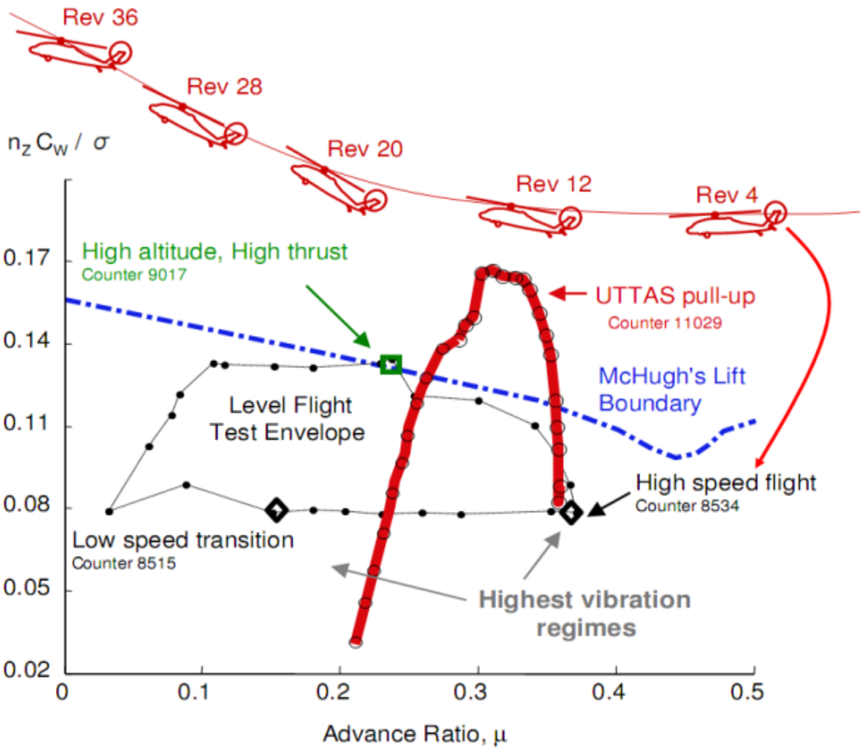

Figure 5.1 McHugh's Lift Boundary [16]

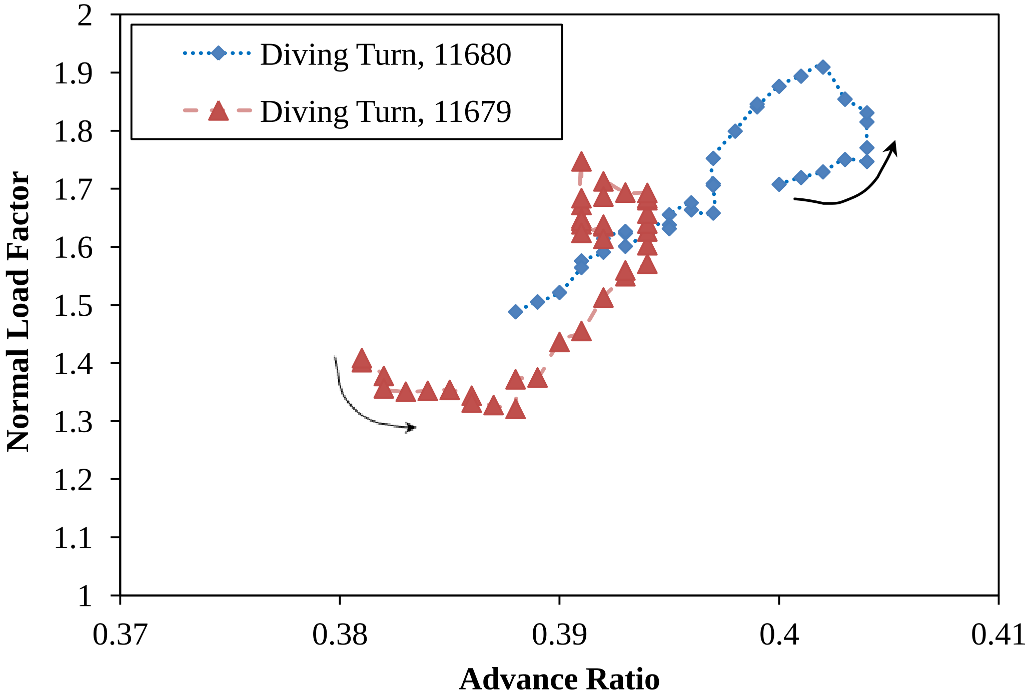

Figure 5.2 Advance ratio vs load factor for 11680 and 11679

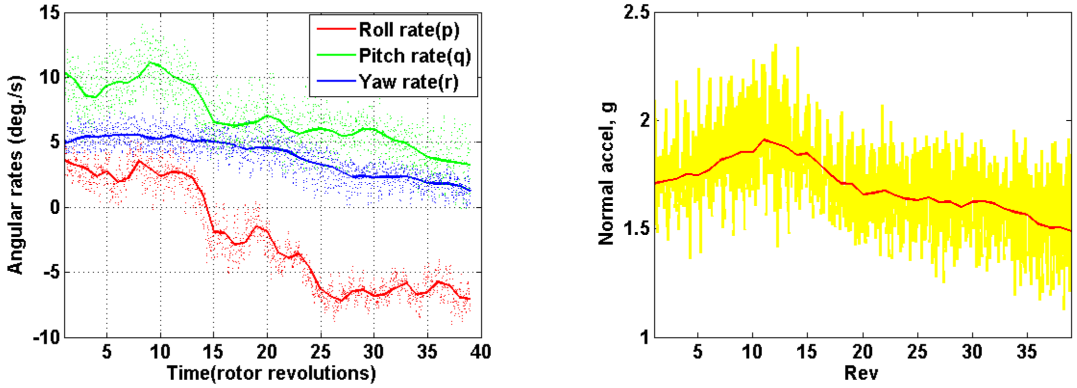

a. Angular rates

b. Normal load factor

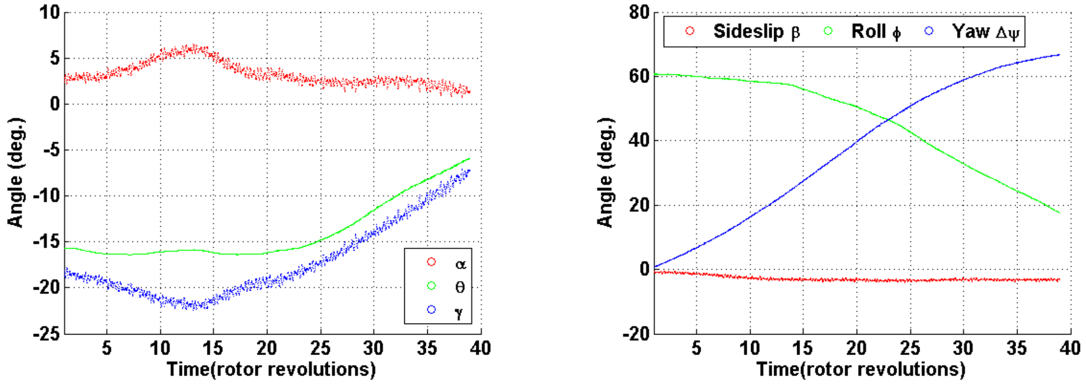

c. Angle of attack, pitch attitude, flight path angle

d. Sideslip angle, roll attitude and yaw attitude

Figure 5.3 Angular rates and normal load factor for 11680.

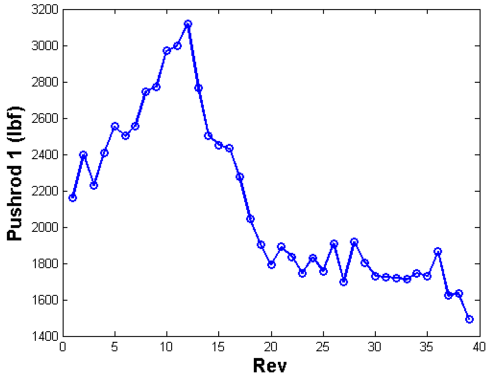

Figure 5.4 Alternating push-rod loads, for 11680.

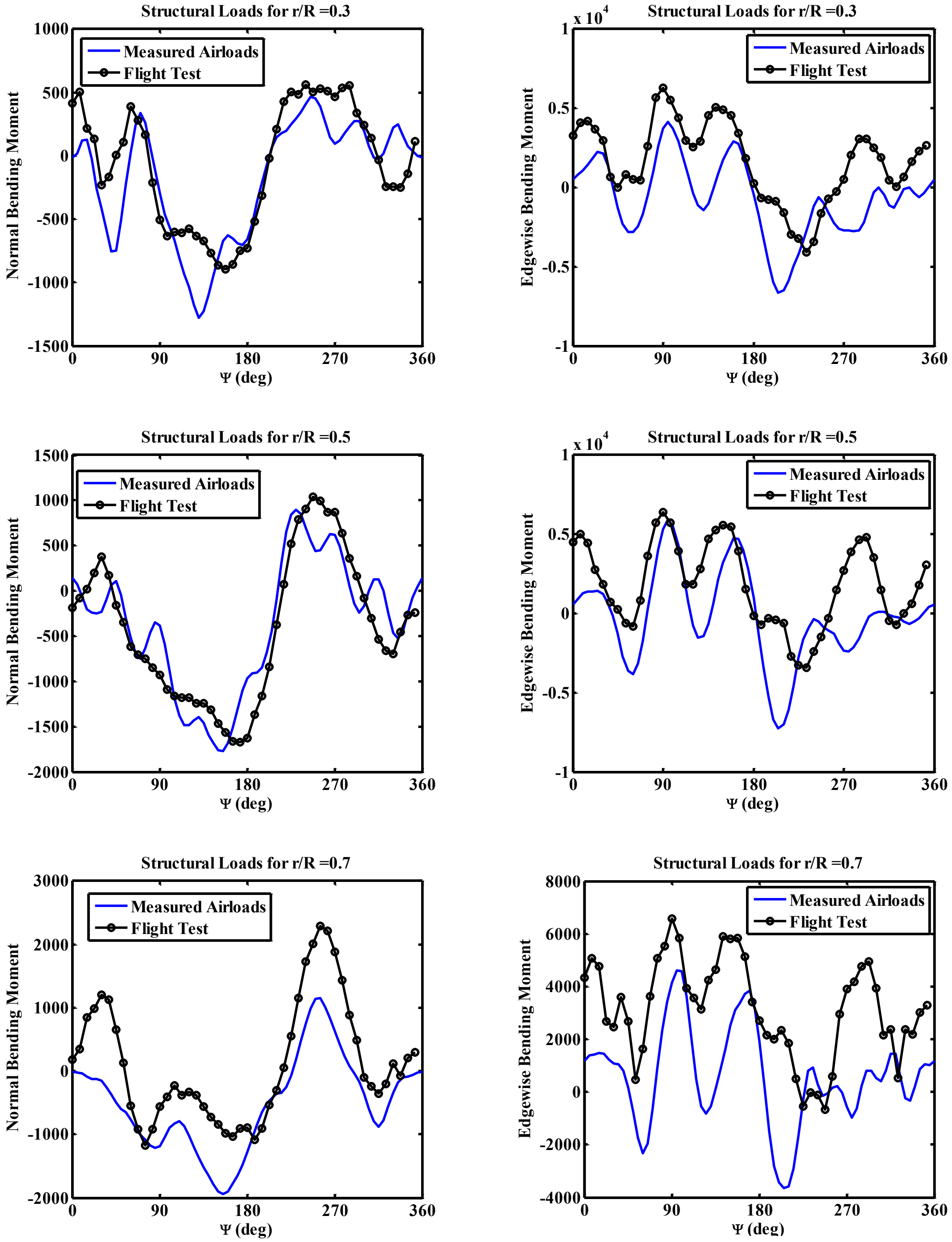

Figure 5.5 Flapwise and Edgewise Bending Moment at 30%, 50% and 70% radius for a rotor revolution with peak-load (Rev 12). Predictions are made using flight-test airloads.

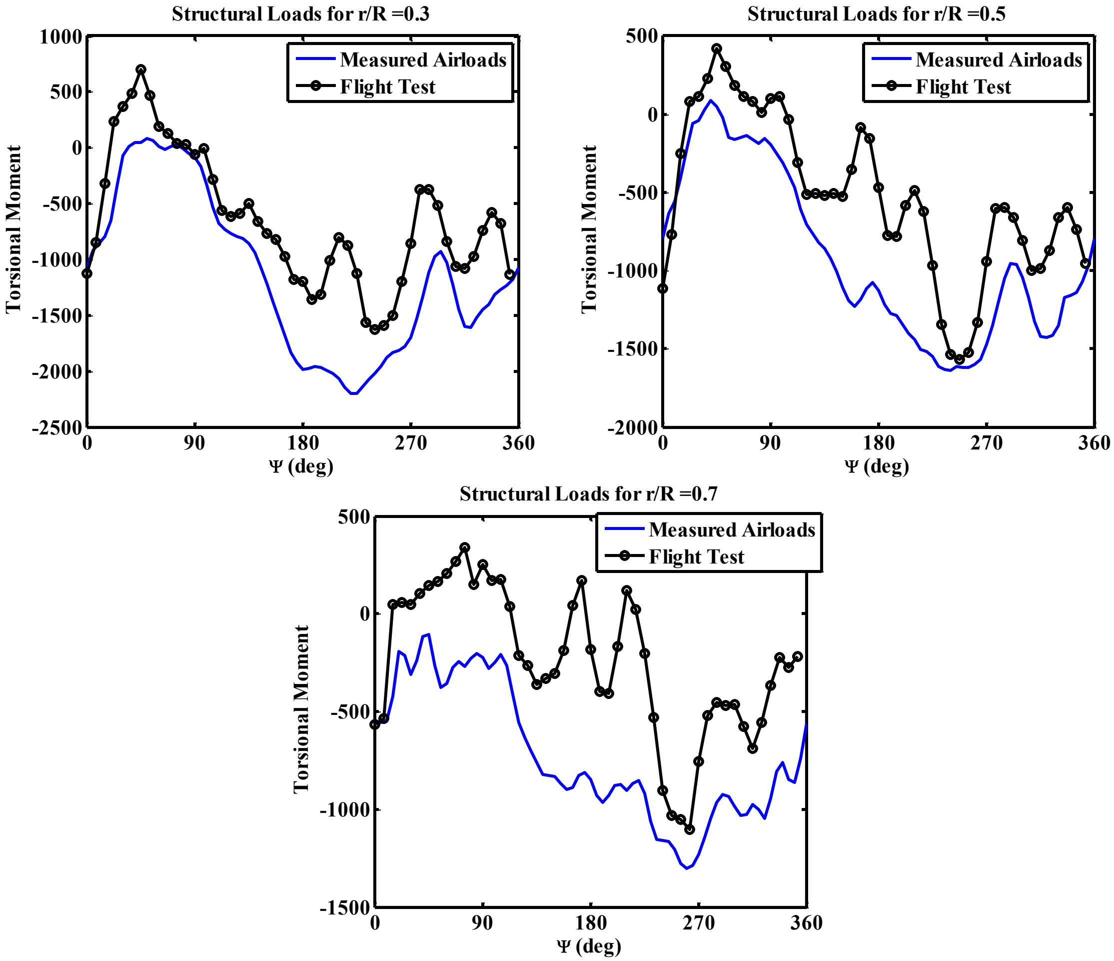

Figure 5.6 Torsional Moments at 30%, 50% and 70% radius for a rotor revolution with peak-load (Rev 12). Predictions are made using flight-test airloads.

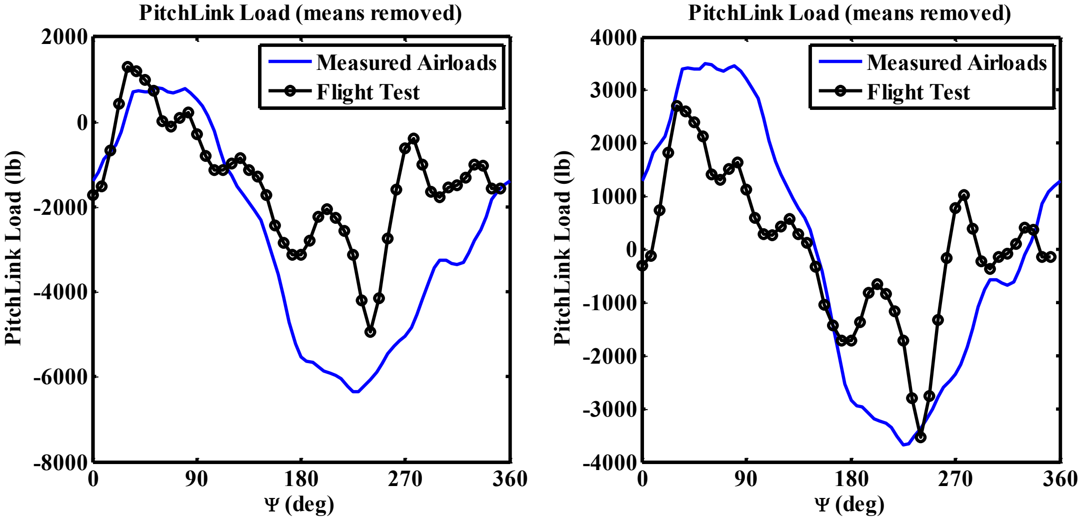

Figure 5.7 Push-rod loads for a rotor revolution with peak-load (Rev 12).. Predictions are made using flight-test airloads.

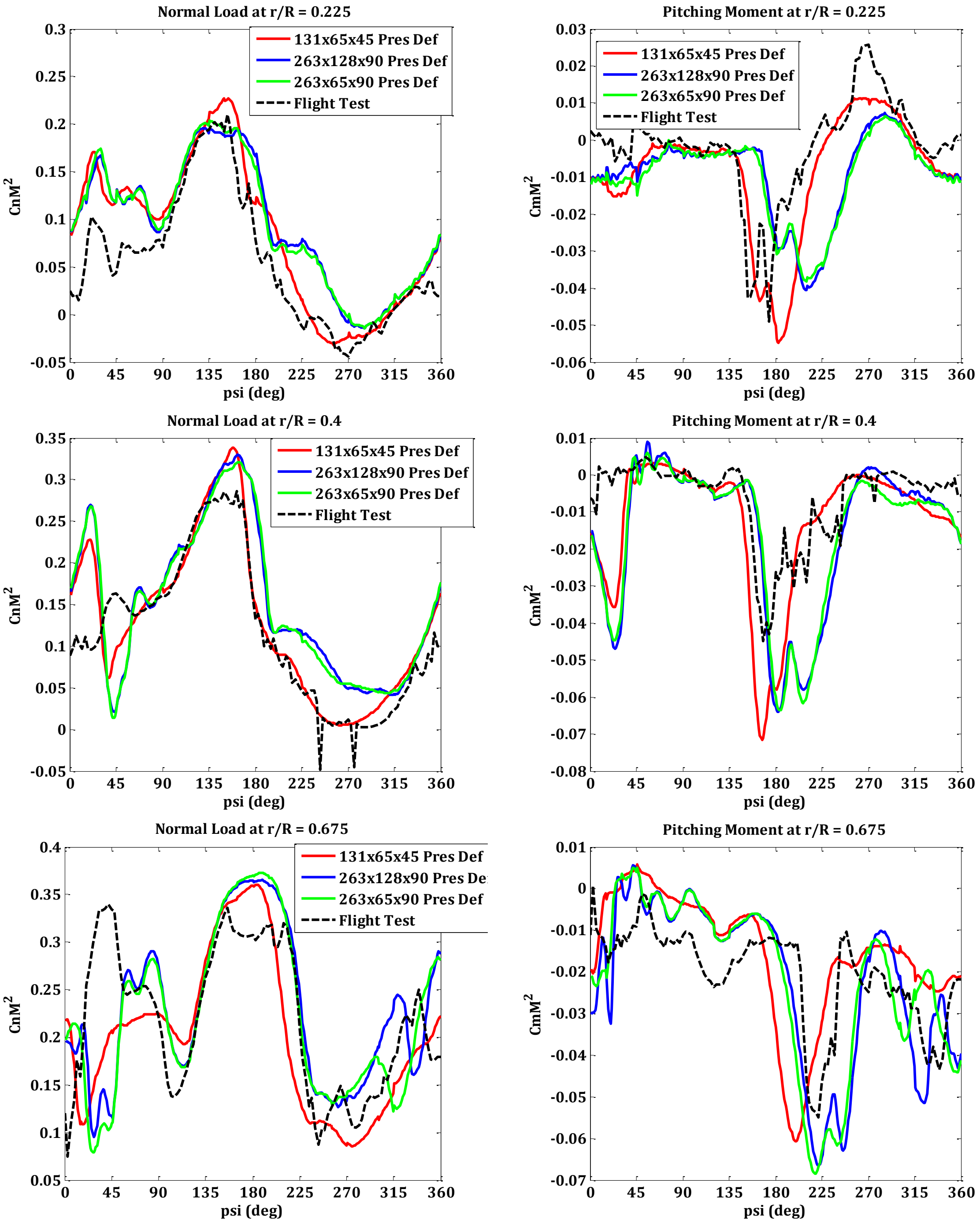

Figure 5.8 Sensitivity of the predicted sectional airloads to grid size. Inner-spanwise locations.

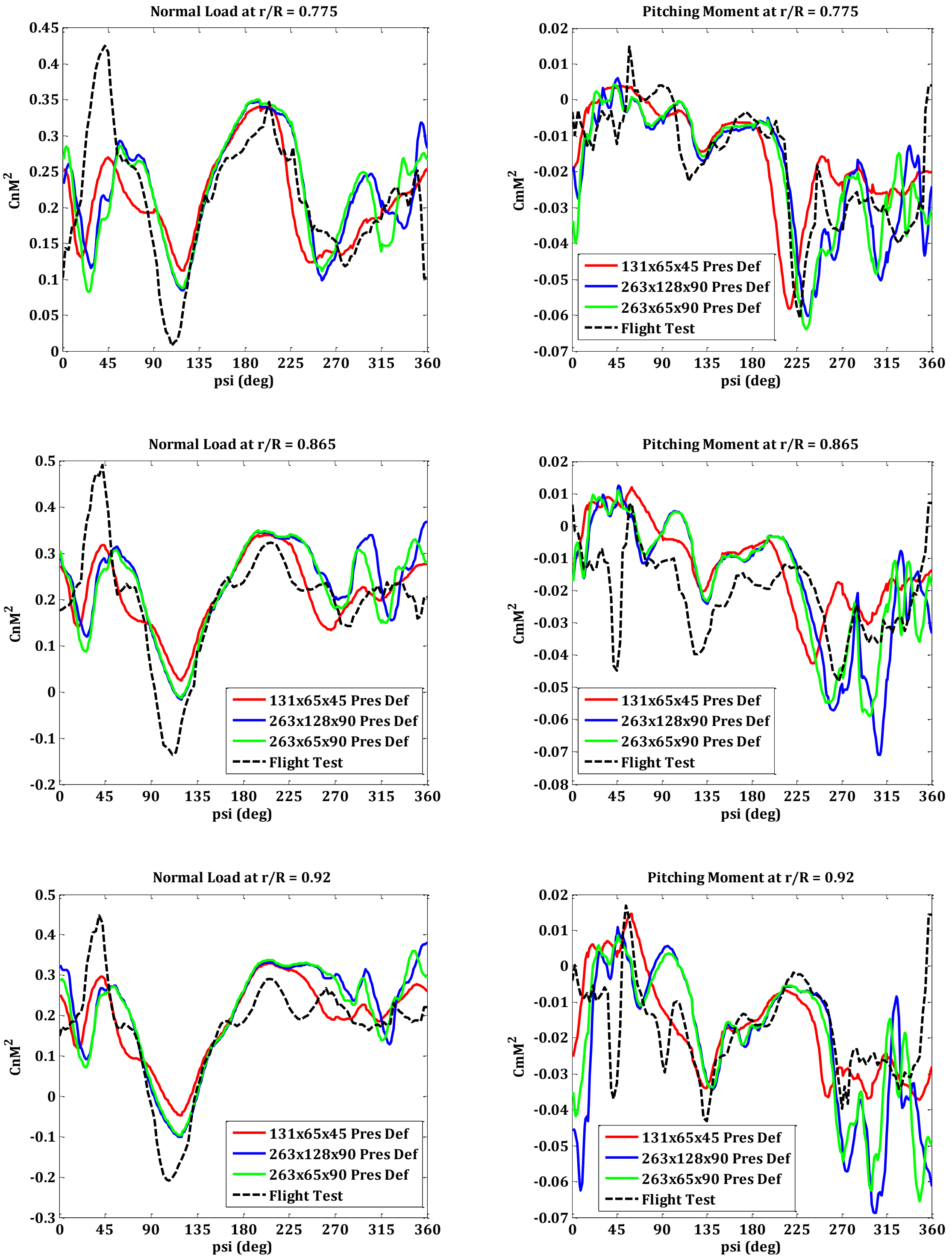

Figure 5.9 Sensitivity of the predicted sectional airloads to grid size. Outer-spanwise locations.

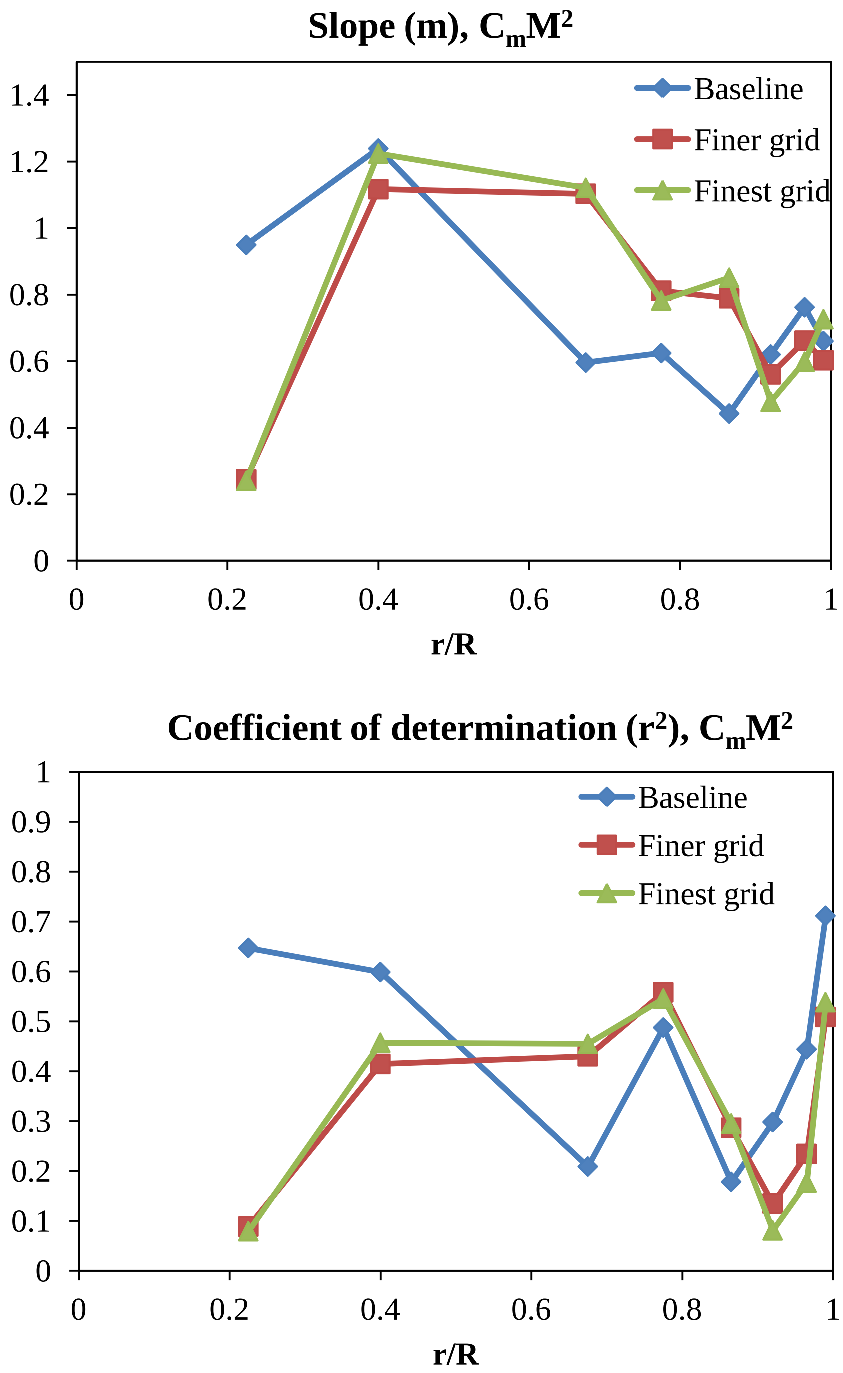

Figure 5.10 Quantitative assessment of grid sensitivity for sectional pitching moments as a function of radial station

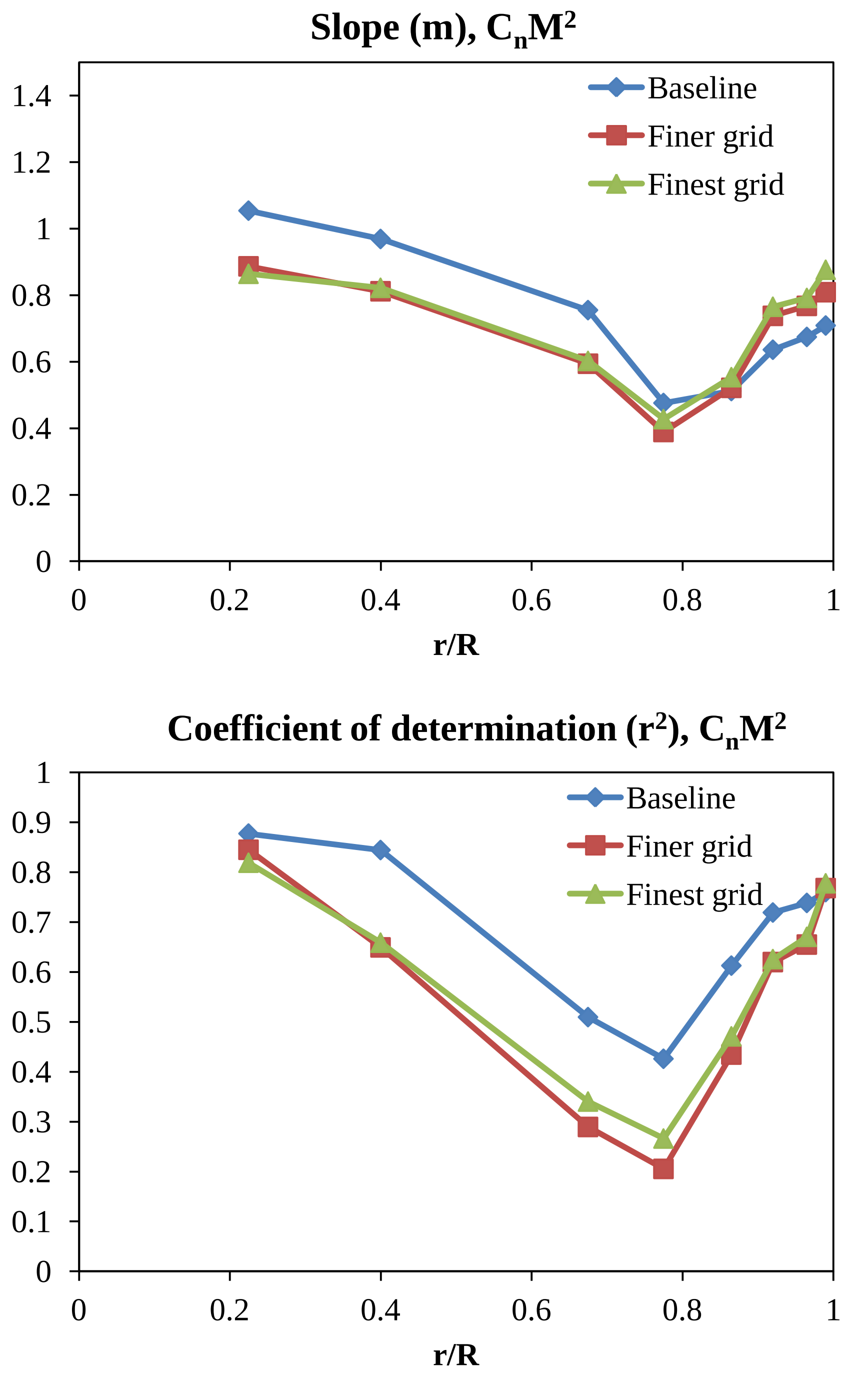

Figure 5.11 Quantitative assessment of grid sensitivity for sectional pitching moments as a function of radial station

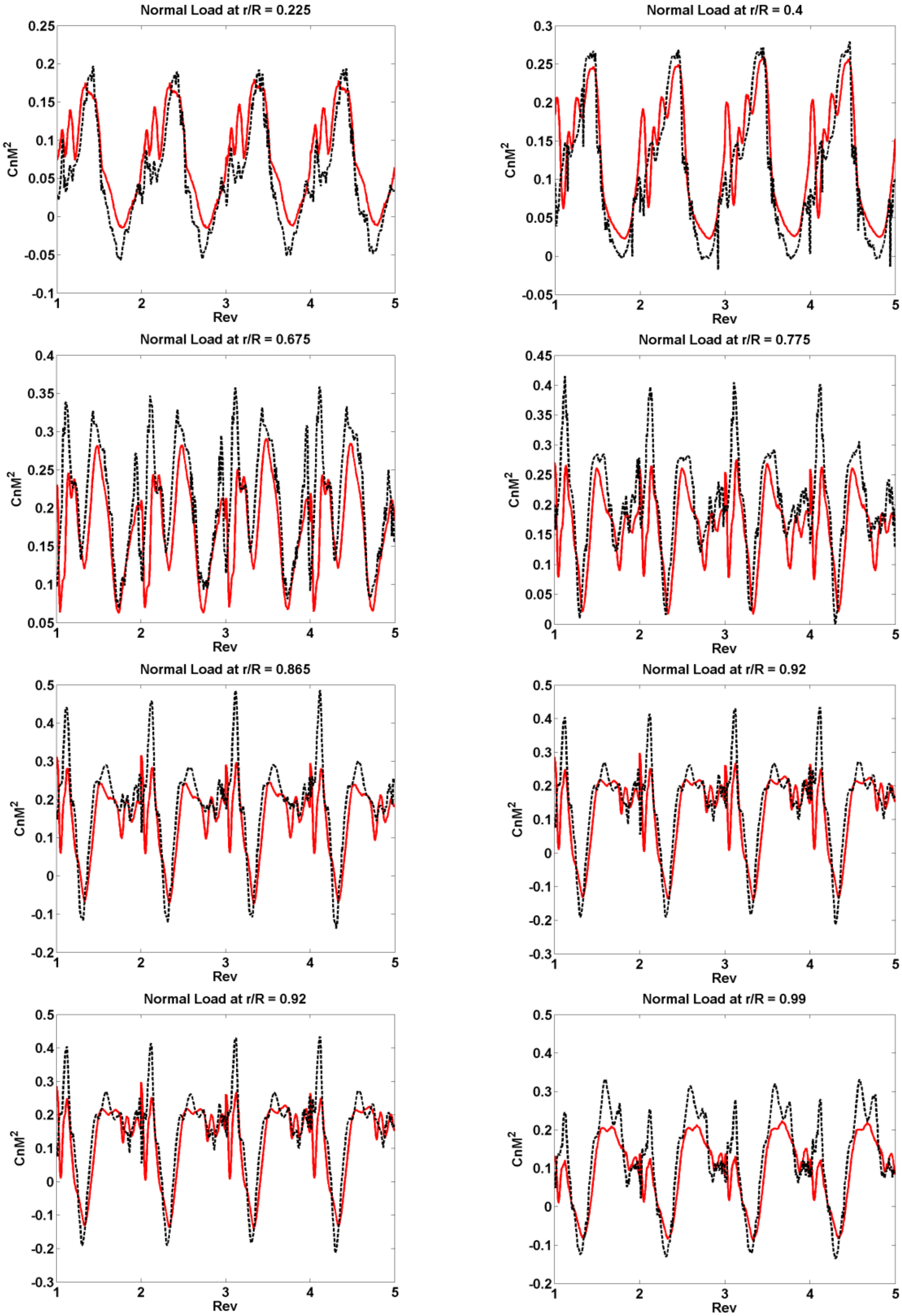

Figure 5.12 Representative non-dimensional sectional normal loads for Revs 2-5.

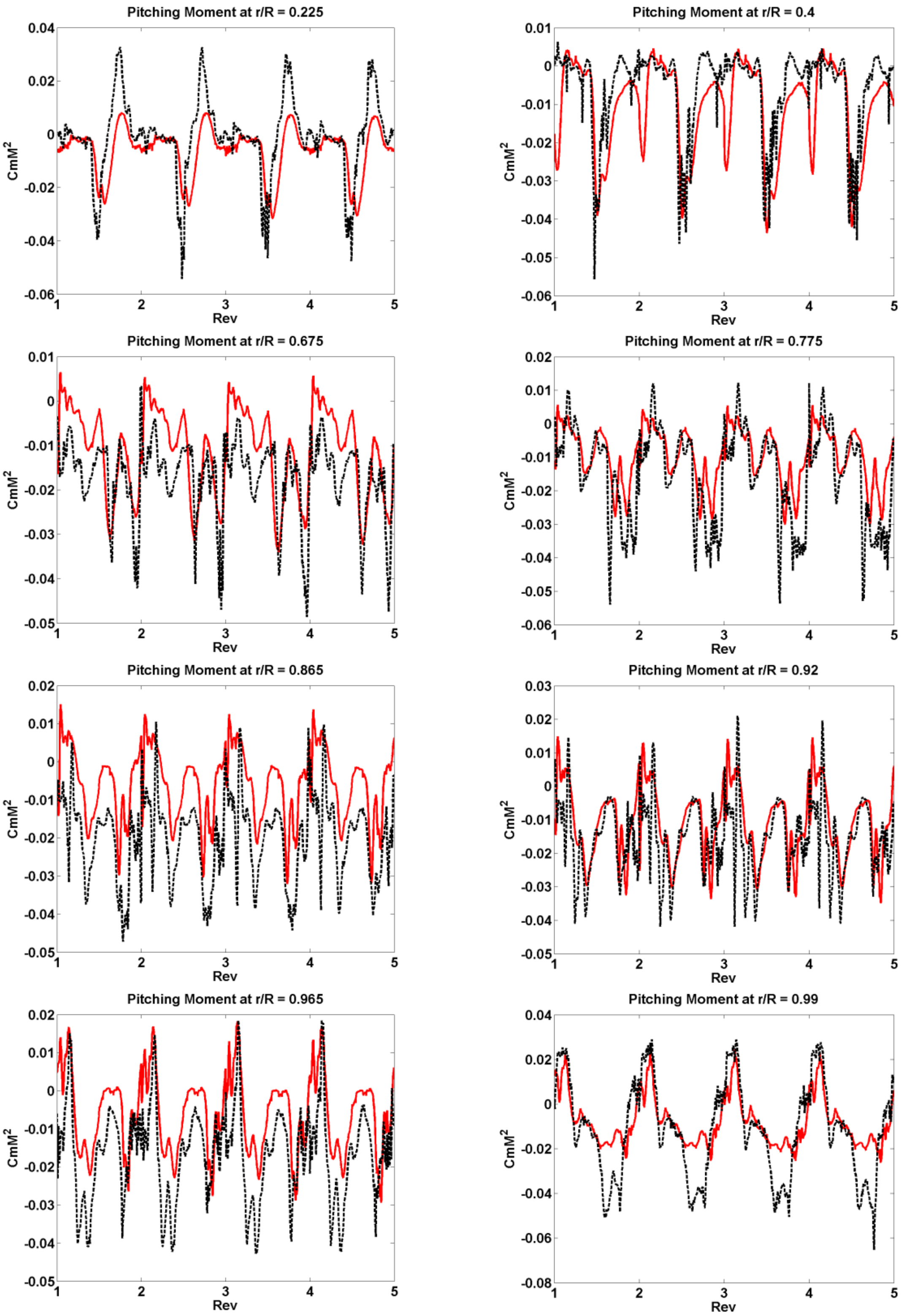

Figure 5.13 Representative non-dimensional pitching moments for Revs 2-5.

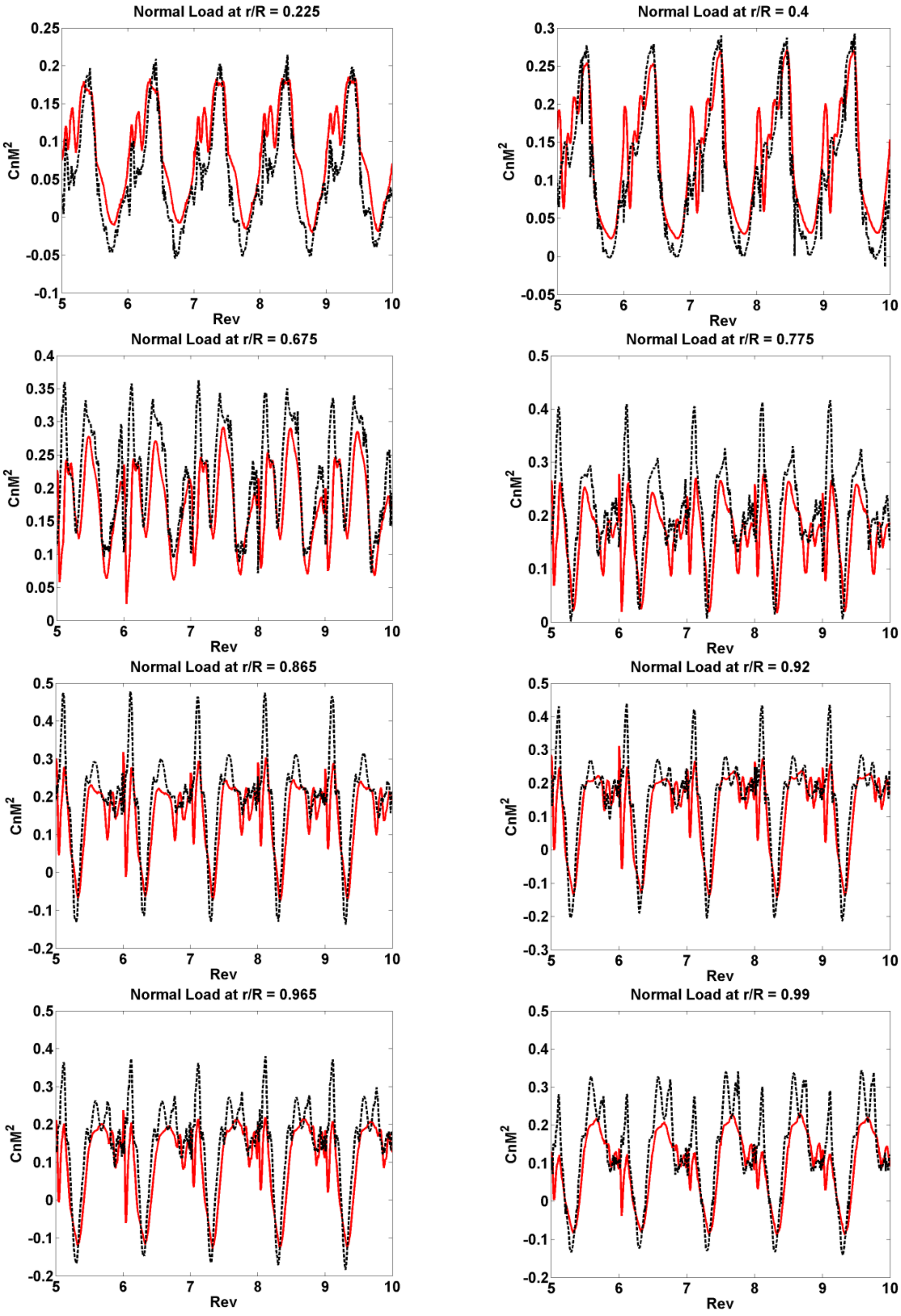

Figure 5.14 Representative non-dimensional sectional normal loads Revs 6-10.

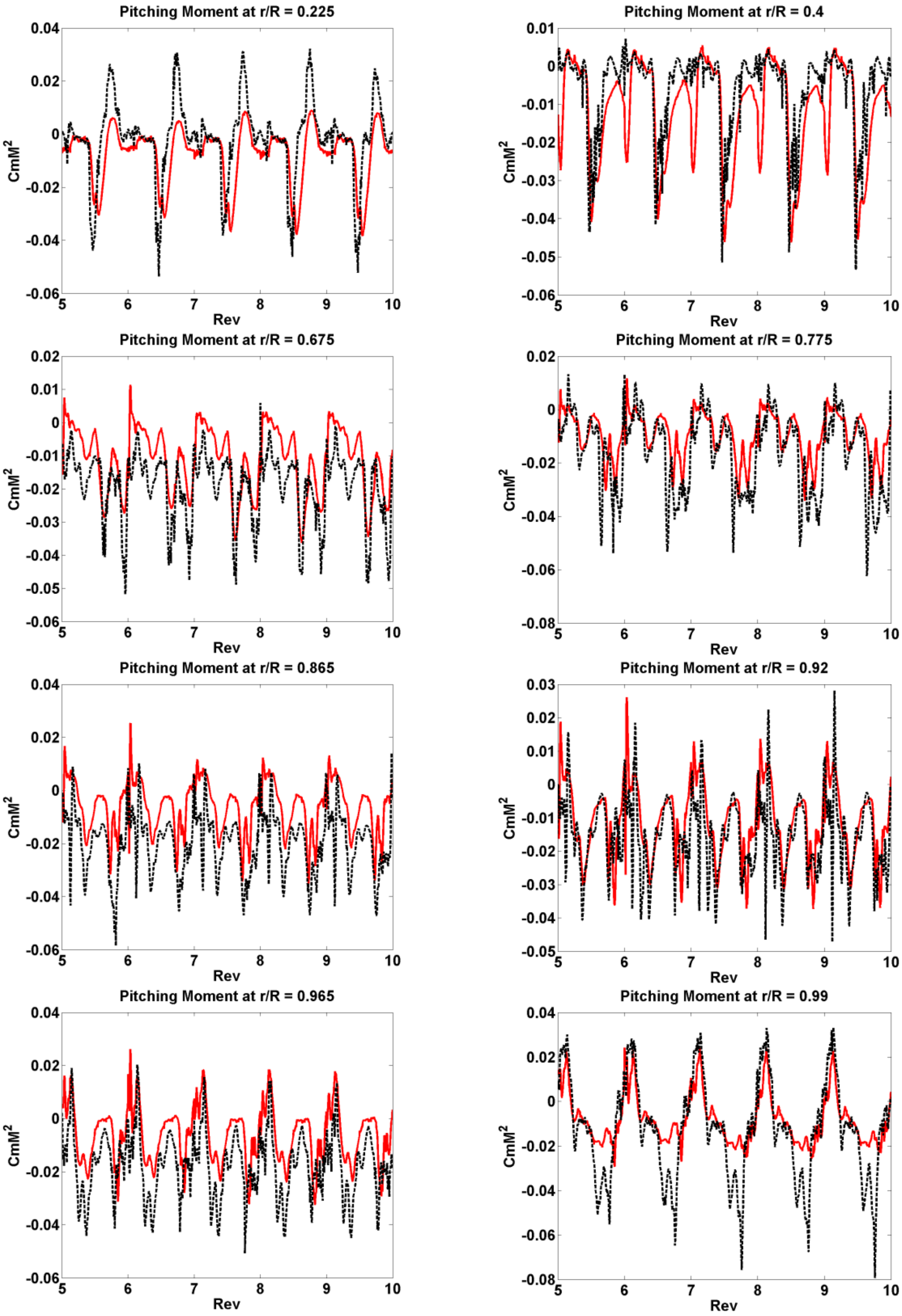

Figure 5.15 Representative non-dimensional pitching moments for Revs 6-10.

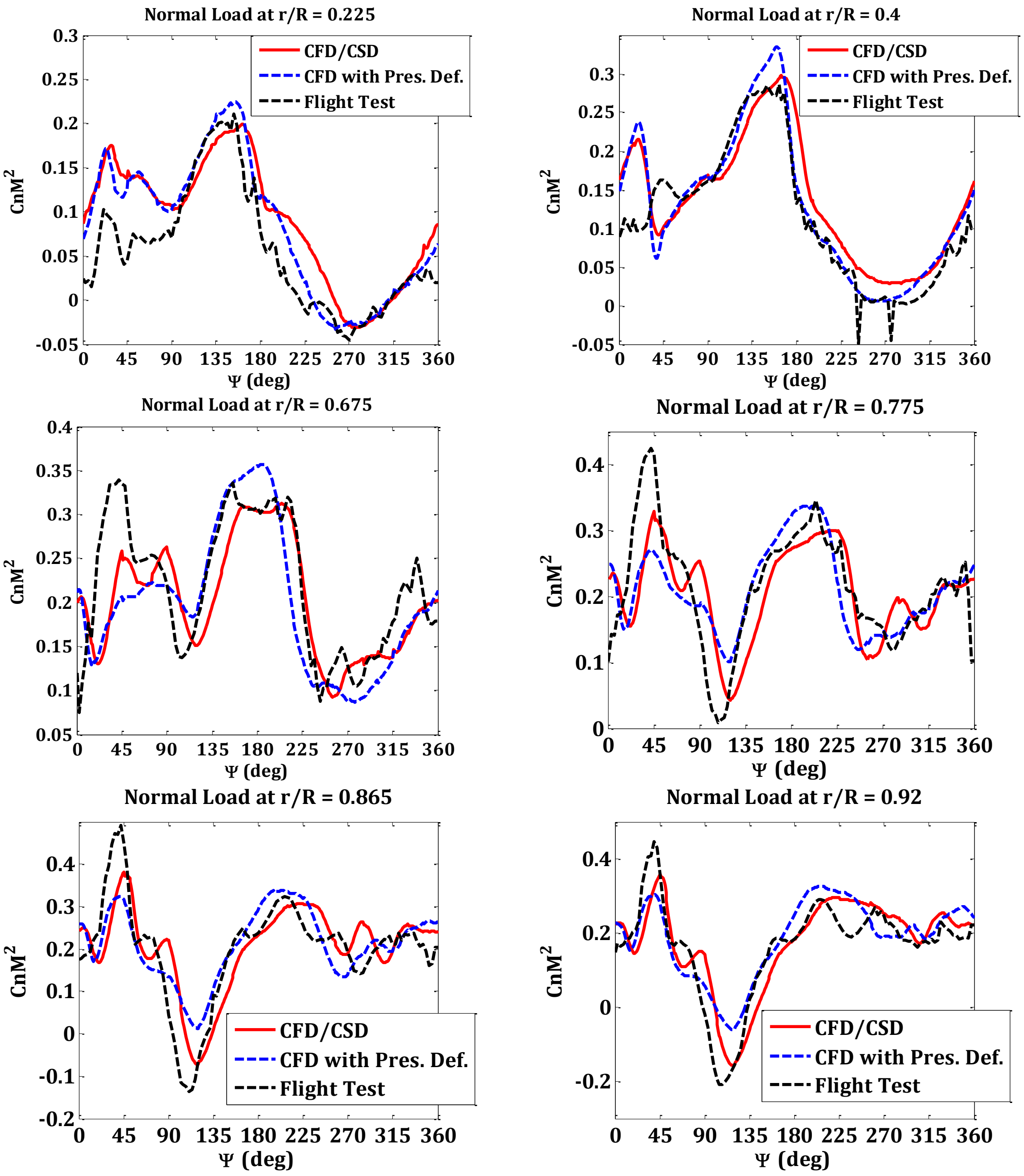

Normal Load at r/R = 0.225

Normal Load at r/R = 0.4

Normal Load at r/R = 0.675

Normal Load at r/R = 0.775

Normal Load at r/R = 0.865

Normal Load at r/R = 0.92

Figure 5.16 Representative non-dimensional sectional normal loads for Rev 12 at load factor of 1.7

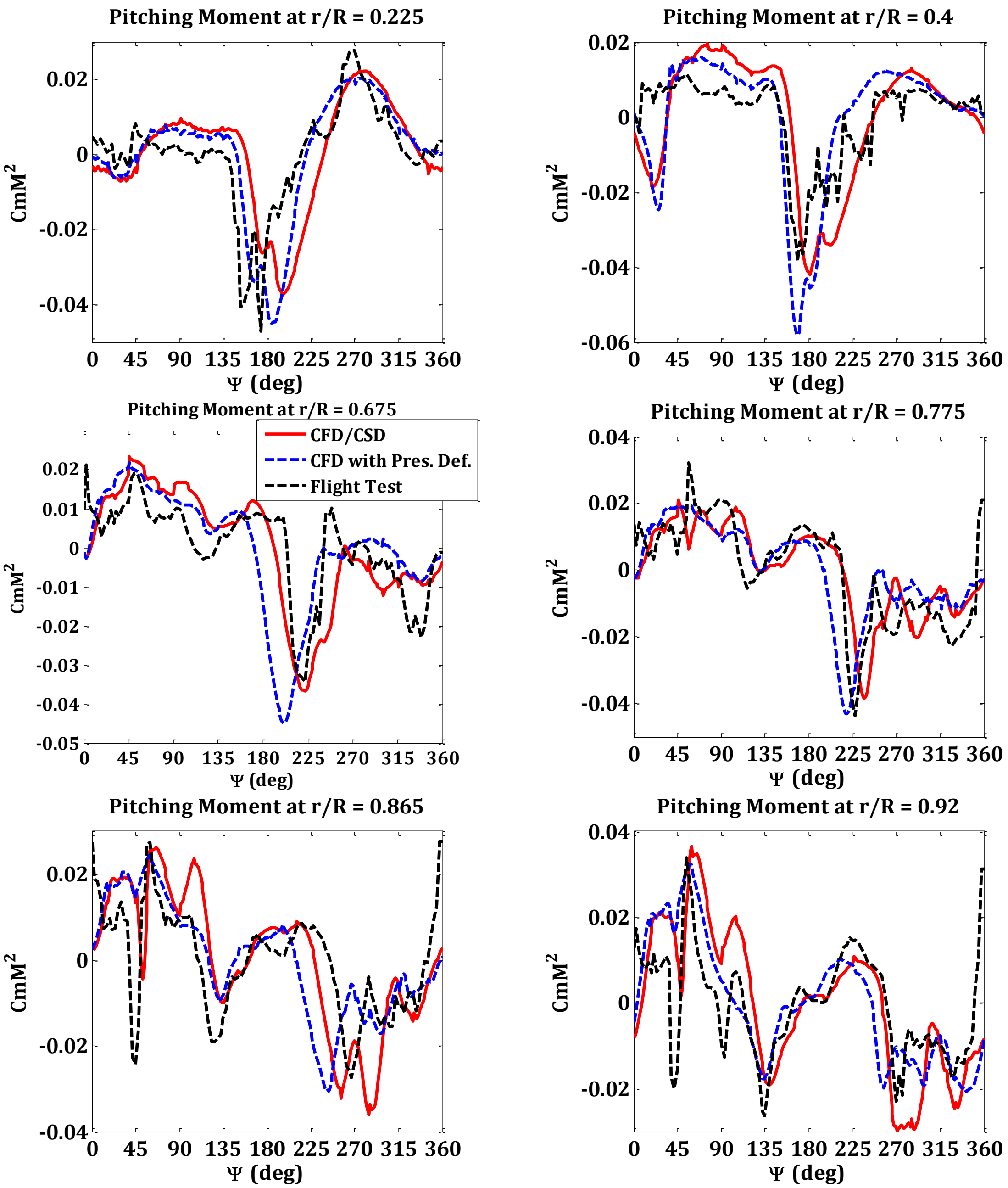

Figure 5.17 Representative non-dimensional sectional pitching moments for Rev 12 at load factor of 1.7.

Radial station (r/R)	CFD with prescribed deformations		CFD/CSD	
	Slope (*m*)	Coefficient of determination (r^2)	Slope (*m*)	Coefficient of determination (r^2)
0.225	0.9212	0.6169	0.6289	0.3404
0.4000	1.2586	0.6273	1.1346	0.5736
0.6750	0.6369	0.2439	0.9548	0.5774
0.7750	0.6408	0.5246	0.6608	0.6091
0.8650	0.4791	0.2146	0.7571	0.3674
0.9200	0.6713	0.3514	0.8075	0.3772
0.9650	0.8081	0.4774	0.8490	0.4772
0.9900	0.6716	0.7270	0.6161	0.7141

Table 5.2 Comparison of the prediction accuracy of sectional pitching moments using CFD with prescribed deformations vs. CFD/CSD

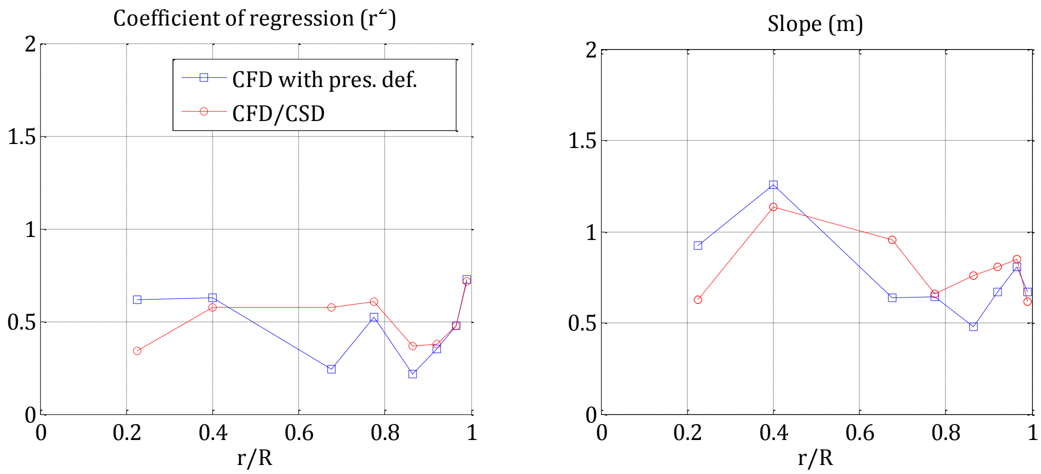

Figure 5.18 Slope and coefficient of determination as a function of radial location.

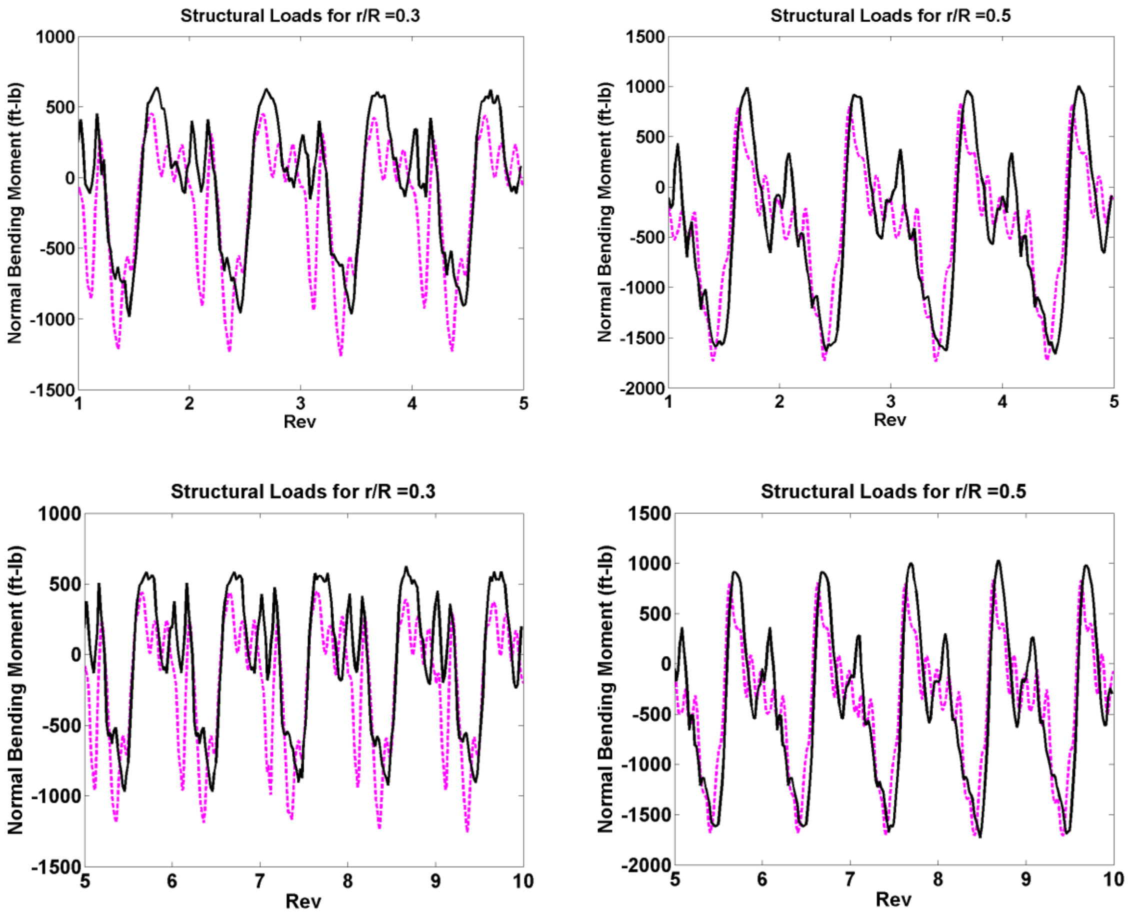

Figure 5.19 Blade sectional Normal Bending Moments at 30% and 50% R for Revs 1-10.

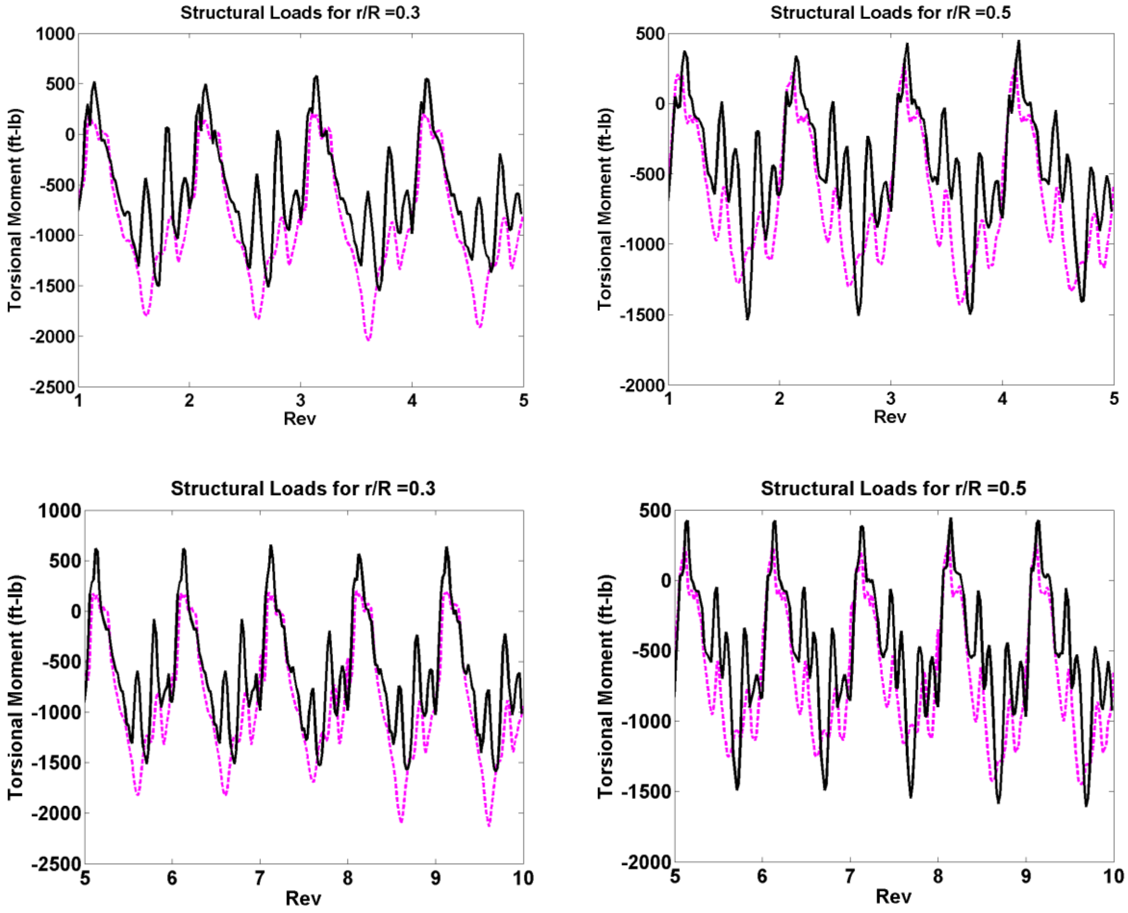

Figure 5.20 Blade sectional Torsional Moments at 30% and 50% R for Revs 1-10.

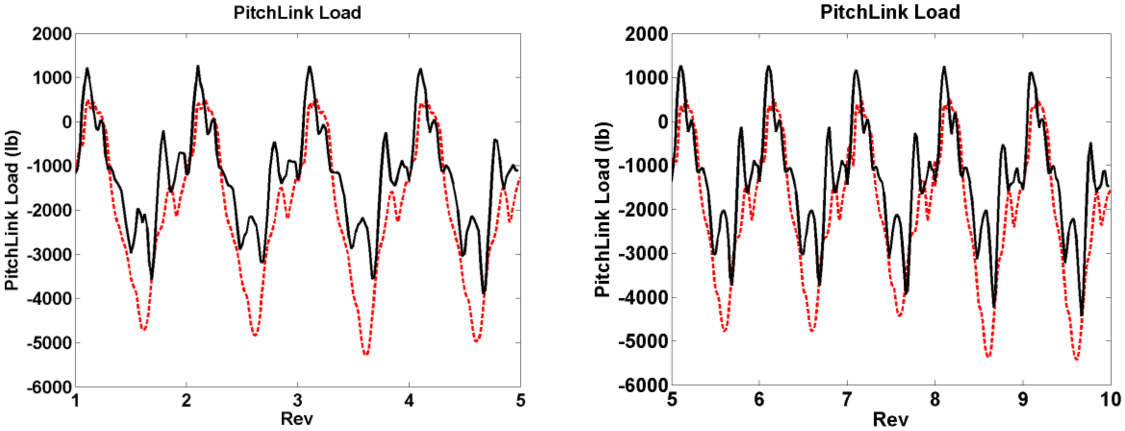

Figure 5.21 Pitchlink loads for the first 10 revolutions.

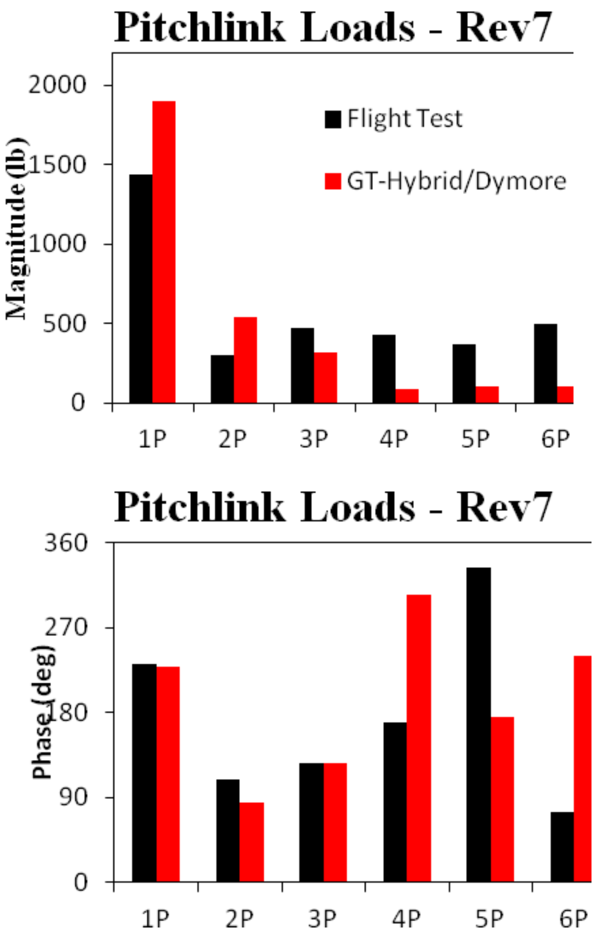

Figure 5.22 Harmonic content of pitchlink loads for a representative revolution, Rev 7.

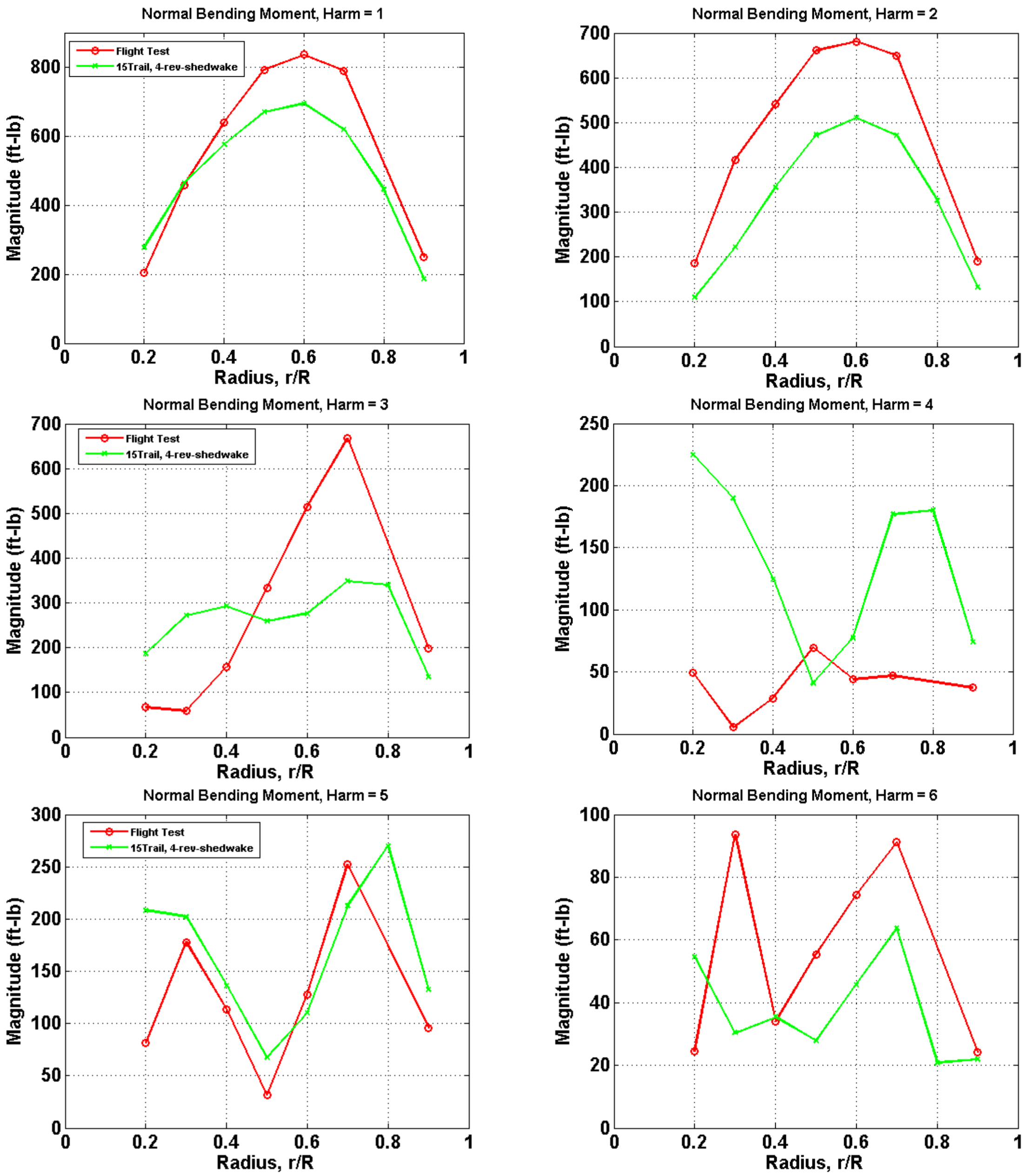

Figure 5.23 Harmonic content (magnitude) of normal bending moments for a representative revolution, Rev 7.

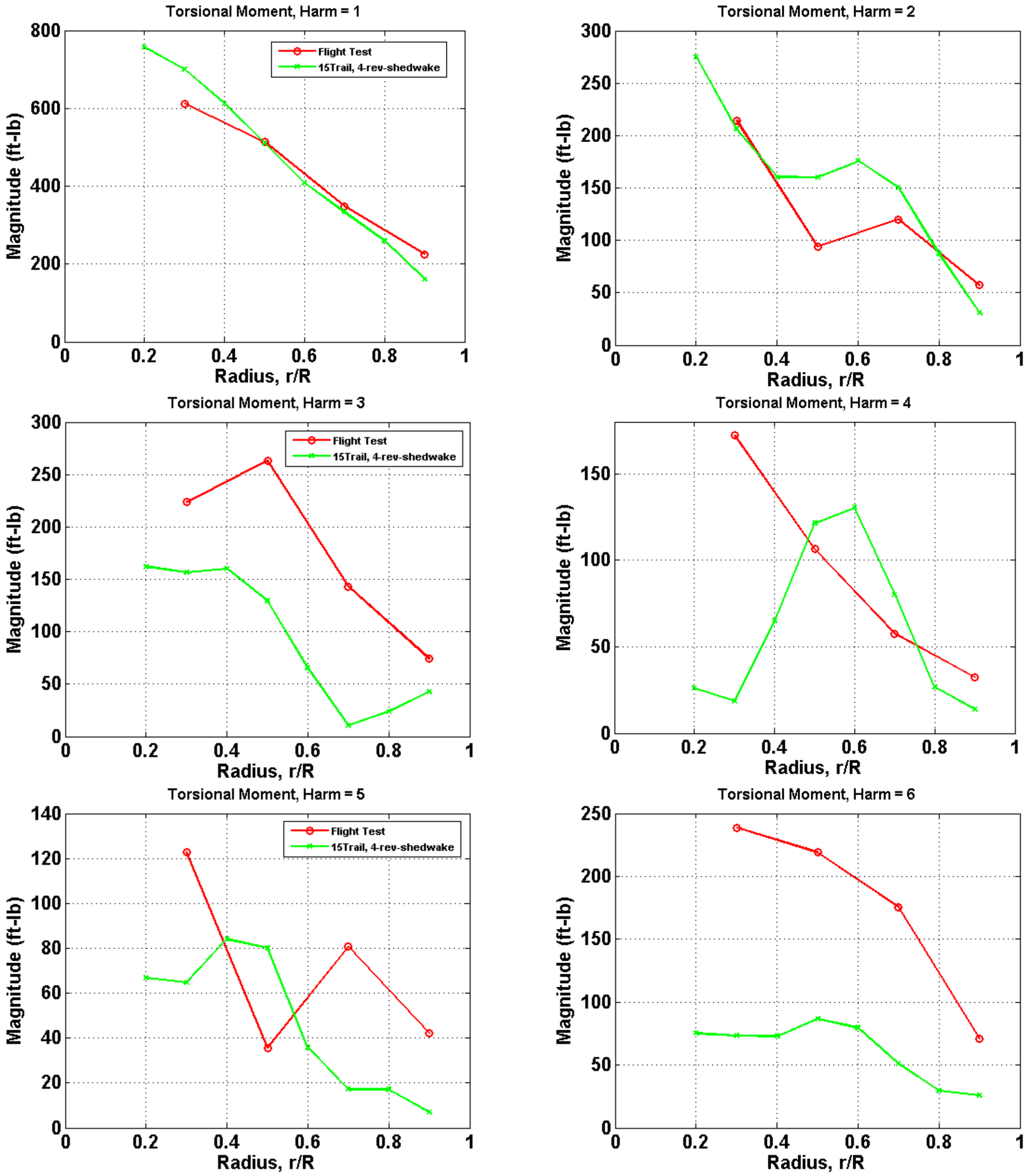

Figure 5.24 Harmonic content (magnitude) of torsional loads for a representative revolution, Rev 7

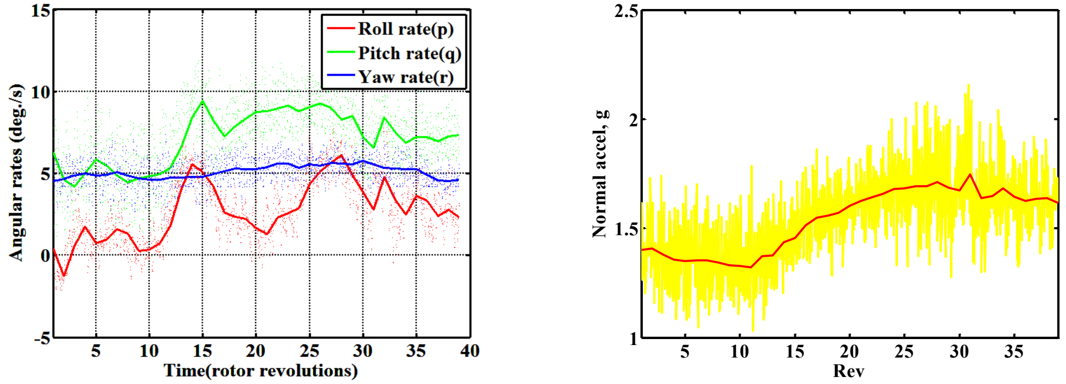

a. Angular rates b. Normal Load Factor

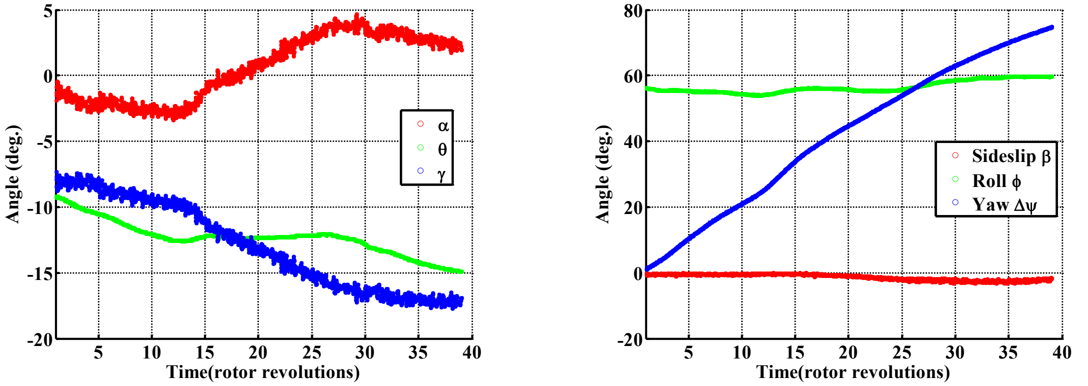

c. Angle of attack, pitch attitude, flight path angle d. Side slip angle, roll attitude, yaw attitude

Figure 5.25 Vehicle attitudes in the inertial frame, for 11679.

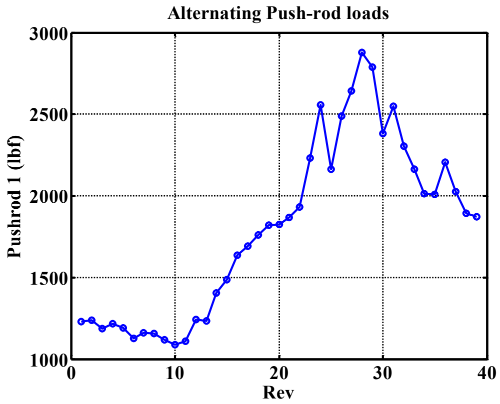

Figure 5.26 Alternating push-rod loads, for 11679.

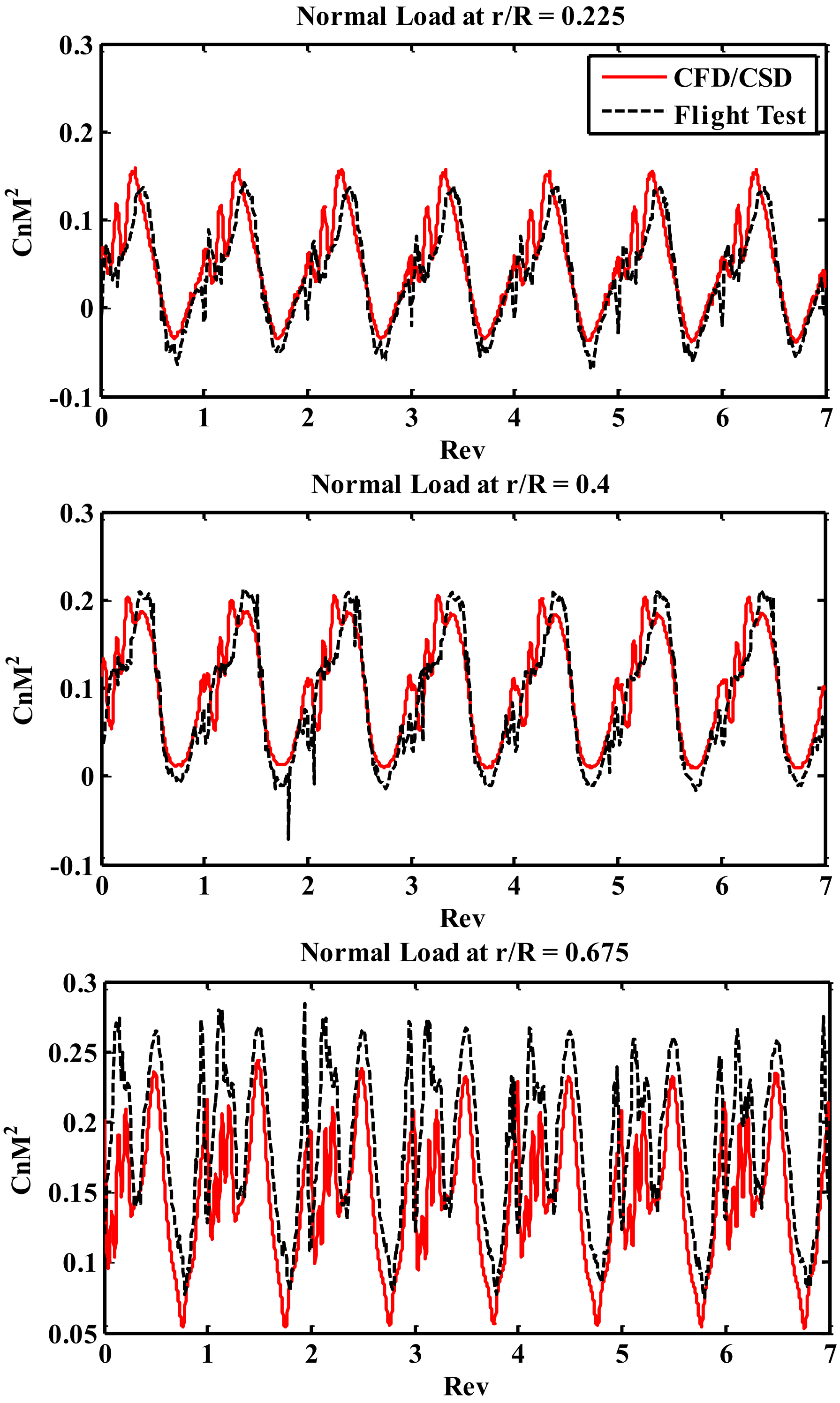

Figure 5.27 Sectional Normal Loads for Revs 1-7 of C11679, at 0.225R, 0.4R and 0.675R respectively.

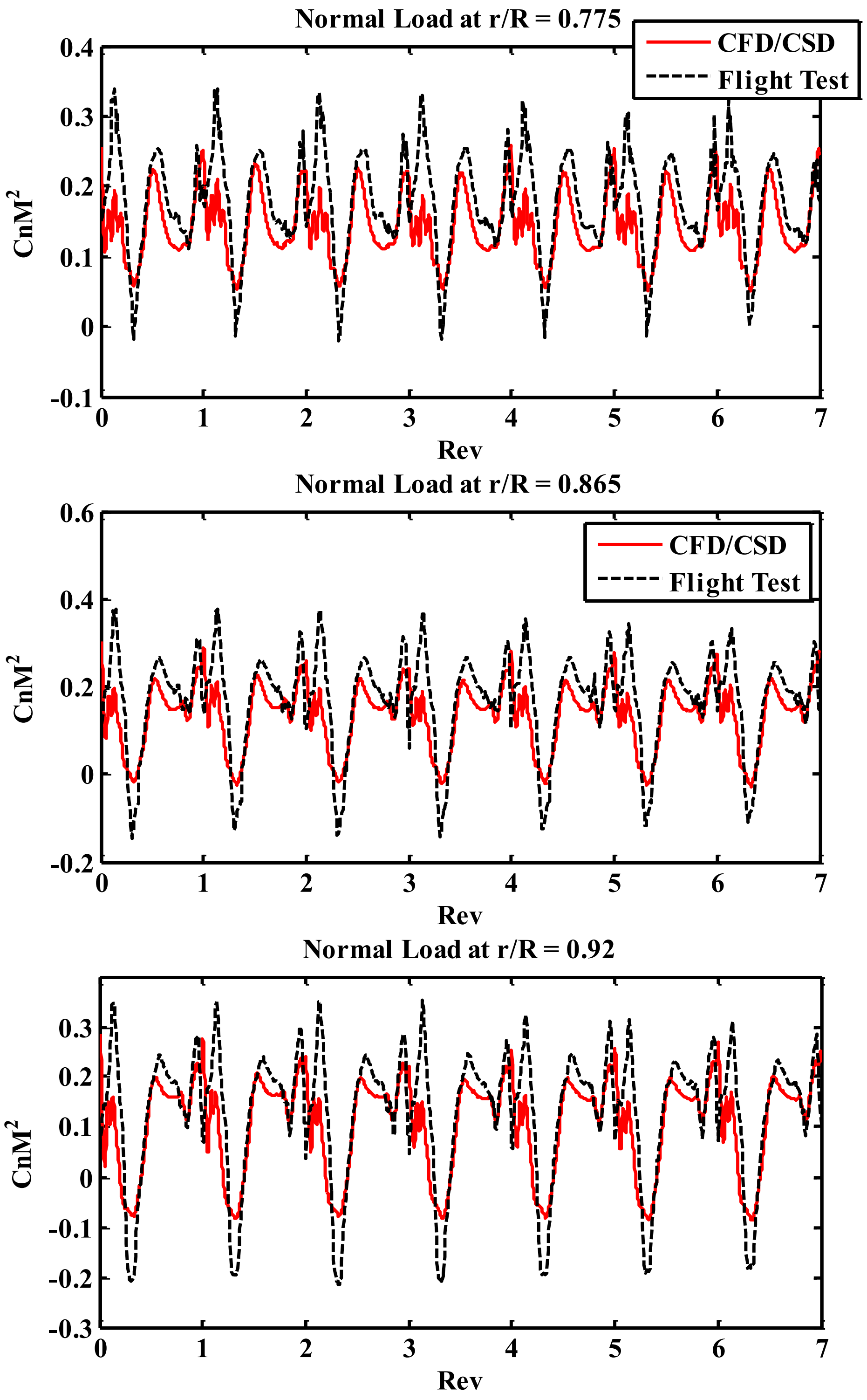

Figure 5.28 Sectional Normal Loads for Revs 1-7 of C11679, at 0.775R, 0.865R and 0.92R respectively.

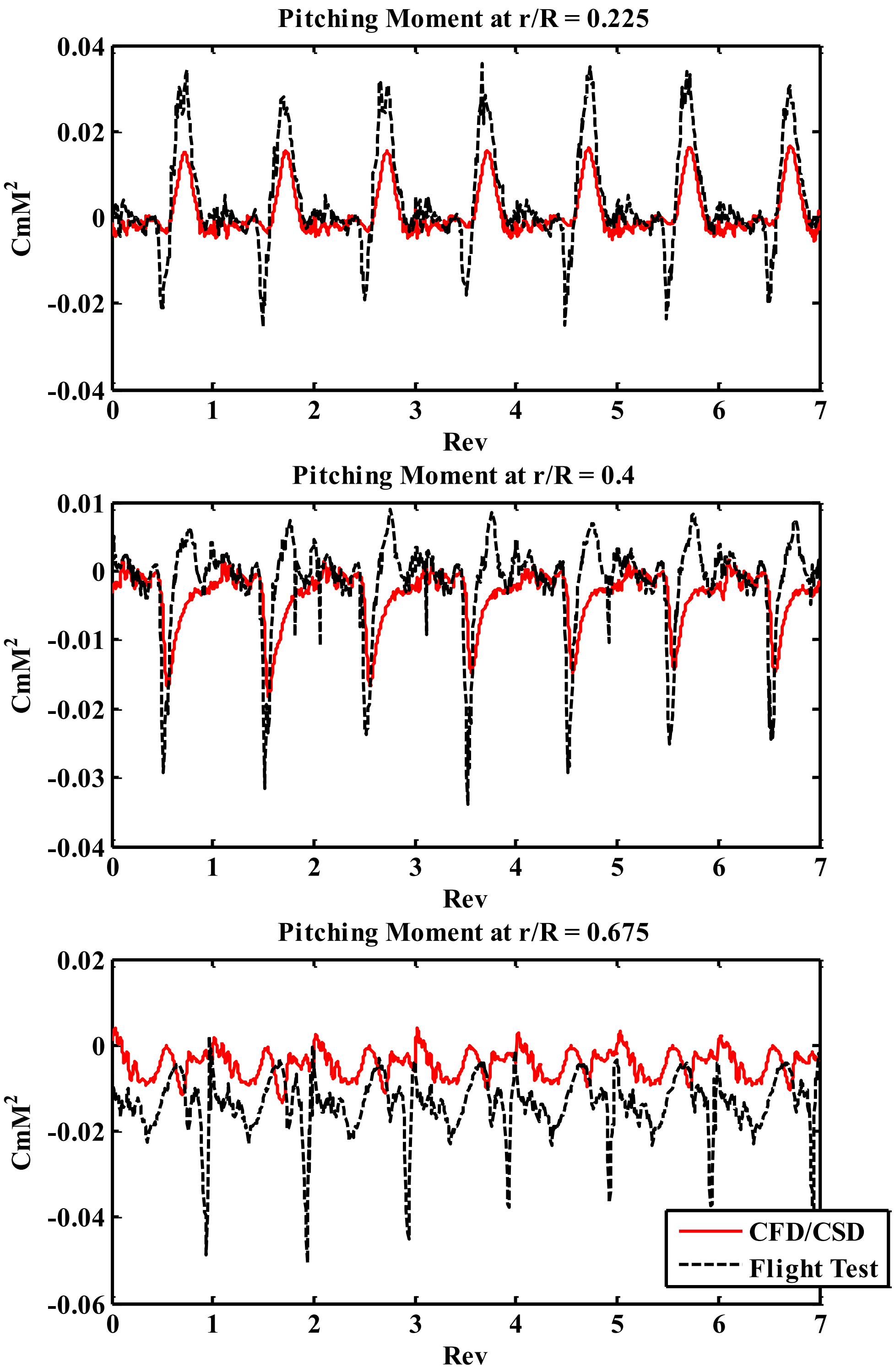

Figure 5.29 Sectional Pitching Moments for Revs 1-7 of C11679, at 0.225R, 0.4R and 0.675R respectively.

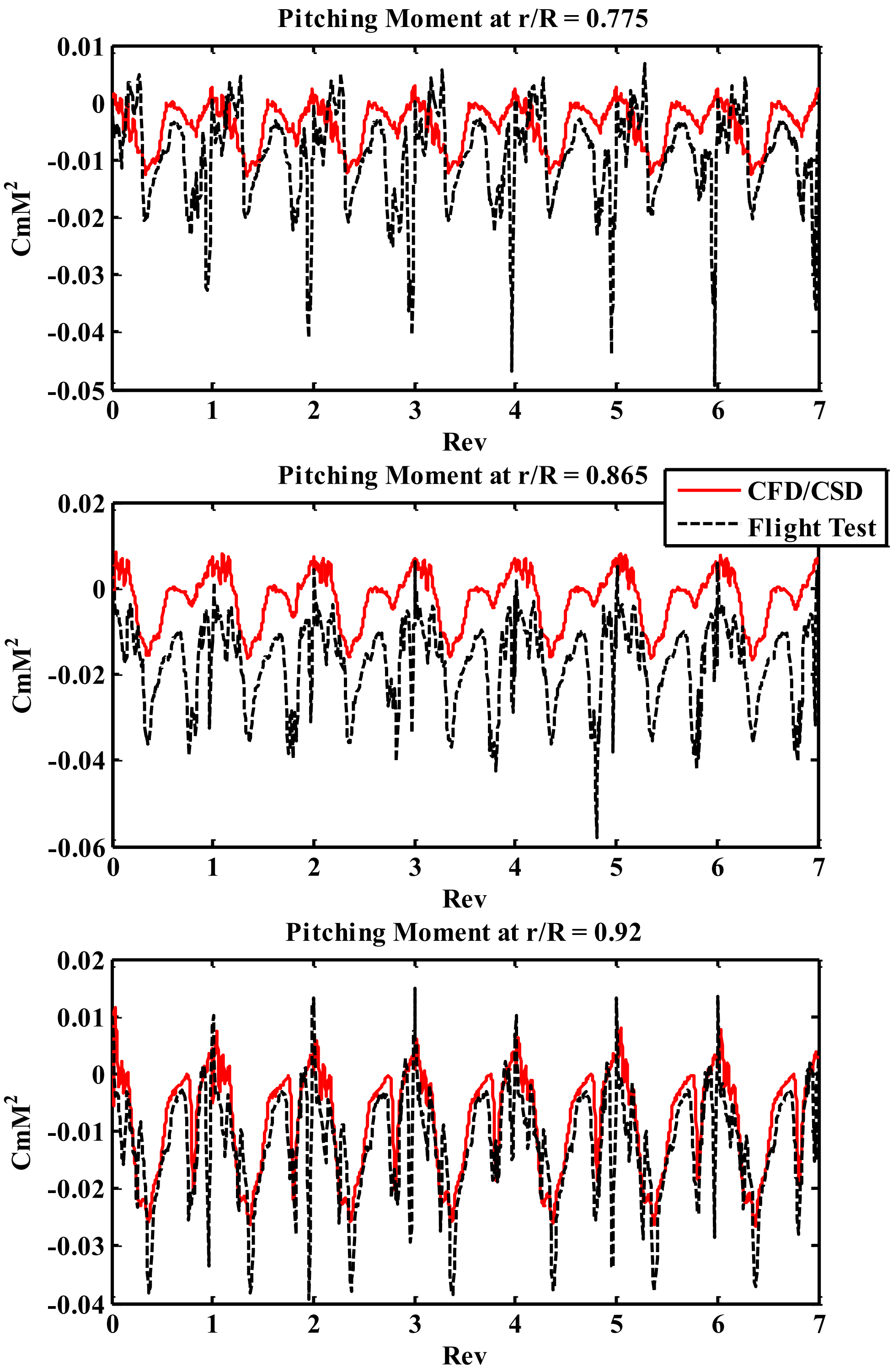

Figure 5.30 Sectional Pitching Moments for Revs 1-7 of C11679.

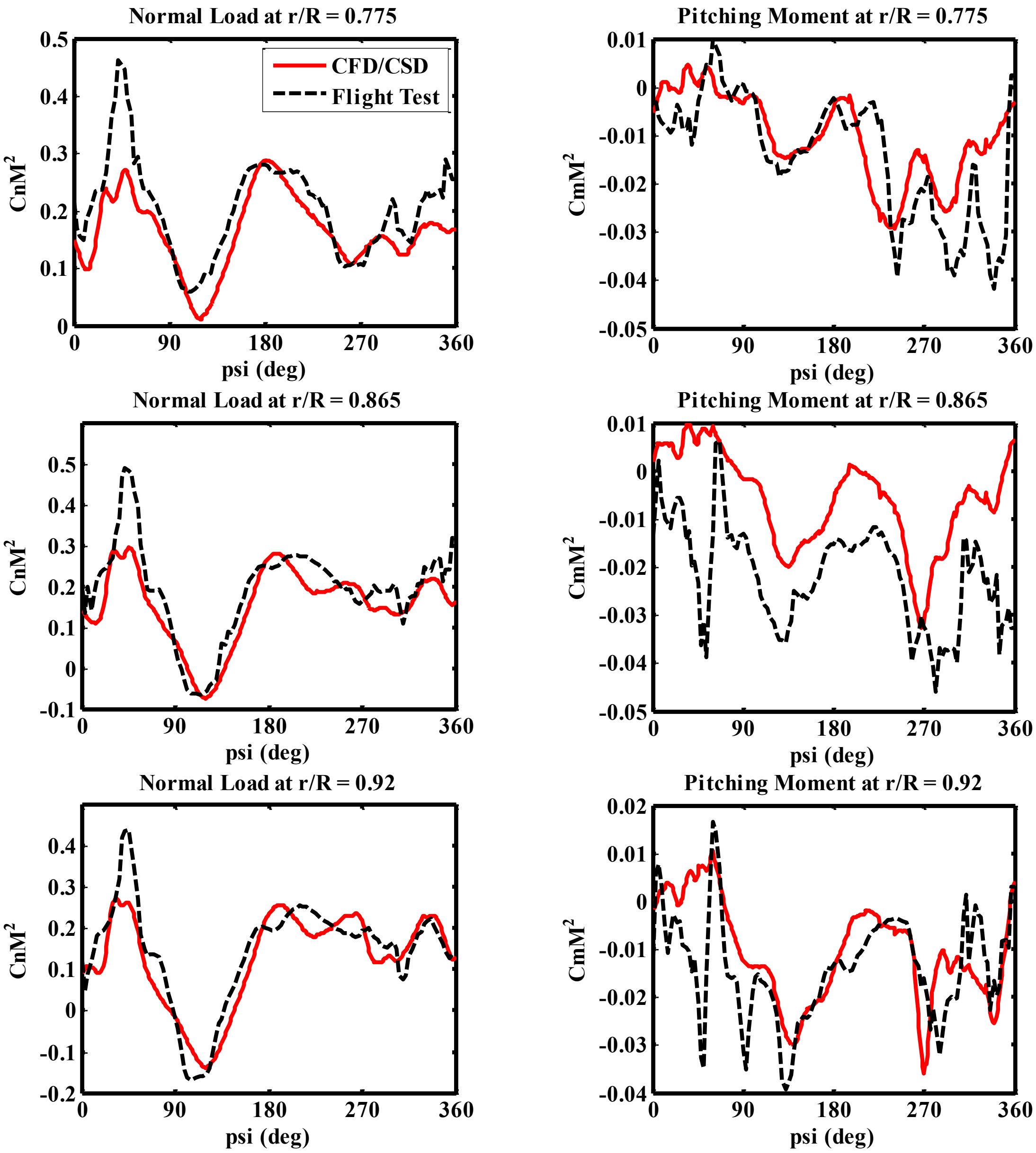

Figure 5.31 Sectional normal loads and pitching moments for Rev 20 characterized by normal load factor of 1.7, 11679

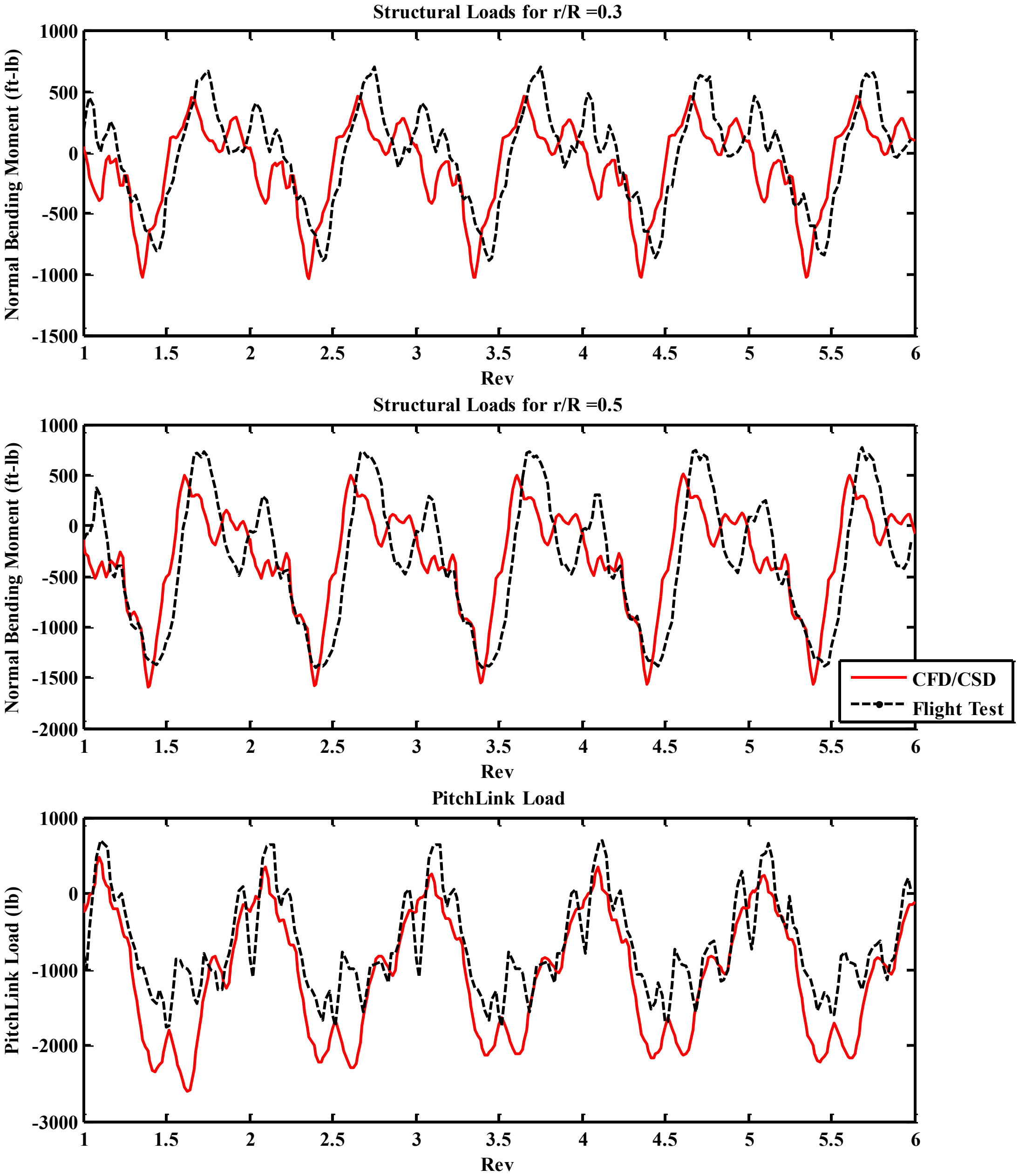

Figure 5.32 Blade structural loads for Revs 1-6 of C11679.

CHAPTER 6

CONCLUSIONS AND RECOMMENDATIONS

This research work forms a link in understanding the rotor behavior under a variety of flight conditions. In this research, a hybrid CFD methodology was coupled with a multi-body dynamics approach and extensively validated for a range of operating conditions for the UH-60A rotor. A series of speed sweep conditions ranging between blade-vortex interaction case to a compressible flow case, as well as thrust sweep conditions ranging between unstalled to deeply stalled cases were studied to understand the behavior of the rotor and determine performance characteristics.

The hybrid method is then extended to study the most severe maneuver recorded in the UH-60A flight test database. The current research work forms the first CFD/CSD study of the diving turn maneuvers (11679 and 11680) for the UH-60A rotor. CFD grid sensitivity and structural model validation studies were performed for to investigate this maneuver. The feasibility of a quasi-steady loosely coupled approach for predicting severe maneuver loads, was explored for efficiently and accurately predicting critical aerodynamic and aeroelastic phenomena.

6.1 Conclusions

Based on the studies performed, the following conclusions may be drawn:

1. The hybrid methodology in conjunction with the multibody dynamics code provide an economical means of modeling steady level flight as well as maneuvers.
2. The methodology is able to yield performance data such as C_T , C_P , C_H and L/D_e as a function of rotor operating conditions.

3. For the UH-60A rotor configuration, mildly BVI events occurring at advance ratio of 0.15 were captured by the multiple trailer wake model in conjunction with the shed wake. The blade loading is found to be significantly sensitive to wake model at low advance ratios.
4. All the key aerodynamic phenomena for low speed, high speed and high thrust conditions were predicted by the current analyses.
5. In the case of quasi-steady maneuvers studied in this work, the loose coupling approach was found to be adequate to model all the necessary physical phenomena.
6. The blade root motion and control settings for a speed sweep and thrust sweep were found to be in good agreement with the test data.
7. A 3rd stall event occurring in a region of super-critical flow is observed in the first quadrant at 92% radial location on the rotor blade, during rotor revolutions characterized by peak load factor of both Maneuvers 11679 and 11680. The current CFD/CSD methodology is able to capture this event.
8. The mean and the peak-to-peak structural loads occurring in Maneuvers 11679 and 11680 were well-predicted. However, the retreating blade wave-form was not captured well. Analysis using the mechanical airloads problem showed that the structural model will further need to be improved in order to capture the retreating side events.

6.2 Recommendations for Future Work

Based on the computational studies and conclusions, the following recommendations are made for future research:

1. Althouth 1P-3P structural loads are reasonably captured, the prediction of higher harmonic content continues to be a challenge.
2. Enhancements to the structural dynamics should include incorporation of accurate control system stiffness, modeling of swash plate dynamics and definitions of the hydraulic lag damper.
3. Maneuvering flight should be accurately simulated by incorporating the accelerations experienced by the rotor hub in the structural model.
4. Enhancements to the CFD model include incorporation of advanced turbulence and transition models and use of higher temporal and spatially accurate methods. The advancing side stall is hypothesized to be triggered due to moving shock and boundary layer interaction. This phenomena must be further investigated.
5. In the current implementation of the multiple trailer model, the spacing of the trailers is uniform, although their strength varies based on the changes in the local bound circulation. The effect of grid spacing and spacing of the trailers needs to be further assessed.
6. The shaft shank has been shown to cause high drag and power penalties at high advance ratios, which has not been modeled in the current research.
7. In the current work, all the vehicle dynamics data was taken from flight test data. A flight dynamics model of the vehicle should be coupled to the CFD and the CSD solvers.
8. There are several computational kernels in the current hybrid methodology which may be extended for GPU computation. The Biot-Savart law for induced velocity computation may be implemented using GPU.

9. Alternate methodologies for induced velocity computation such as the viscous vortex particle methods that rely on parallelization techniques such as the fast multi-pole methods should be implemented. This will make the current hybrid methodology a faster method.

APPENDIX A

QUANTITATIVE METRIC FOR ASSESSMENT OF ACCURACY

It is necessary for estimating the accuracy of analytical and predictive methods through quantitative correlation. A standardized approach to quantitative assessment of predictive accuracy of analytical methods in rotorcraft aeromechanics was proposed and documented by Bousman and Norman [113].

A linear regression curve-fit of the data points provides three quantitative attributes of the correlation quality – slope (m), coefficient of determination (r^2) and vertical axis offset (b). This metric can be used to study the improvement and degradation of the airloads prediction as a function of various parameters. As the correlation quality improves, the slope (m) and coefficient of determination (r^2) approach unity. Exact correlation is said to be obtained if all the calculated and measured points lie on a line with slope of unity. In this assessment approach, slopes greater than 1.0 are considered an over prediction and slopes less than 1.0 are an under prediction.

This approach is illustrated in Figure A-1. A plot of calculated and measured sectional normal aerodynamic loads (C_nM^2) for a low speed steady level flight condition ($\mu = 0.15$ and $C_T/\sigma = 0.09$) at a spanwise location of 92% along the blade is shown in Figure A-1. Linear regression of the correlation variables gives a value of 0.925 for the slope (m), 0.0096 for the intercept (b) and 0.8384 for the coefficient of determination (r^2). Thus, there is a fairly good agreement between the measurement and the predicted data. Figure A-1 includes a linear regression line shown as a solid green. The scatter is indicated by solid blue line ($\pm\sigma$) and provides the standard estimate of error. The scatter in this case is 1.4% (based on the ordinate scale), which is typical of better performance calculations.

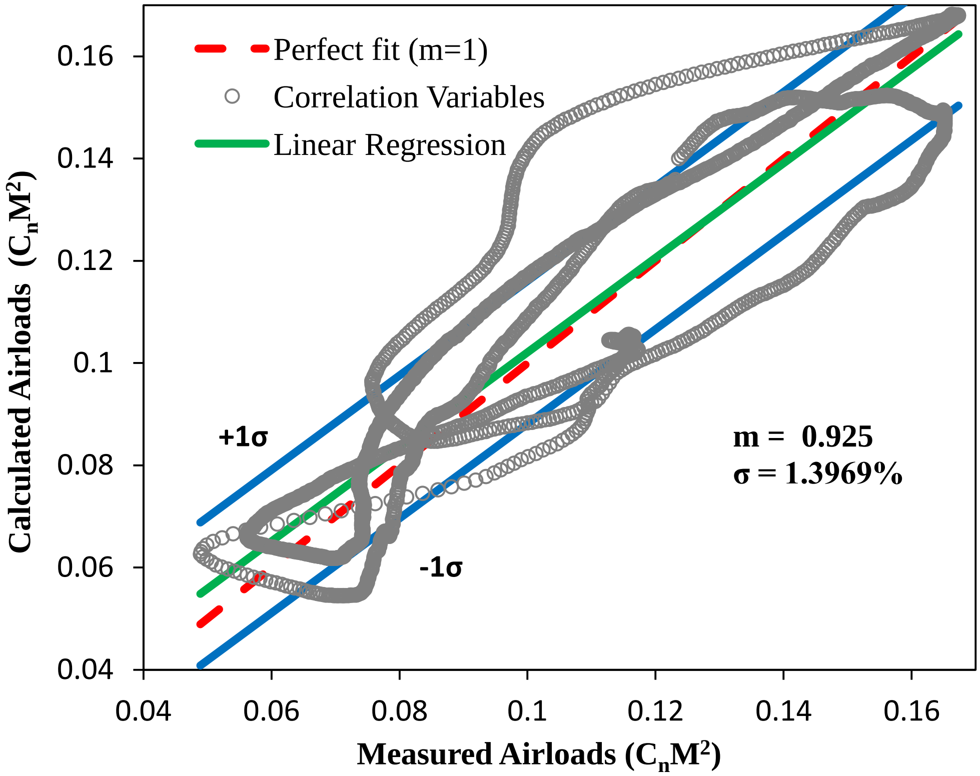

Figure A.1 Accuracy of sectional normal airloads predicted by GT-Hybrid/DYMORE2 (CFD/CSD) for UH-60A blade at a radial station of 92% at steady level flight condition with μ = 0.15 and $C_T/\sigma = 0.09$.

The predictive capability of sectional normal airloads for a high speed flight condition obtained using GT-Hybrid/DYMORE2 CFD/CSD analysis is plotted as a function of slope and coefficient of determination in Figure A-2. Quantitative assessment of accuracy of predicted normal loads for a high thrust condition at which dynamic stall occurs has also been plotted in Figure A-3. Inaccurate phase prediction manifests as increased scatter and reduced slope.

Thus, this methodology can be used to quantitatively assess the accuracy of predicted aeromechanical loads.

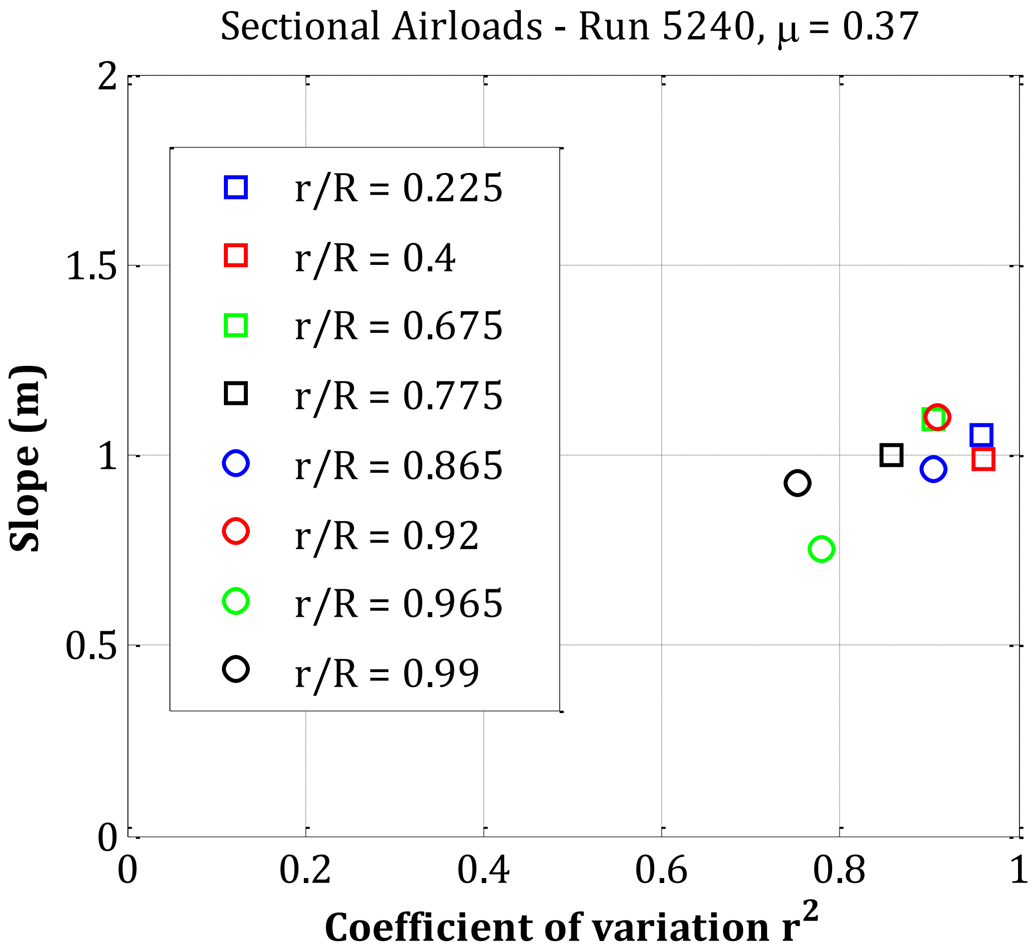

Figure A.2 Prediction quality of sectional normal airloads at different radial locations along the blade at a high speed steady level flight condition with μ = 0.37 and CT/σ = 0.09. Best correlation quality corresponds to m = 1 and r^2 = 1.

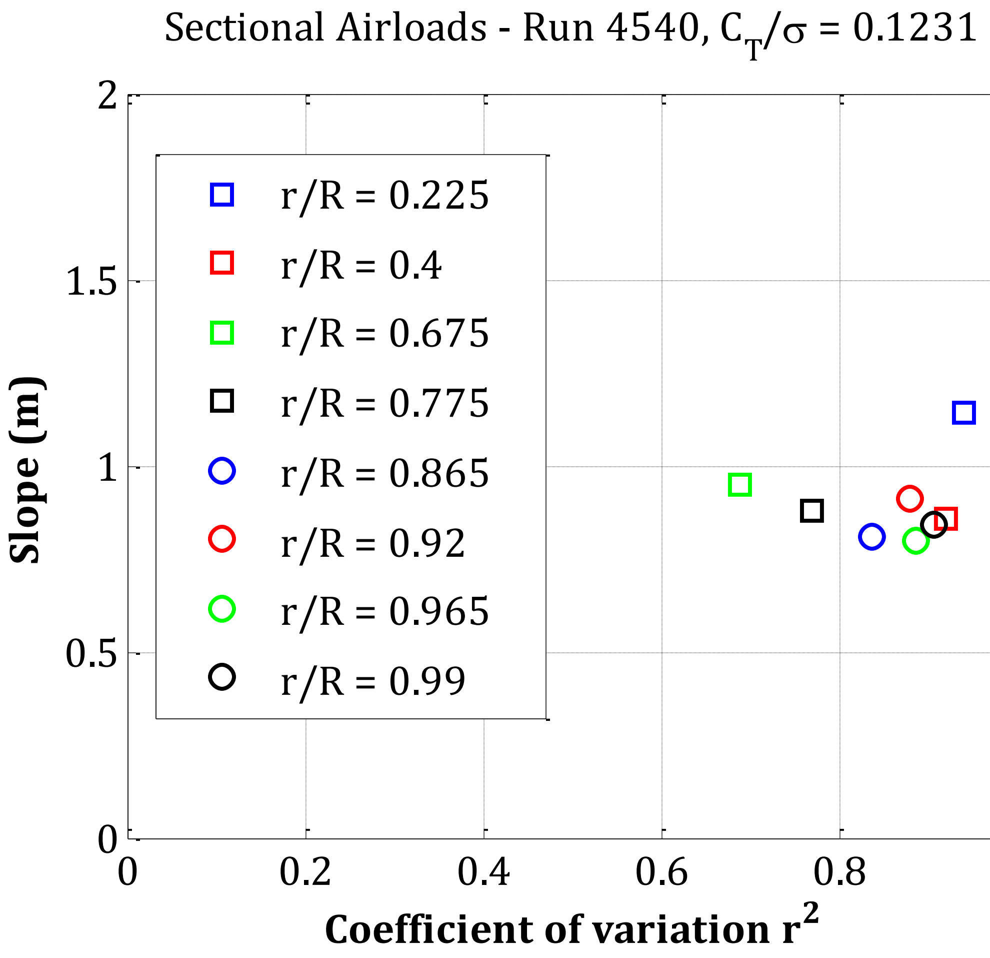

Figure A.3 Prediction quality of sectional normal airloads at different radial locations along the blade at a high thrust flight condition with μ = 0.3 and C_T/σ = 0.123. Best correlation quality corresponds to m = 1 and r^2 = 1.

REFERENCES

1. Scheiman, J. "A tabulation of helicopter rotor-blade differential pressures, stresses, and motions as measured in flight." National Aeronautics and Space Administration, Washington, DC, 1964.

2. Cross, J., and Watts, M. "Tip aerodynamics and acoustics test: A report and data survey," 1988.

3. Shockey, G. A., Williamson, J. W., and Cox, C. R. "AH-1G Helicopter Aerodynamic and Structural Loads Survey." DTIC Document, 1977.

4. Isaacs, N., and Harrison, R. "Identification of retreating blade stall mechanisms using flight test pressure measurements," *AHS, Annual Forum, 45th, Boston, MA*. 1989.

5. Caradonna, F., and Tung, C. "Experimental and analytical studies of a model helicopter rotor in hover," *Vertica* Vol. 5, No. 2, 1981, pp. 149-161.

6. Caradonna, F., Lautenschlager, J., and Silva, M. "An experimental study of rotor-vortex interactions," *AIAA, Aerospace Sciences Meeting, 26 th, Reno, NV*. 1988, p. 1988. doi:10.2514/6.1988-45

7. Dadone, L., Ekquist, D., Dawson, S., and Boxwell, D. "Model 360 rotor test at DNW- Review of performance and blade airload data," *American Helicopter Society-Annual Forum*. Vol. 43, American Helicopter Society, Inc., Saint Louis, MO, 1987, p. 1987.

8. Lorber, P. F. "Aerodynamic results of a pressure-instrumented model rotor test at the DNW," *Journal of the American Helicopter Society* Vol. 36, No. 4, 1991, pp. 66-76. doi: 10.4050/JAHS.36.66

9. Bousman, W. G., and Kufeld, R. M. *UH-60A airloads catalog*: National Aeronautics and Space Administration, Ames Research Center, 2005.

10. Kufeld, R. M., and Bousman, W. G. "High load conditions measured on a UH-60A in maneuvering flight," *Journal of the American Helicopter Society* Vol. 43, No. 3, 1998, pp. 202-211. http://dx.doi.org/10.4050/JAHS.43.202

11. Datta, A., and Chopra, I. "Validation and understanding of UH-60A vibratory loads in steady level flight," *Journal of the American Helicopter Society* Vol. 49, No. 3, 2004, pp. 271-287. http://dx.doi.org/10.4050/JAHS.49.271

12. Datta, A., and Chopra, I. "Prediction of UH-60A dynamic stall loads in high altitude level flight using CFD/CSD coupling," Annual Forum Proceedings-

American Helicopter Society, Vol. 61, American Helicopter Society, Inc., 2005, p. 117.

13. Datta, A., Sitaraman, J., Chopra, I., and Baeder, J. D. "CFD/CSD prediction of rotor vibratory loads in high-speed flight," *Journal of aircraft* Vol. 43, No. 6, 2006, pp. 1698-1709. doi: 10.2514/1.18915

14. Potsdam, M., Yeo, H., and Johnson, W. "Rotor airloads prediction using loose aerodynamic/structural coupling." DTIC Document, 2004.

15. Biedron, R. T., and Lee-Rausch, E. "An Examination of Unsteady Airloads on a UH-60A Rotor: Computation versus Measurement," 2012.

16. Bhagwat, M. J., Ormiston, R. A., Saberi, H. A., and Xin, H. "Application of CFD/CSD coupling for analysis of rotorcraft airloads and blade loads in maneuvering flight," *Annual Forum Proceedings-American Helicopter Society*. Vol. 63, American Helicopter Society, Inc., 2007, p. 2048.

17. Rajmohan, N. "Application of hybrid methodology to rotors in steady and maneuvering flight," *School of Aerospace Engineering*. Georgia Institute of Technology, Atlanta, GA, 2010.

18. Rajmohan, N., Sankar, L. N., and Costello, M. "Effect of inflow model on coupling between aeromechanics and flight mechanics," *AIAA Aerospace Sciences Meeting*. Vol. 49, American Institute of Aeronautics and Astronautics, Orlando, FL, 2011. doi: 10.2514/6.2011-1192

19. Rajmohan, N., Marpu, R., Sankar, L. N., Baeder, J. D., and Egolf, T. A. "Improved prediction of rotor maneuvering loads using a hybrid methodology," *Annual Forum Proceedings-American Helicopter Society*. Vol. 67, 2011.

20. Rajmohan, N., Manivannan, V., Sankar, L. N., Costello, M., and Bauchau, O. A. "Development of a Methodology for coupling rotorcraft aeromechanics and vehicle dynamics to study helicopters in maneuvering flight," *Annual Forum Proceedings-American Helicopter Society*. Vol. 65, American Helicopter Society, Inc., 2009.

21. Marpu, R., Sankar, L. N., Makinen, S., Baeder, J. D., Egolf, T. A., and Wasikowski, M. "Physics based modeling of maneuver loads for rotor and hub design," *American Helicopter Society Specialist's Design Conference*. American Helicopter Society, Inc., San Fransisco, 2012.

22. Marpu, R., Sankar, L. N., Makinen, S., and Baeder, J. D. "Computational Modeling of Diving Turn Maneuvers using Hybrid Methodology," *Annual Forum Proceedings-American Helicopter Society*. Vol. 68, American Helicopter Society, Inc., Fort Worth, TX, 2012.

23. Norman, T. R., Shinoda, P., Peterson, R., and Datta, A. "Full-Scale Wind Tunnel Test of The UH-60A Airloads Rotor," *Annual Forum Proceedings-American Helicopter Society*. Vol. 67, American Helicopter Society, Inc., Virginia Beach, VA, 2011, pp. 3-5.

24. Romander, E., Norman, T. R., and Chang, I.-C. "Correlating CFD simulation with wind tunnel test for the full-scale UH-60A airloads rotor," *Annual Forum Proceedings-American Helicopter Society*. Vol. 67, American Helicopter Society, Inc., Virginia Beach, VA, 2011.

25. Datta, A., Yeo, H., and Norman, T. R. "Experimental investigation and fundamental understanding of a slowed UH-60A rotor at high advance ratios," *Annual Forum Proceedings-American Helicopter Society*. Vol. 67, American Helicopter Society, Inc., Virginia beach, VA, 2011.

26. Yeo, H., and Romander, E. A. "Loads Correlation of a Full-Scale UH-60A Airloads Rotor in a Wind Tunnel," *Annual Forum Proceedings-American Helicopter Society*. Vol. 68, American Helicopter Society, Inc., Fort Worth, TX, 2012.

27. Marpu, R., Sankar, L. N., Norman, T., Egolf, T. A., and Makinen, S. "Analysis of the UH-60A Rotor Loads Using Wind Tunnel Data," *51st AIAA Aerospace Sciences Meeting including the New Horizons Forum and Aerospace Exposition*. American Institute of Aeronautics and Astronautics, 2013. doi: 10.2514/6.2013-635

28. Chang, I.-C., Norman, T., and Romander, E. "Airloads Correlation of the UH-60A Rotor inside the 40- by 80-Foot Wind Tunnel," *51st AIAA Aerospace Sciences Meeting including the New Horizons Forum and Aerospace Exposition*. American Institute of Aeronautics and Astronautics, 2013. doi: 10.2514/6.2013-636

29. Leishman, J., and Beddoes, T. "A semi-empirical model for dynamic stall," *Journal of the American Helicopter Society* Vol. 34, No. 3, 1989, pp. 3-17. doi: http://dx.doi.org/10.4050/JAHS.34.3

30. Johnson, W. "Development of a Comprehensive Analysis for Rotorcraft. 1. Rotor Model and Wake Analysis," *Vertica* Vol. 5, No. 2, 1981, pp. 99-129.

31. Stephens, W. B., Rutkowski, M. J., Ormiston, R. A., and Tan, C. M. "Development of the second generation comprehensive helicopter analysis system (2GCHAS)," *American Helicopter Society National Specialists' Meeting on Rotorcraft Dynamics*. Arlington, TX, 1989.

32. Rutkowski, M. J., Ruzicka, G. C., Ormiston, R. A., Saberi, H., and Jung, Y. "Comprehensive aeromechanics analysis of complex rotorcraft using 2GCHAS," *Journal of the American Helicopter Society* Vol. 40, No. 4, 1995, pp. 3-17. doi: http://dx.doi.org/10.4050/JAHS.40.3

33. Sopher, R., and Hallock, D. W. "Time-history analysis for rotorcraft dynamics based on a component approach," *Journal of the American Helicopter Society* Vol. 31, No. 1, 1986, pp. 43-51. doi: http://dx.doi.org/10.4050/JAHS.31.43

34. Bir, G., Chopra, I., and Nguyen, K. "Development of UMARC(University of Maryland Advanced Rotorcraft Code)," *AHS, Annual Forum, 46 th, Washington, DC*. 1990, pp. 55-78.

35. Johnson, W. "A history of rotorcraft comprehensive analyses," Ames Research Center, Moffett Field, CA, 2012.

36. Johnson, W. "Rotorcraft dynamics models for a comprehensive analysis," *Annual Forum Proceedings-American Helicopter Society*, Vol. 54, American Helicopter Society, 1998, pp. 452-471.

37. Saberi, H., Khoshlahjeh, M., Ormiston, R. A., and Rutkowski, M. J. "Overview of RCAS and application to advanced rotorcraft problems," *American Helicopter Society 4th Decennial Specialists' Conference on Aeromechanics, San Francisco, CA*. 2004.

38. Bauchau, O. A. "Computational schemes for flexible, nonlinear multi-body systems," *Multibody System Dynamics* Vol. 2, No. 2, 1998, pp. 169-225. doi: 10.1016/S0895-7177(00)00303-4

39. Abhishek, A., Datta, A., and Chopra, I. "Prediction of UH-60A structural loads using multibody analysis and swashplate dynamics," *Journal of Aircraft* Vol. 46, No. 2, 2009, p. 474. doi: 10.2514/1.35076

40. Bauchau, O. A., and Kang, N. "A multibody formulation for helicopter structural dynamic analysis," *Journal of the American Helicopter Society* Vol. 38, No. 2, 1993, pp. 3-14. http://dx.doi.org/10.4050/JAHS.38.3

41. Bauchau, O. A., Bottasso, C. L., and Nikishkov, Y. G. "Modeling rotorcraft dynamics with finite element multibody procedures," *Mathematical and Computer Modelling* Vol. 33, No. 10, 2001, pp. 1113-1137. http://dx.doi.org/10.1016/S0895-7177(00)00303-4

42. Hodges, D. H. "Geometrically Exact, Intrinsic Theory for Dynamics of Curved and Twisted Anisotropic Beams," *AIAA Journal* Vol. 41, No. 6, 2003, pp. 1131-1137. doi: 10.2514/2.2054

43. Hodges, D. H., and Yu, W. "A rigorous, engineer-friendly approach for modelling realistic, composite rotor blades," *Wind Energy* Vol. 10, No. 2, 2007, pp. 179-193. doi: 10.1002/we.215

44. Yu, W., Volovoi, V. V., Hodges, D. H., and Hong, X. "Validation of the variational asymptotic beam sectional analysis (VABS)," *AIAA Journal* Vol. 40, No. 10, 2002, pp. 2105-2113. doi: 10.2514/6.2001-1530

45. Gray, R. B. "On the Motion of the Helical Vortex Shed From a Single-Bladed Hovering Model Helicopter Rotor and its Application to the Calculation of the Spanwise Aerodynamic Loading." DTIC Document, 1955.

46. Landgrebe, A. J. "The wake geometry of a hovering helicopter rotor and its influence on rotor performance," *Journal of the American Helicopter Society* Vol. 17, No. 4, 1972, pp. 3-15. http://dx.doi.org/10.4050/JAHS.17.3

47. Scully, M. "Computation of helicopter rotor wake geometry and its influence on rotor harmonic airloads," *Department of Aeronautics and Astronautics*. PhD Thesis, Massachusetts Institute of Technology, 1975.

48. Summa, J. M. "Potential flow about three-dimensional lifting configurations, with application to wings and rotors," *13th Aerospace Sciences Meeting*. American Institute of Aeronautics and Astronautics, 1975. doi: 10.2514/6.1975-126

49. Caradonna, F. X., and Isom, M. P. "Subsonic and transonic potential flow over helicopter rotor blades," *AIAA Journal* Vol. 10, No. 12, 1972. doi: 10.2514/6.1972-39

50. Chang, I.-C. *Transonic flow analysis for rotors*: National Aeronautics and Space Administration, Scientific and Technical Information Branch, 1984.

51. Chang, I.-C. "Unsteady Euler solution of transonic helicopter rotor flow," *National Specialists' Meeting on Aerodynamics and Aeroacoustics, Arlington, TX*. 1987, p. 1987.

52. Egolf, T. A., and Sparks, S. P. "A full potential rotor analysis with wake influence using an inner-outer domain technique," *Journal of the American Helicopter Society* Vol. 32, No. 3, 1987, pp. 15-24. http://dx.doi.org/10.4050/JAHS.32.15

53. Sankar, L. N., and Prichard, D. "Solution of transonic flow past rotor blades using the conservative full potential equation," *AIAA Paper 85-5012*, 1985. doi: 10.2514/6.1985-5012

54. Sankar, L. N., and Malone, J. B. "Unsteady transonic full potential solutions for airfoils encountering vortices and gusts," *American Institute of Aeronautics and*

Astronautics, Fluid Dynamics and Plasmadynamics and Lasers Conference, 18th, Cincinnati, OH. 1985, p. 1985. doi: 10.2514/6.1985-1710

55. Sankar, L. N., Wake, B. E., and Lekoudis, S. G. "Solution of the unsteady Euler equations for fixed and rotor wing configurations," *Journal of Aircraft* Vol. 23, 1986, pp. 283-289. doi: 10.2514/3.45301

56. Agarwal, R., and Deese, J. "Euler calculations for flowfield of a helicopter rotor in hover," *Journal of Aircraft* Vol. 24, No. 4, 1987, pp. 231-238. doi: 10.2514/6.1986-1782

57. Hassan, A., Tung, C., and Sankar, L. "An assessment of full potential and Euler solutions for self-generated rotor blade-vortex interactions," *AHS, Annual Forum, 46 th, Washington, DC*. 1990, pp. 771-784.

58. Sankar, L., and Tung, C. "Euler calculations for rotor configurations in unsteady forward flight," *American Helicopter Society-Annual Forum Proceedings*. Vol. 42, Washington, DC, 1986, pp. 985-995.

59. Strawn, R. C., and Barth, T. J. "A finite-volume Euler solver for computing rotary-wing aerodynamics on unstructured meshes," *Journal of the American Helicopter Society* Vol. 38, No. 2, 1993, pp. 61-67. http://dx.doi.org/10.4050/JAHS.38.61

60. Srinivasan, G. R., and McCroskey, W. J. "Navier-Stokes calculations of hovering rotor flowfields," *Journal of Aircraft* Vol. 25, No. 10, 1988, pp. 865-874. doi: 10.2514/3.45673

61. Wake, B. E., and Sankar, L. N. "Solutions of the Navier-Stokes equations for the flow about a rotor blade," *Journal of the American Helicopter Society* Vol. 34, No. 2, 1989, pp. 13-23. doi: http://dx.doi.org/10.4050/JAHS.34.13

62. Wake, B. E. "Solution procedure for the Navier-Stokes equations applied to rotors," *School of Aerospace Engineering*. PhD Thesis, Georgia Institute of Technology, Atlanta, GA, 1987.

63. Srinivasan, G. R., Baeder, J. D., Obayashi, S., and McCroskey, W. J. "Flowfield of a lifting rotor in hover - A Navier-Stokes simulation," *AIAA Journal* Vol. 30, No. 10, 1992, pp. 2371-2378. doi: 10.2514/3.11236

64. Srinivasan, G. R., and Baeder, J. D. "TURNS: A Free-Wake Euler/Navier-Stokes Numerical Method for Helicopter Rotors," *AIAA Journal* Vol. 31, No. 5, 1993, pp. 959-962. doi: 10.2514/3.49036

65. Chen, C., McCroskey, W., and Obayashi, S. "Numerical solutions of forward-flight rotor flow using an upwind method," *Journal of Aircraft* Vol. 28, No. 6, 1991, pp. 374-380. doi: 10.2514/6.1989-1846

66. Bangalore, A. K. "Computational fluid dynamic studies of high lift rotor systems using distributed computing," *School of Aerospace Engineering*. Georgia Institute of Technology, Atlanta, 1995.

67. Steinhoff, J., Yonghu, W., Mersch, T., and Senge, H. "Computational vorticity capturing - Application to helicopter rotor flows," *AIAA, Aerospace Sciences Meeting and Exhibit, 30th, Reno, NV*. 1992, p. 1992. doi: 10.2514/6.1992-56

68. Wang, C., Bridgeman, J., Steinhoff, J., and Wenren, Y. "The application of computational vorticity confinement to helicopter rotor and body flows," *Annual Forum Proceedings-American Helicopter Society*. Vol. 49, American Helicopter Society, Inc., 1993, pp. 557-557.

69. Nichols, R. H., Tramel, R. W., and Buning, P. "Solver and turbulence model upgrades to OVERFLOW 2 for unsteady and high-speed applications," *24 th AIAA Applied Aerodynamics Conference*. 2006. doi: 10.2514/6.2006-2824

70. Chan, W. M., Meakin, R. L., and Potsdam, M. A. "CHSSI Software for Geometrically Complex Unsteady Aerodynamic Applications," *15 th AIAA Computational Fluid Dynamics Conference, Anaheim, CA, United States*. Vol. 11, 2001. doi: 10.2514/6.2001-593

71. Sankaran, V., Sitaraman, J., Wissink, A., Datta, A., Jayaraman, B., Potsdam, M., Mavriplis, D., Yang, Z., O'Brien, D., and Saberi, H. "Application of the helios computational platform to rotorcraft flowfields," *48th AIAA Aerospace Sciences Meeting*. Vol. 1230, American Institute of Aeronautics and Astronautics, Orlando, FL, 2010. doi: 10.2514/6.2010-1230

72. Altmikus, A., Wagner, S., Beaumier, P., and Servera, G. "A comparison- Weak versus strong modular coupling for trimmed aeroelastic rotor simulations," *AHS International, 58th Annual Forum Proceedings*. Vol. 1, 2002, pp. 697-710.

73. Bauchau, O., and Ahmad, J. "Advanced CFD and CSD methods for multidisciplinary applications in rotorcraft problems," *AIAA, NASA, & ISSMO, Symposium on Multidisciplinary Analysis and Optimization,(Bellevue, WA)*. 1996. doi: 10.2514/6.1996-4151

74. Pomin, H., and Wagner, S. "Navier-Stokes analysis of helicopter rotor aerodynamics in hover and forward flight," *AIAA Paper* Vol. 998, 2001. doi: 10.2514/6.2001-998

75. Sitaraman, J. "CFD based unsteady aerodynamic modeling for rotor aeroelastic analysis," *Department of Aerospace Engineering*. PhD Thesis, University of Maryland, College Park, MD, 2003.

76. Phanse, S., Sankar, L. N., and Charles, B. "Efficient coupled fluid structure interaction approach for analysis of rotors in forward flight," *American Helicopter Society Vertical Lift Aircraft Design Conference*. American Helicopter Society, Inc., San Francisco, CA, 2006.

77. Potsdam, M., Yeo, H., and Johnson, W. "Rotor Airloads Prediction Using Multidisciplinary Coupling," *Users Group Conference, 2005*. IEEE, 2005, pp. 147-152. http://doi.ieeecomputersociety.org/10.1109/DODUGC.2005.60

78. Biedron, R. T., and Lee-Rausch, E. M. "Rotor airloads prediction using unstructured meshes and loose CFD/CSD coupling," *26th AIAA Applied Aerodynamics Conference*. 2008.

79. Biedron, R. T., and Lee-Rausch, E. "Computation of UH-60A airloads using CFD/CSD coupling on unstructured meshes," *Annual Forum Proceedings-American Helicopter Society*. Vol. 67, American Helicopter Society, Inc., Virginia Beach, VA, 2011.

80. Abras, J., Lynch, C. E., and Smith, M. J. "Computational fluid dynamics-computational structural dynamics rotor coupling using an unstructured Reynolds-averaged Navier-Stokes methodology," *Journal of the American Helicopter Society* Vol. 57, 2012, pp. 1-14. doi: 10.4050/JAHS.57.012001

81. Bhagwat, M. J., Ormiston, R. A., Saberi, H. A., and Xin, H. "Application of Computational Fluid Dynamics/Computational Structural Dynamics Coupling for Analysis of Rotorcraft Airloads and Blade Loads in Maneuvering Flight," *Journal of the American Helicopter Society* Vol. 57, No. 3, 2012, pp. 1-21. doi: 10.4050/JAHS.57.032007

82. Silbaugh, B., and Baeder, J. D. "Coupled CFD/CSD Analysis of a Maneuvering Rotor Using Staggered and Time-Accurate Coupling Schemes," *AHS Specialists Conference on Aeromechanics, San Francisco, CA*. 2008.

83. Horn, J. F., Calise, A. J., and Prasad, J. V. R. "Flight Envelope Cueing on a Tilt-Rotor Aircraft Using Neural Network Limit Prediction," *Journal of the American Helicopter Society* Vol. 46, No. 1, 2001, pp. 23-31. doi: 10.4050/JAHS.46.23

84. Bottasso, C. L., Croce, A., Leonello, D., and Riviello, L. "Optimization of critical trajectories for rotorcraft vehicles," *Journal of the American Helicopter Society* Vol. 50, No. 2, 2005, pp. 165-177.

85. Jongki, M., and Prasad, J. V. R. "Aggressive maneuvering for obstacle avoidance with envelope protection for autonomous UAVs," *International Specialists' Meeting on Unmanned Rotorcraft Systems*. American Helicopter Society, Inc., Phoenix, AZ, 2009.

86. Ruffin, S. M., and Lee, J.-D. "Rotorcraft Flowfield Prediction Accuracy and Efficiency using a Cartesian Grid Framework," *Int'J. of Mathematical Models and Methods in Applied Sciences* Vol. 3, No. 3, 2009.

87. Renaud, T., O'Brien, J., D M, Smith, M. J., and Potsdam, M. "Evaluation of isolated fuselage and rotor-fuselage interaction using CFD," *Journal of the American Helicopter Society* Vol. 53, No. 1, 2008, pp. 3-17.

88. Duque, E., Sankar, L., Menon, S., Bauchau, O., Ruffin, S., Smith, M., Ahuja, K., Brentner, K., Long, L., and Morris, P. "Revolutionary Physics-Based Design Tools for Quiet Helicopters," *44th AIAA Aerospace Sciences Meeting and Exhibit, Reno, NV January*. 2006, pp. 2006-1068.

89. Beno, E. A. "Analysis of helicopter maneuver-loads and rotor-loads flight test data." Vol. 2225, National Aeronautics and Space Administration, 1973.

90. Yang, Z. "A hybrid flow analysis for rotors in forward flight," *School of Aerospace Engineering*. PhD Thesis, Georgia Institute of Technology, Atlanta, GA, 2000.

91. Steger, J. L., and Warming, R. F. "Flux vector splitting of the inviscid gasdynamic equations with application to finite-difference methods," *Journal of Computational Physics* Vol. 40, No. 2, 1981, pp. 263-293. http://dx.doi.org/10.1016/0021-9991(81)90210-2

92. Van Leer, B. "Flux-vector splitting for the Euler equations," *Eighth international conference on numerical methods in fluid dynamics*. Springer, 1982, pp. 507-512. doi: 10.1007/3-540-11948-5_66

93. Roe, P. L., and Pike, J. "Efficient construction and utilisation of approximate Riemann solutions," *Computing Methods in Applied Science and Engineering*, 1984.

94. Vinokur, M., and Liu, Y. "Equilibrium gas flow computations. II-An analysis of numerical formulations of conservation laws," *26th AIAA Aerospace Sciences Meeting*. Vol. 1, 1988.

95. Van Leer, B. "Towards the ultimate conservative difference scheme. V. A second-order sequel to Godunov's method," *Journal of computational Physics* Vol. 32, No. 1, 1979, pp. 101-136. http://dx.doi.org/10.1016/0021-9991(79)90145-1

96. Van Leer, B. "Upwind and high-resolution methods for compressible flow: From donor cell to residual-distribution schemes," *Communications in Computational Physics* Vol. 1, No. 2, 2006, pp. 192-206. doi: 10.2514/6.2003-3559

97. Van Albada, G., Van Leer, B., and Roberts Jr, W. "A comparative study of computational methods in cosmic gas dynamics," *Astronomy and Astrophysics* Vol. 108, 1982, pp. 76-84. http://hdl.handle.net/1887/6764

98. Pulliam, T. H., and Steger, J. L. "Implicit finite-difference simulations of three-dimensional compressible flow," *AIAA Journal* Vol. 18, No. 2, 1980, pp. 159-167. doi: 10.2514/3.50745

99. Yoon, S., and Jameson, A. "Lower-upper Symmetric-Gauss-Seidel method for the Euler and Navier-Stokes equations," *AIAA Journal* Vol. 26, No. 9, 1988, pp. 1025-1026. doi: 10.2514/3.10007

100. Thomas, P. D., and Lombard, C. K. "Geometric Conservation Law and Its Application to Flow Computations on Moving Grids," *AIAA Journal* Vol. 17, No. 10, 1979, pp. 1030-1037. doi: 10.2514/3.61273

101. Spalart, P. R., and Allmaras, S. R. "A one-equation turbulence model for aerodynamic flows," *AIAA Paper 92-0439*. 1992. doi: 10.2514/6.1992-439

102. Spalart, P. R. "Detached-eddy simulation," *Annual review of fluid mechanics* Vol. 41, 2009, pp. 181-202. doi: 10.1146/annurev.fluid.010908.165130

103. Fang, Y., and Menon, S. "Kinetic-Eddy Simulation of Static and Dynamic Stall," *24 th AIAA Applied Aerodynamics Conference*. 2006. doi: 10.2514/6.2006-3847

104. Zaki, M., Menon, S., and Sankar, L. N. "Hybrid Reynolds-Average Navier-Stokes and Kinetic Eddy Simulation of External and Internal Flows," *Journal of Aircraft* Vol. 47, No. 3, 2010, pp. 805-811. doi: 10.2514/1.43454

105. Johnson, W. *Helicopter Theory*: Dover publications, 1994.

106. Mello, O., Prasad, J., Sankar, L., and Tseng, T. "Analysis of helicopter/ship aerodynamic interactions," *The American Helicopter Society Aeromechanics Specialists Conference, San Francisco, CA*. 1994.

107. Kuethe, A., and Chow, C.-Y. *Foundations of Aerodynamics*: New York: John Wiley and Sons Inc, 1998.

108. Vatistas, G. H., Kozel, V., and Mih, W. "A simpler model for concentrated vortices," *Experiments in Fluids* Vol. 11, No. 1, 1991, pp. 73-76. doi: 10.1007/BF00198434

109. Vatistas, G. H. "New model for intense self-similar vortices," *Journal of Propulsion and Power* Vol. 14, No. 4, 1998, pp. 462-469. doi: 10.2514/2.5323

110. Bhagwat, M. J., and Leishman, J. G. "Generalized viscous vortex model for application to free-vortex wake and aeroacoustic calculations," *Annual Forum Proceedings-American Helicopter Society*. Vol. 58, American Helicopter Society, Inc. , 2002, pp. 2042-2057.

111. Tung, C., Caradonna, F. X., and Johnson, W. R. "The prediction of transonic flows on an advancing rotor," *Journal of the American Helicopter Society* Vol. 31, No. 3, 1986, pp. 4-9. http://dx.doi.org/10.4050/JAHS.31.4

112. Bauchau, O. A., and Liu, H. "On the modeling of hydraulic components in rotorcraft systems," *Journal of the American Helicopter Society* Vol. 51, No. 2, 2006, pp. 175-184. http://dx.doi.org/10.4050/JAHS.51.175

113. Bousman, W. G., and Norman, T. "Assessment of Predictive Capability of Aeromechanics Methods," *Journal of the American Helicopter Society* Vol. 55, No. 1, 2010, pp. 12001-12001. http://dx.doi.org/10.4050/JAHS.55.012001

114. Bousman, W. G. "A qualitative examination of dynamic stall from flight test data," *Journal of the American Helicopter Society* Vol. 43, No. 4, 1998, pp. 279-295. http://dx.doi.org/10.4050/JAHS.43.279

115. Howlett, J. J. "UH-60A Black Hawk engineering simulation program. Volume 1: Mathematical model," 1981.

116. Hilbert, K. B. "A mathematical model of the UH-60 helicopter," *NASA-TM*, 1984.

117. Ormiston, R. A. "An Investigation of the Mechanical Airloads Problem for Evaluating Rotor Blade Structural Dynamics Analysis," *American Helicopter Society 4th Decennial Specialists' Conference on Aeromechanics, San Francisco, CA*. 2004.